UTILIZING POLLEN AS A BIO-ORGANIC TEMPLATE FOR TAILORABLE MULTIMODAL ADHESION

A Thesis
Presented to
The Academic Faculty

by

Ismael J. Gomez

In Partial Fulfillment
of the Requirements for the Degree
Doctor of Philosophy in the
School of Chemical and Biomolecular Engineering

Georgia Institute of Technology
December 2013

UTILIZING POLLEN AS A BIO-ORGANIC TEMPLATE FOR TAILORABLE MULTIMODAL ADHESION

Approved by:

Dr. J. Carson Meredith, Advisor
School of Chemical and Biomolecular Engineering
Georgia Institute of Technology

Dr. Yulin Deng
School of Chemical and Biomolecular Engineering
Georgia Institute of Technology

Dr. Haskell Beckham
School of Materials Science & Engineering
Georgia Institute of Technology

Dr. Yonathan Thio
School of Chemical and Biomolecular Engineering
Georgia Institute of Technology

Dr. Sven Behrens
School of Chemical and Biomolecular Engineering
Georgia Institute of Technology

Date Approved: October 8, 2013

This work is dedicated to my family.

ACKNOWLEDGEMENTS

I would like to thank my family for giving me the strength and support needed to complete my education. To my parents, Ana and Ismael Gomez, the sacrifices you have made to provide me with the opportunity to obtain an education have always motivated me to succeed. Thank you for all your love and inspiration throughout my life. To my siblings, Tiffany, Adrian, and Adam, you've always been my best friends and kept me grounded. Thank you for all the laughs and encouragement you have given me during my time away from home. To my Grandma Violeta, the love and prayers you have given me have helped me succeed in all my endeavors. Finally, to my Great Grandmother, Mama Tere, thank you for always believing in me and watching over me from heaven.

I am especially grateful to my advisor, Dr. Carson Meredith, for being an inspiring mentor during my graduate career. Your support and encouragement have been invaluable to my growth and development. Most importantly, you have helped me become a well-rounded person by teaching me the importance of integrity, a strong work ethic, and attaining a work-life balance. I would like to thank my committee members, Dr. Haskell Beckham, Dr. Sven Behrens, Dr. Yulin Deng, and Dr. Yonathan Thio for providing me with valuable feedback and support throughout my PhD education. Special appreciation is given to my collaborators, Dr. Ken Sandhage and Brandon Goodwin, for their contributions to my work. Additionally, I would like to acknowledge the organizations that provided funding for my research: Dow Chemical and the U.S. Air Force Office for Scientific Research.

I would like to express my gratitude to the professors that have shaped the course of my education. I thank Dr. Ken Smith for providing me with guidance during my time at MIT and encouraging me to pursue a graduate degree. I am grateful to Dr. Paula

Hammond for providing me with the opportunity to perform research as an undergraduate student. The year I spent in your lab provided me with a strong foundation that has enabled me to succeed as a PhD student. I'd like to thank my high school chemistry teacher, Ms. Sharon Veenhoff, for challenging and enlightening me throughout high school. Your guidance has undoubtedly contributed to all my academic success. I am also very thankful to Dr. Sue Ann Bidstrup-Allen for giving me the opportunity to become a mentor and leader through the Exxon-Mobil Success Program. This experience has given me a unique opportunity to grow as a person and become a role-model for other students.

I thank all the current and past members of the Meredith research group, Dr. Keith Reed, Dr. Jung-Hyun Lee, Dr. Reginald Thio, Jie Wu, Dr. Haisheng Lin, Dr. Sangil Han, Timi Fadiran, Natalie Girouard, Dr. Shanhong Xu, Yi Zhang and Donglee Shin, for sharing your knowledge and friendships with me. I appreciate all the discussions, collaborations, and laughs we've shared throughout my time in the group.

Lastly, I'd like to thank my friends, not already mentioned, who have contributed to my quality of life during my time at Georgia Tech. I'd like to give special thanks to Kathleen Vermeersch for sharing many adventures with me and supporting me throughout my PhD education. I'd also like to thank Erin Redmond, Stephanie Didas, Jonathan Rubin, Aubrey Tiernen, Vyran George, Hector Beltran, and Esteban Felix for all their support.

TABLE OF CONTENTS

LIST OF TABLES

LIST OF FIGURES

SUMMARY

The interactions of microparticles, particularly those possessing nano- and microstructured asperities, play a critical role in many industrial applications. As a result, control over particle-particle and particle-surface interactions can be accomplished by designing microparticles with well-defined surface morphologies. Nature provides remarkable examples of evolutionary-optimized microscale biological particles with structures and/or chemistries tailored for effective adhesion to a variety of surfaces under different dynamic and environmental conditions. Prominent among these are pollen, which possess a range of ornamentations consisting of combinations of various morphologies and feature sizes. These surface structures, provided by a highly chemically and mechanically stable outer shell, make pollen a model bioparticle for evaluating geometric effects on adhesion.

This research aims to take advantage of pollen's unique architecture by utilizing it as a biotemplate for designing pollen-derived particles with tailorable microparticle adhesion. In this work, the adhesion behavior of pollen and pollen-derived particles is characterized using atomic force microscopy (AFM). Cleaned natural pollen particles were found to exhibit short-range van der Waals (VDW) adhesion strengths that were independent of surface chemistry and scaled with the tip radius of pollen's ornamentations. Employing pollen as a core material, electrostatic interactions were utilized to controllably coat metal nanoparticles onto pollen's surface. Metal nanoparticle-coated pollen particles displayed enhanced adhesion facilitated by multiple nanoparticle contacts with probe surfaces, while also showing potential for use as surface enhanced Raman scattering (SERS) substrates. Using pollen as a template, a layer-by-layer (LbL) surface sol-gel (SSG) technique allowed for the preparation of high-fidelity ferro- and ferrimagnetic replicas exhibiting short-range VDW-based adhesion governed by the contact of nanocrystals present, and long-range magnetic attraction governed by

the magnetic properties of ferrimagnetic pollen replicas. The results of this work highlight the feasibility of utilizing pollen as a bio-organic template and the potential for designing pollen-derived particles with tailorable adhesion.

CHAPTER 1

INTRODUCTION AND BACKGROUND

1.1 Designing Microstructured Particles

Interest in microparticles has been driven by advances in photonics, catalysis, electronics, electrorheological fluids, biological imaging, and drug delivery [1-7]. Control over particle-particle and particle-surface interactions of microparticles plays a vital role in many industrial applications, such as the adhesion of paints to substrates, the dispersion of dry powder inhalers for drug delivery, the adhesion of toner particles to paper in xerography, and the self-assembly of hierarchical structures [8-14]. These interactions of microstructured particles, specifically those with nanoscale surface asperities, are controlled by the balance of attractive forces (hydrogen bonding, electrostatic forces, and dipole-dipole interactions) and repulsive forces (steric forces and electrostatic repulsion) [15]. As a result, great effort has been devoted to designing microparticles with well-defined shapes, sizes and structures.

1.1.1 Fabrication of Microstructured Particles

Preparation of structured particles is often accomplished by mimicking existing structures using a number of fabrication processes. Figure 1.1 illustrates a number of techniques used to synthesize particles from core particle templates of varying shapes (spheres, rods, cubes), sizes (microns, nanometers), and materials (synthetic, bacteria, biological) [16-20]. Common fabrication methods for synthesizing such particles include surface sol-gel, chemical vapor deposition, atomic layer deposition, layer-by-layer deposition, Pickering emulsion polymerization, chemical reduction/seeded growth, colloidal heteroaggregation, and a combination of these methods [18, 21-26]. Colloidal heteroaggregation and surface sol-gel techniques are of particular interest for preparing *in-situ* and *ex-situ* coatings on core particle templates.

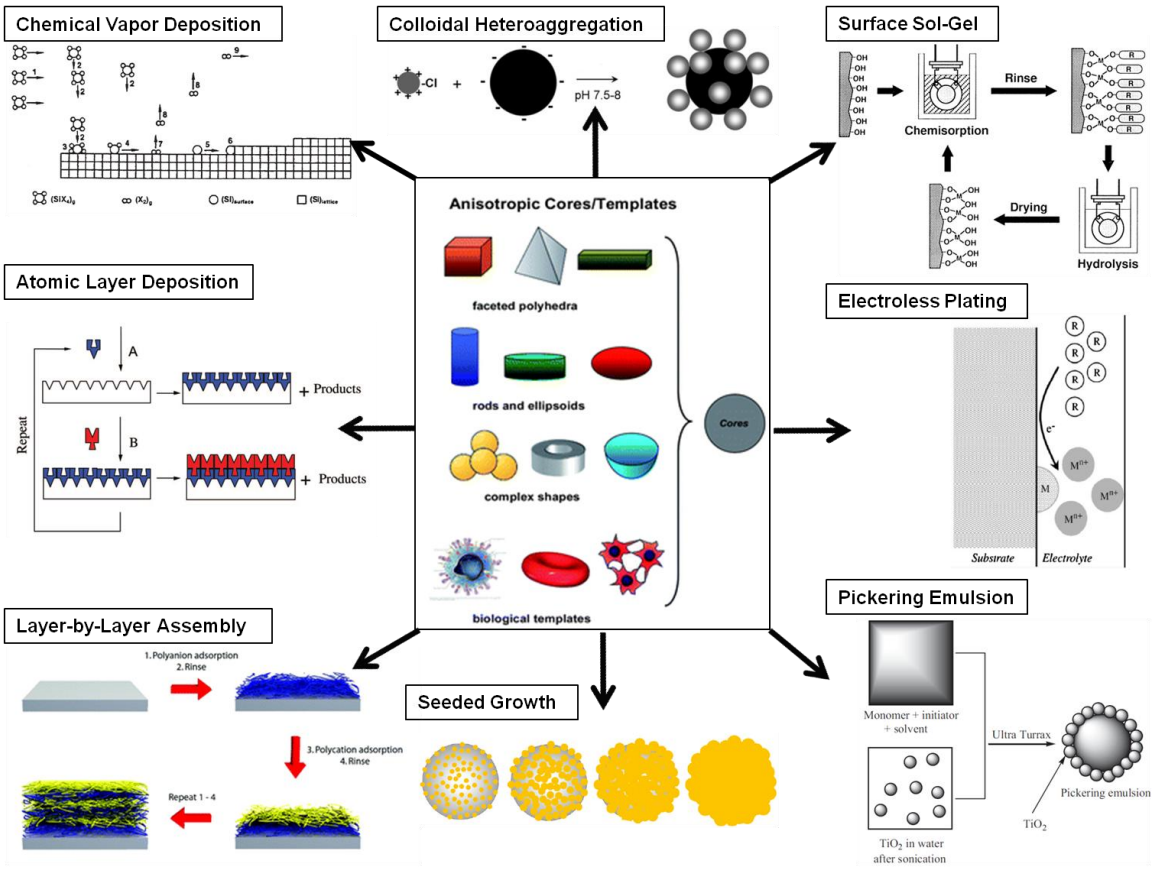

Figure 1.1. Common fabrication methods for preparing hybrid particles from core templates taken from references 11 and 31-38.

1.1.1.1 Sol Gel Process

Sol-gel processes normally require at least one precursor, usually a metal alkoxide, solvents to disperse the precursor, a catalyst, a base, and water. During the sol-gel transformation, the sol (colloid suspension) becomes interconnected to form a gel (a rigid three dimensional network) via hydrolysis of the precursor, alcohol or water condensation of the precursor, or reaction of hydrolysis and condensation products of the precursor [27]. The surface sol-gel process is facilitated by a surface bearing hydroxyl groups and occurs through the chemisorption of the alkoxide, followed by rinsing, hydrolysis of the chemisorbed alkoxide, and drying [28]. The precursor is not necessarily

limited to alkoxides as long as they fulfill the requirements of chemisorption on surface hydroxyl groups and regeneration of the hydroxyl groups after hydrolysis [29].

1.1.1.2 Colloidal Heteroaggregation

Particles suspended in a medium inevitably undergo collisions with one another that can result in an unstable system of aggregates [30]. Heterocoagulation describes permanent, irreversible, contact between particles. Heteroflocculation and heteroassociation define a reversible or temporary association between particles. Heteroaggregation is the general term applies to particle aggregation. Interactions leading to heteroaggregation are often electrostatic in nature, arising from the electric double layer surrounding the particles, and can be induced by mixing oppositely charged particles [31]. Size differences can also promote aggregation of colloids with similar chemistries and charges [32]. Finally, chemistry differences in particles of similar sizes and charges can be used to drive heteroaggregation [33].

1.1.2 Structured Particles Derived from Nature

Nature provides remarkable examples of evolutionary-optimized microscale particles with structures and/or chemistries tailored for effective adhesion to a variety of porous or dense surfaces. Figure 1.2 displays examples of naturally-fabricated diatom, spore, and pollen microparticles. Diatoms, unicellular aquatic algae with siliceous cell walls, possess a high degree of species-specific three-dimensional micro- and nanostructures [34-36]. Spores are unicellular haploid units of asexual reproduction of nonvascular plants (e.g., algae, fungi, and mosses) with roughened surfaces. Pollen is the male gametophyte of angiosperms (i.e. flowering plants) with a high degree of species-specific morphological complexity [37]. Pollen's sustainability, chemical and mechanical stability, and unique architecture make it an appealing candidate for use as a model biotemplate.

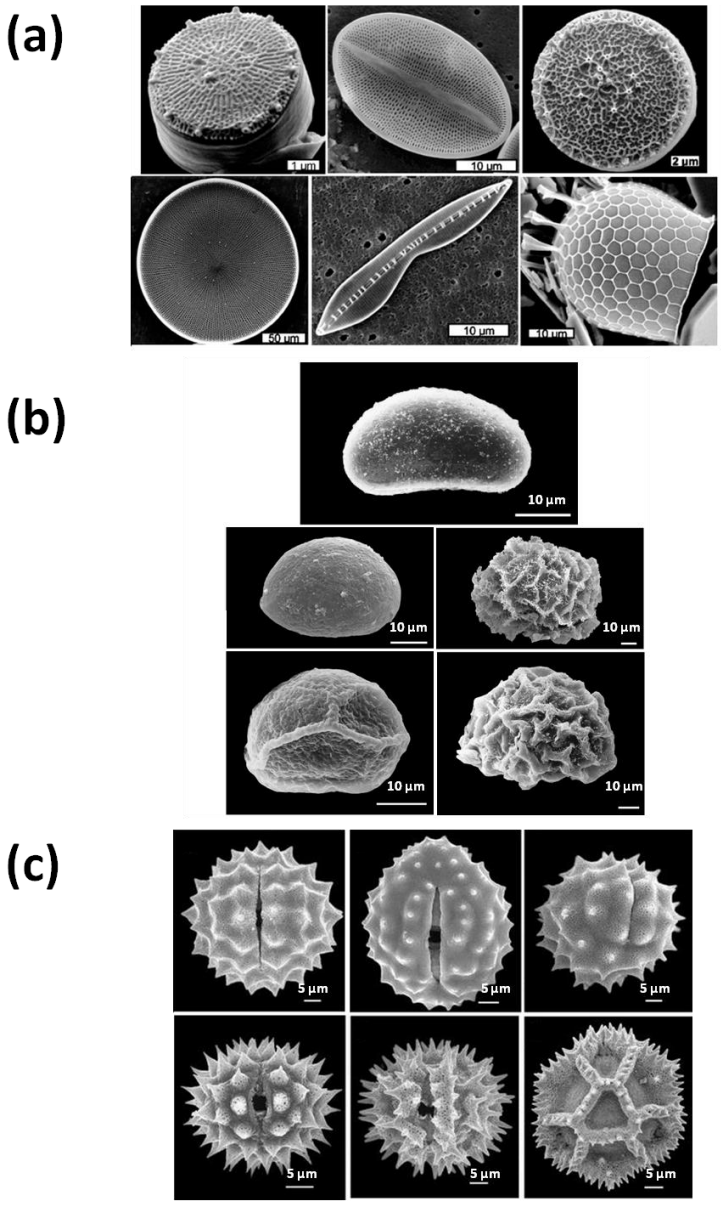

Figure 1.2. Representative scanning electron micrographs of the structural diversity of (a) diatom, (b) spore, and (c) pollen microparticles. Images were taken from references 42-44.

1.2 Pollen as a Biotemplate

1.2.1 Pollen sustainability

Pollen is an ubiquitous material produced by plants in large numbers. A single ragweed (*Ambrosia artemisiifolia*) plant can produce 8 billion ragweed pollen grains in 5 h [38]. It is estimated that more than a million tons of ragweed pollen is produced in a

single season in the U.S. alone [39]. The total yearly pollen production in the world may be several orders of magnitude greater taking into consideration an estimated 352,000 species of flowering, pollen-bearing, plants [40]. Additionally, pollen production is expected to significantly increase based on predicted future climate conditions. Five CO_2 emission scenarios for the period 1850-2100 project a minimum atmospheric CO_2 level of ~440 ppm, with less conservative estimates approaching ~600 ppm, to be achieved by the year 2100 [41]. Subjecting plants to future CO_2 conditions, a 62% increase from year 2000 to future CO_2 levels results in a 90% increase in pollen production [42].

Currently a number of companies (e.g. Greer Laboratories, Inc., Polysciences, Inc., etc.) offer a wide range of pollen species in lab-scale quantities. Commercial harvesting on this scale is supplied by certified farmers in the U.S. and Europe [43]. One such 400-acre farm collects roughly 30 species of pollen and during ragweed season, which runs from mid-August to October, harvests an average of more than four pounds of ragweed pollen per day [44]. Collected pollen is sold to companies at an average cost of 50 cents per gram of pollen and as low as five cents per gram for common pollen such as ragweed. Although it is unclear how pollen collection on a larger scale may impact the environment, the fact that these pollen farms currently exist demonstrate the potential to sustainably harvest pollen to meet consumer demands.

1.2.2 Pollen chemistry

Mature pollen grains are characterized by a number of extracellular and intracellular features as seen in Figure 1.3. The outer pollen wall, known as the exine, possesses a very high mechanical strength [45]. The exine consists of sporopollenin, a biopolymer network essentially insoluble to known solvents and extremely resistant to non-oxidative physical, biological, and chemical degradation [46]. The fact that sporopollenin is insoluble in common acids and solvents limits many of the chemical analyses to solid state techniques. A number of pollen treated with a nonoxidative,

extraction-hydrolyis method were used to isolate the exines of different plant classes. Distinct ^{13}C NMR spectra obtained from these exines indicate that the sporopollenin from different pollen species are all distinct substances [47]. Sporopollenin can therefore be categorized as a class of biopolymers rather than a single, homogeneous macromolecule. FTIR spectra of acetolyzed sporopollenin of *Magnolia grandiflora* Linn. and *Hibiscus syracus* Linn. suggest that the main structure of sporopollenin is a simple aliphatic polymer with aromatic and conjugated groups in the side chains [48]. Specifically, phenols are revealed to be integral compounds of the sporopollenin skeleton through the identification of 4-hydroxy-cinnamic acid from ^{1}H-^{1}H-COSY NMR spectra of silyl and acetyl derivatives of *Typha angustifolia* L. pollen [49-51]. Exposing sporopollenin from *Typha angustifolia* L. to a series of 36 subsequent acidic methanolysis procedures indicate that the sporopollenin polymers possess alkyl chains containing at least ten CH_2 groups and the polymers are linked via ether bridges [52]. Acetolysis-resistant sporopollenin of *Betula pendula* and *Pinus sylvestris* subjected to pyrolysis GC-MS revealed the presence of both p-coumaric acid and ferulic acid [53]. Solid state ^{13}C NMR and RuO_4 chemical degradation, in combination with pyrolysis results, have led to a tentative structure for sporopollenin, shown in Figure 1.4, in which long-chain (C_{24}-C_{28}) highly aliphatic units form the backbone of sporopollenin with cinnamic acids as cross-linking units [54].

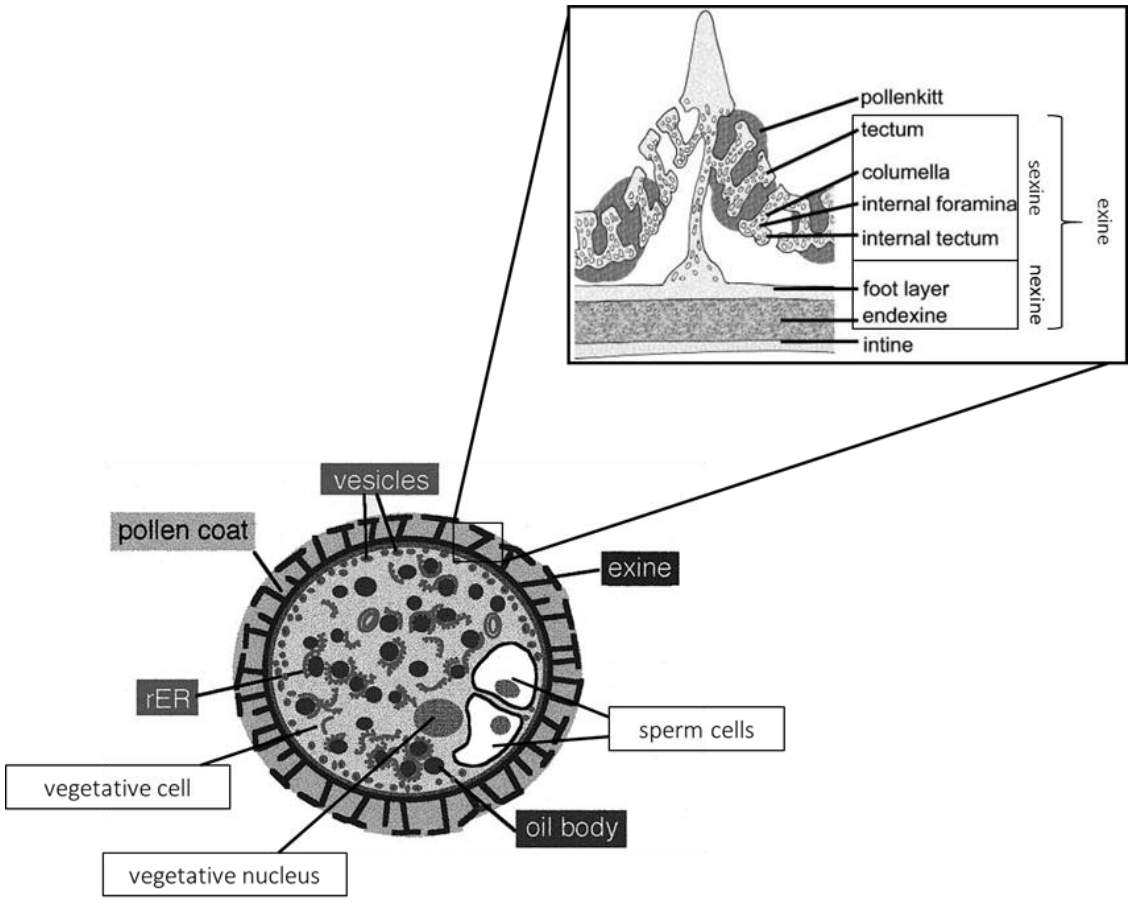

Figure 1.3. Ultrastructure of a typical mature pollen grain. Extracellular features include the inner intine, outer exine, and pollen coat (pollenkitt) filling the cavities of the exine sculpture. The exine is further divided into the sexine (tectum, columella, formina) and nexine (foot layer and endexine). Intracellular features include oil bodies, rough endoplasmic reticulum (rER), numerous vesicles, a vegetative nucleus, a vegetative cell, and sperm cells. Representations were taken from references 59-61.

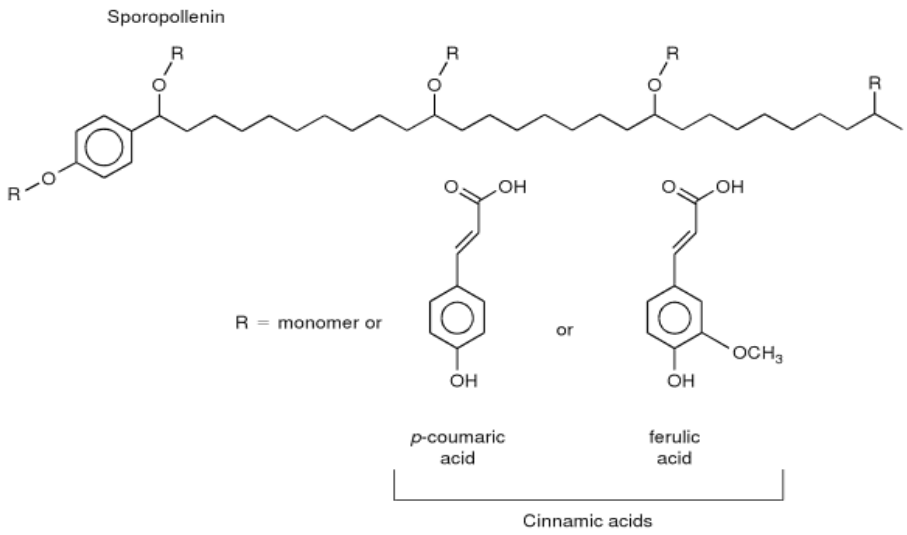

Figure 1.4. Proposed structure of sporopollenin monomeric building blocks taken from reference 58.

A pollen coat, a viscous adhesive material known as pollenkitt, is primarily located in the cavities of the exine as well as the surface of the exine. Pollenkitt offers protection against water loss, fungi or bacteria, and UV radiation. Despite its importance for pollen dispersal and subsequent germination, relatively little is known about the chemical composition of the pollen coat [55]. Analysis of the volatiles from the pollenkitt of *Rosa rugosa* revealed that the coating extract shared half of the volatiles found in pollen (aromatics, C_{11}-C_{16} aliphatics, and terpenoids) and proportionately more C_{16} acetate; comparing to *Rosa canina*, pollenkitt volatiles are distinct even between pollen of different species [56]. From a collection of pollen from 69 angiosperms, the pollenkitt were found to contain non-glyceride neutral lipids (hydrocarbons, fatty acid methyl esters, sterol esters, aldehydes, and ketones), very few polar lipids, and pigments (yellow carotenoids and flavenoids) [57]. Beneath the outer pollen wall lays a cellulose-rich layer called the intine [58]. Filling most of the interior of the pollen grain is a large vegetative cell consisting of a nucleus that lies within the cytoplasm which is densely packed with storage oil bodies, endoplasmic reticulum, vesicles around the periphery of the

cytoplasm, and two sperm cells [55, 59]. These intracellular pollen lipids and membranes are composed of triacylglycerols and membrane-associated phospholipids [55].

1.2.3 Pollen Transport Properties

1.2.3.1 Structural Factors

In nature, pollen structure plays a vital role to its successful dispersal and transport. Wind pollen dispersal is made possible through the evolution of flowering plants to disperse pollen through mechanisms aided by air currents, termed anemophilous. The exine wall in anemophilous pollen species is often modified to enhance buoyancy. Pollinator pollen dispersal is facilitated by pollen adhering to the body of insects (entomophilous) and vertebrates (zoophilous) that consume nectar of flowering plants. The exine wall in entomophilous and zoophilous pollen species often possesses surface rods, spines, and other sculptural features to enhance dissemination [37, 59, 60]. As a result, the structure and sculpture of the exine is what gives pollen their distinct microscopic and submicroscopic morphology [37]. Figure 1.5 identifies the basic architectures of the outer sculptured layer of the exine, the sexine, which are defined by size, shape, and arrangement in Table 1.1 [61]. Additionally, the size of pollen grains typically ranges from 5 microns to greater than 200 microns [37].

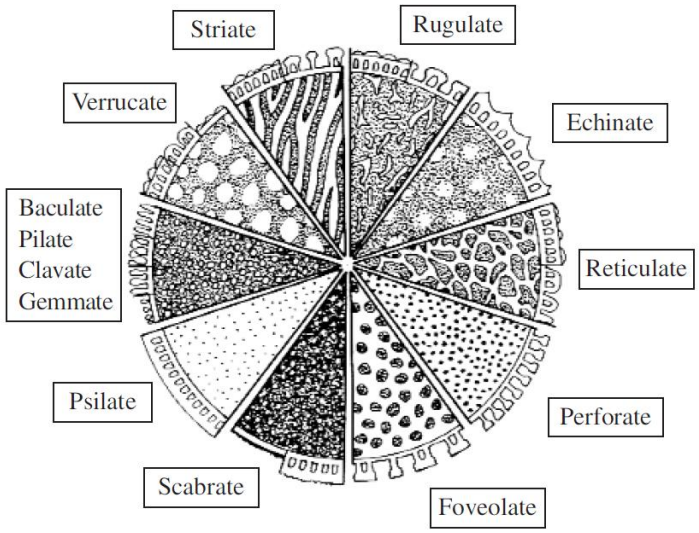

Figure 1.5. Surface sculpturing elements of pollen taken from references 65 and 66. Raised areas are shown light and lower areas are shown dark. Cross-sections of the exine are located around the perimeter.

Table 1.1. Characteristic surface structures of pollen grains [37].

Architecture	Characteristic
Psilate	Smooth surface
Foveolate	Pitted surface
Fossulate	Grooved surface
Perforate	Numerous openings in the tectum
Scabrate	Sculptured elements < 1 μm in any dimension
Verrucate	Sculptured elements > 1 μm with near equal height and width
Gemmate	Sculptured elements with diameters equal to, or greater than, the height with a constricted base of > 1 μm
Baculate	Rod-like elements > 1 μm of greater height than width
Clavate	Elements > 1 μm long of greater height than width with a constricted base or club-shaped tip
Echinate	Pointed spines 1-3 μm long
Rugulate	Horizontally elongated elements in an irregular pattern
Striate	Horizontally elongated elements in an irregular pattern
Reticulate	Horizontally elongated elements forming a net-like pattern

1.2.3.2 Chemical Factors

Pollenkitt is absent from the pollen of strictly and primarily anemophilous taxa, characteristic of entomophilous taxa, present in secondary anemophilous members of otherwise entomophilous families, and present in variable quantities in zoophilous plants [62, 63]. In species possessing pollenkitt, it plays an important role in the survival of pollen grains and eventual fertilization of the ovum. Pollen dispersal is facilitated by pollenkitt's ability to keep pollen grains together during transport and adhere to insects or vertebrates. Pollinators are attracted to the odor, color, and digestible reward of the pollenkitt. Pollen germination and the ovum fertilization is possible because the pollenkitt allows for pollen to adhere to the stigma and rehydrate [62, 64].

1.2.4 Pollen-based Hybrid Materials

Recently pollen grains have attracted much attention as a component for organic-inorganic hybrid materials. For example, pollen composites of ZrO_2/sunflower (*Helianthus annuus*) pollen, Fe_3O_4/ragweed (*Ambrosia artemisiifolia*) pollen, and NiO/carbonized lotus (*Nelumbo nucifera*) pollen have been fabricated *in-situ* for use in hydrogen storage, waste water separation, and anodes in Li-ion batteries, respectively [65-67]. Additionally, the *in-situ* preparation of silver nanoparticle (AgNP)/ragweed, AgNP/rye (*Secale cereale*) pollen, and AgNP/carbonized brassica (*Brassica oleracea*) pollen have been successfully demonstrated [68, 69]. Furthermore, hybrids of $CaHPO_4$/brassica pollen, $CaCO_3$/brassica pollen, SiO_2/brassica pollen, and SiO_2/rape (*Brassica napus*) pollen have been transformed into hollow inorganic pollen replicas by removing the organic pollen template through a calcination step [70, 71]. Little consideration, however, has been given to the adhesive properties of these hybrid pollen particles. Pollen's well-defined surface structures allow for controlled adhesion to surfaces and the deposition of inorganic material could potentially provide a means for tuning the adhesion of pollen-derived particles to surfaces.

1.3 Characterizing the Adhesion of Pollen-Derived Particles

The primary tool used to investigate potential interactions between pollen-derived particles and select surfaces is Atomic Force Microscopy (AFM). AFM not only has the capability to characterize nanoscale surface topographies and morphologies, but can be used to investigate the interactions between a cantilever tip and sample [72-75]. Functionalizing commercially available silicon AFM tips, possessing nano-sized radii, provides a means for understanding specific chemical interactions with select surfaces [76, 77]. Alternatively, colloidal probes can be fabricated by attaching a large particle to the end of a cantilever, typically greater than a few microns in diameter, to measure the interactions between macroscopic particles and a surface of interest [78-81]. The advantage of using a colloidal probe to measure adhesion forces is that interactions are generally enhanced with a colloidal particle and surface as compared to a tip and a surface, i.e., colloidal probe adhesion resulting from van der Waals forces have been measured to be 10^{-8}-10^{-9} N as compared to atom-atom van der Waals forces of 10^{-11} N [75]. A representation of a typical colloidal probe and its accompanying force-distance curve is shown in Figure 1.6.

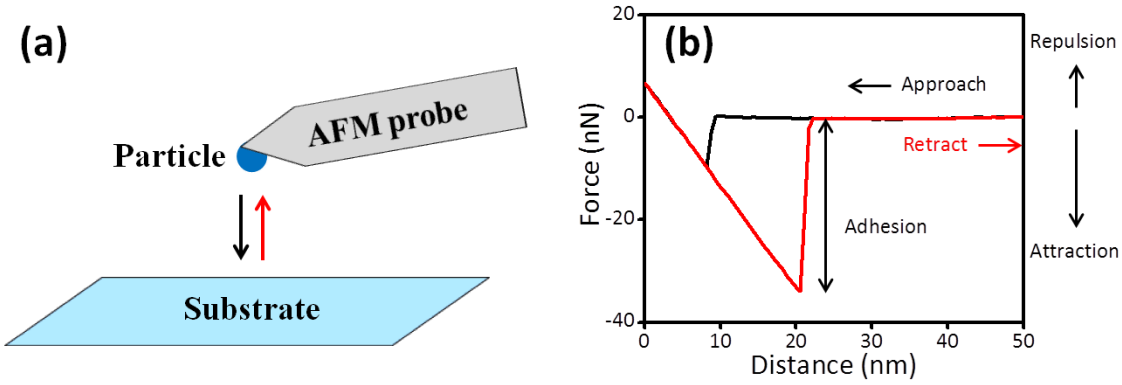

Figure 1.6. Representation of (a) an AFM colloidal probe and (b) a typical force distance curve.

Repulsive and attractive forces are measured from approach force curve in Figure 1.6b, while adhesive forces are determined from the force well in the accompanying

retraction force curve. At large separation distances, the colloidal probe does not experience any attractive or repulsive forces. As the probe approaches the substrate, the particle experiences an initial attraction and jumps to contact with the substrate. This is immediately followed by repulsion defined by a loading force. The probe is then retracted and adheres to the surface based on interactions between the two. This attractive force is overcome by further retraction of the probe until it returns to its initial state. The adhesion force is determined by the depth of the force well at maximum attraction relative to the baseline force at large separations. Common forces detected by colloidal AFM include, but are not limited to, van der Waals, electrostatic, magnetic, capillary, hydrogen bonding, and solvation. Adjustment of probe type, substrate, and medium can aid in elucidating specific interactions present in any given system.

Native pollen, pollen composite, and pollen replica particles present an intriguing system for understanding the mechanisms of particle adhesion. Pollen's unique structure will play an important role in the adhesion of pollen-derived particles. Consequently, colloidal AFM will be a critical tool for investigating pollen interactions. The major objectives of this thesis include:

1) Quantify the dependence of pollen adhesion on exine size and shape using colloidal AFM.
2) Control the deposition of nanoparticles onto pollen using electrostatic interactions to modify pollen's adhesive properties and impart optical functionality.
3) Utilize pollen as a template in the surface sol-gel fabrication of replicas possessing magnetic behavior.
4) Tune the magnetic attraction of the pollen replicas and model the long-range magnetic interactions of the replicas using a permanent magnet as a probe.

1.4 Thesis Overview

This research aims to utilize unique pollen grain morphologies as templates to create pollen-derived particles with controlled adhesion to surfaces. These particles will allow us to take advantage of the adhesive nature of pollen grains, while imparting additional functionality, such as surface enhanced Raman scattering (SERS) and magnetic. Colloidal probe AFM is the primary tool used to investigate the role interfacial forces play in governing particle adhesion. Chapter 2 focuses on understanding the structural factors governing the adhesion of natural pollen grains with varying sizes and architectures using colloidal probe AFM. Chapter 3 describes a method for preparing gold and silver nanoparticle-coated pollen grains using an *ex-situ* electrostatic-driven technique. The effect of metal coatings on particle adhesion will be explored using colloidal probe AFM and their potential as surface-enhanced Raman scattering (SERS) agents is evaluated. Chapter 4 details the preparation of magnetic pollen replica particles of hematite and magnetite via an *in-situ* layer-by-layer (LBL) surface sol-gel (SSG) process. The short-range adhesion and long-range magnetic attraction of pollen replicas is investigated using the colloidal AFM technique. Chapter 5 focuses on the tunability of the magnetic attraction of pollen replicas based on LBL coating thickness. Additionally, the magnetic forces are simulated and modeled using a finite difference approximation. Chapter 6 concludes with a summary of the important findings and provides future recommendations based on this work.

1.5 References

1. Cheng, H., et al., *Photonic porous silicon-based hybrid particles by soft-lithography.* physica status solidi (c), 2011. **8**(6): p. 1754-1758.

2. Lewis, C.L., et al., *Microfluidic fabrication of hydrogel microparticles containing functionalized viral nanotemplates.* Langmuir, 2010. **26**(16): p. 13436-13441.

3. Ju, S.A., et al., *Graphene-Wrapped Hybrid Spheres of Electrical Conductivity.* ACS Applied Materials & Interfaces, 2011. **3**(8): p. 2904-2911.

4. Liu, Y.D., F.F. Fang, and H.J. Choi, *Core−Shell Structured Semiconducting PMMA/Polyaniline Snowman-like Anisotropic Microparticles and Their Electrorheology.* Langmuir, 2010. **26**(15): p. 12849-12854.

5. Pai, R.K. and M. Cotlet, *Highly Stable, Water-Soluble, Intrinsic Fluorescent Hybrid Scaffolds for Imaging and Biosensing.* The Journal of Physical Chemistry C, 2011. **115**(5): p. 1674-1681.

6. Du, C., et al., *PUA/PSS multilayer coated CaCO3 microparticles as smart drug delivery vehicles.* Materials Science and Engineering: C, 2013(0).

7. Sanchez, C., et al., *Applications of hybrid organic-inorganic nanocomposites.* Journal of Materials Chemistry, 2005. **15**(35-36): p. 3559-3592.

8. Vesely, D., A. Kalendova, and M.V. Manso, *Properties of calcined kaolins in anticorrosion paints depending on PVC, chemical composition and shape of particles.* Progress in Organic Coatings, 2012. **74**(1): p. 82-91.

9. Kalendová, A., D. Veselý, and P. Kalenda, *Properties of paints with hematite coated muscovite and talc particles.* Applied Clay Science, 2010. **48**(4): p. 581-588.

10. Littringer, E.M., et al., *Spray dried mannitol carrier particles with tailored surface properties–The influence of carrier surface roughness and shape.* European Journal of Pharmaceutics and Biopharmaceutics, 2012. **82**(1): p. 194-204.

11. Raula, J., et al., *Investigations on particle surface characteristics vs. dispersion behaviour of l-leucine coated carrier-free inhalable powders.* International Journal of Pharmaceutics, 2010. **385**(1): p. 79-85.

12. Zhou, H., M. Götzinger, and W. Peukert, *The influence of particle charge and roughness on particle–substrate adhesion.* Powder Technology, 2003. **135–136**(0): p. 82-91.

13. Zhang, H., et al., *Adhesion properties of nanoparticle-coated emulsion aggregation toner.* Powder Technology, 2011. **208**(3): p. 582-589.

14. Sacanna, S. and D.J. Pine, *Shape-anisotropic colloids: Building blocks for complex assemblies.* Current Opinion in Colloid & Interface Science, 2011. **16**(2): p. 96-105.

15. Bishop, K.J., et al., *Nanoscale Forces and Their Uses in Self-Assembly.* small, 2009. **5**(14): p. 1600-1630.

16. Nomura, T., et al., *Synthesis of hollow silica microparticles from bacterial templates.* Advanced Powder Technology, 2010. **21**(2): p. 218-222.

17. Kobayashi, Y., V. Salgueiriño-Maceira, and L.M. Liz-Marzán, *Deposition of silver nanoparticles on silica spheres by pretreatment steps in electroless plating.* Chemistry of Materials, 2001. **13**(5): p. 1630-1633.

18. Raty, J.-Y., F. Gygi, and G. Galli, *Growth of carbon nanotubes on metal nanoparticles: A microscopic mechanism from ab initio molecular dynamics simulations.* Physical review letters, 2005. **95**(9): p. 096103.

19. Moya, S., et al., *Polyelectrolyte multilayer capsules templated on biological cells: core oxidation influences layer chemistry.* Colloids and Surfaces A: Physicochemical and Engineering Aspects, 2001. **183–185**(0): p. 27-40.

20. Lisunova, M., et al., *Template-Assisted Assembly of the Functionalized Cubic and Spherical Microparticles.* Langmuir, 2012. **28**(37): p. 13345-13353.

21. Yuan, J. and T. Zhou, *Efficient synthesis of asymmetric particles by sol-gel process.* Colloid and Polymer Science, 2013. **291**(5): p. 1227-1234.

22. Ferguson, J., A. Weimer, and S. George, *Atomic layer deposition of Al2O3 films on polyethylene particles.* Chemistry of Materials, 2004. **16**(26): p. 5602-5609.

23. Johnston, A.P., et al., *Layer-by-layer engineered capsules and their applications.* Current Opinion in Colloid & Interface Science, 2006. **11**(4): p. 203-209.

24. Liu, Y., et al., *Polymer microspheres stabilized by titania nanoparticles.* Materials Letters, 2006. **60**(29–30): p. 3731-3734.

25. Sanchez-Gaytan, B.L. and S.-J. Park, *Spiky gold nanoshells.* Langmuir, 2010. **26**(24): p. 19170-19174.

26. Xia, L.Y., et al., *A facile heteroaggregate-template route to hollow magnetic mesoporous spheres with tunable shell structures.* Journal of Materials Chemistry, 2011. **21**(25): p. 9020-9026.

27. Kumar, A., et al., *A review on development of solid phase microextraction fibers by sol–gel methods and their applications.* Analytica chimica acta, 2008. **610**(1): p. 1-14.

28. Wang, G., et al., *Layer-By-Layer Dendritic Growth of Hyperbranched Thin Films for Surface Sol–Gel Syntheses of Conformal, Functional, Nanocrystalline Oxide Coatings on Complex 3D (Bio)silica Templates.* Advanced Functional Materials, 2009. **19**(17): p. 2768-2776.

29. Ichinose, I., H. Senzu, and T. Kunitake, *A Surface Sol−Gel Process of TiO2 and Other Metal Oxide Films with Molecular Precision.* Chemistry of Materials, 1997. **9**(6): p. 1296-1298.

30. Islam, A.M., B.Z. Chowdhry, and M.J. Snowden, *Heteroaggregation in colloidal dispersions.* Advances in Colloid and Interface Science, 1995. **62**(2–3): p. 109-136.

31. Lin, W., et al., *Heteroaggregation in Binary Mixtures of Oppositely Charged Colloidal Particles.* Langmuir, 2005. **22**(3): p. 1038-1047.

32. Shenoy, S.S., et al., *Heteroflocculation of binary latex dispersions of similar chemistry but varying size.* Journal of Colloid and Interface Science, 2003. **268**(2): p. 380-393.

33. Maruyama, K., M. Kawaguchi, and T. Kato, *Heterocoagulation behavior of poly(styrene-co-butadiene) and poly(butyl acrylate) at high particle concentrations.* Colloids and Surfaces A: Physicochemical and Engineering Aspects, 2001. **189**(1–3): p. 211-223.

34. Round, F.E., R.M. Crawford, and D.G. Mann, *The Diatoms : biology & morphology of the genera*1990, Cambridge England ; New York: Cambridge University Press. 747 p.

35. Crawford, S.A., et al., *Nanostructure of the diatom frustule as revealed by atomic force and scanning electron microscopy.* Journal of Phycology, 2001. **37**(4): p. 543-554.

36. Kröger, N., *Prescribing diatom morphology: toward genetic engineering of biological nanomaterials.* Current Opinion in Chemical Biology, 2007. **11**(6): p. 662-669.

37. Kapp, R.O., *How to know pollen and spores*. Pictured-key nature series1969, Dubuque, Iowa,: W. C. Brown Co. ix, 249 p.

38. Grater, W.C. and T.R. Stemen, *The plant, the pollen and the patient.* Review of Palaeobotany and Palynology, 1967. **4**(1): p. 187-192.

39. Horn, E., *A summer hay fever plant survey of Manhattan, Kansas.* Transactions of the Kansas Academy of Science (1903-), 1933. **36**: p. 91-97.

40. Paton, A.J., et al., *Towards target 1 of the global strategy for plant conservation: a working list of all known plant speciesprogress and prospects.* Taxon, 2008. **57**(2): p. 602-611.

41. Kharecha, P.A. and J.E. Hansen, *Implications of "peak oil" for atmospheric CO2 and climate.* Global Biogeochemical Cycles, 2008. **22**(3).

42. Ziska, L.H. and F.A. Caulfield, *Rising CO2 and pollen production of common ragweed (Ambrosia artemisiifolia L.), a known allergy-inducing species: implications for public health.* Functional Plant Biology, 2000. **27**(10): p. 893-898.

43. Codina, R., R.E. Esch, and W.G. Mahoney. *Testing of Raw Materials Used for the Production of Allergenic Extracts*. 2011 [Cited September 5, 2013]; Available from: http://www.greerlabs.com/files/Library/Manufacturing-and-Testing/Testing_Raw_Materials_EAACI_Meeting_2010_Final_Approved_11_2011.pdf.

44. Bavley, A. *Farmers Cultivate Allergy Sufferers' Worst Nightmare*. 2004 [Cited September 5, 2013]; Available from: http://billingsgazette.com/business/farmers-cultivate-allergy-sufferers-worst-nightmare/article_bbc8de4a-67ea-52ef-82e9-f2aaa06b6f5e.html.

45. Liu, T. and Z. Zhang, *Mechanical properties of desiccated ragweed pollen grains determined by micromanipulation and theoretical modelling.* Biotechnology and Bioengineering, 2004. **85**(7): p. 770-775.

46. Domínguez, E., et al., *Pollen sporopollenin: degradation and structural elucidation.* Sexual Plant Reproduction, 1999. **12**(3): p. 171-178.

47. Guilford, W.J., et al., *High Resolution Solid State 13C NMR Spectroscopy of Sporopollenins from Different Plant Taxa.* Plant Physiology, 1988. **86**(1): p. 134-136.

48. Kawase, M. and M. Takahashi, *Chemical composition of sporopollenin in Magnolia grandiflora (Magnoliaceae) and Hibiscus syriacus (Malvaceae).* Grana, 1995. **34**(4): p. 242-245.

49. Niester-Nyveld, C., et al., *Immunocytochemical localization of phenolic compounds in pollen walls using antibodies againstp-coumaric acid coupled to bovine serum albumin.* Protoplasma, 1997. **197**(3-4): p. 148-159.

50. Ahlers, F., et al., *1H NMR analysis of sporopollenin from Typha Angustifolia.* Phytochemistry, 1999. **50**(6): p. 1095-1098.

51. Ahlers, F., J. Lambert, and R. Wiermann, *Acetylation and silylation of piperidine solubilized sporopollenin from pollen of Typha angustifolia L.* ZEITSCHRIFT FUR NATURFORSCHUNG C, 2003. **58**(11/12): p. 807-811.

52. Bubert, H., et al., *Continuous decomposition of sporopollenin from pollen of Typha angustifolia L. by acidic methanolysis.* Zeitschrift fur Naturforschung C-Journal of Biosciences, 2002. **57**(11-12): p. 1035-1041.

53. Rozema, J., et al., *UV-B absorbance and UV-B absorbing compounds (para-coumaric acid) in pollen and sporopollenin: the perspective to track historic UV-B levels.* Journal of Photochemistry and Photobiology B: Biology, 2001. **62**(1–2): p. 108-117.

54. van Bergen, P.F., et al., 2004: p. Structural biomacromoleules in plants: what can be learnt from the fossil record?. In: Hemsley, A.R. and Poole I. (eds.), Linnean

Society Symposium Series, 21, Evolution of Plant Physiology, Elsevier, Amsterdam, p. 134-154.

55. Piffanelli, P., J.H.E. Ross, and D.J. Murphy, *Biogenesis and function of the lipidic structures of pollen grains.* Sexual Plant Reproduction, 1998. **11**(2): p. 65-80.

56. EM Dobson, H., et al., *Pollen and flower volatiles in two Rosa species.* Phytochemistry, 1987. **26**(12): p. 3171-3173.

57. Dobson, H.E.M., *Survey of Pollen and Pollenkitt Lipids - Chemical Cues to Flower Visitors?* American Journal of Botany, 1988. **75**(2): p. 170-182.

58. Schulte, F., et al., *Chemical Characterization and Classification of Pollen.* Analytical Chemistry, 2008. **80**(24): p. 9551-9556.

59. Knox, R.B., *Pollen and allergy*. The Institute of Biology's studies in biology1979, Baltimore: University Park Press. 59 p.

60. Stanley, R.G. and H.F. Linskens, *Pollen: biology, biochemistry, management*1974, Berlin, New York,: Springer-Verlag. ix, 307 p.

61. Frenguelli, G., et al., *Pollini allergenici: morfologia e aspetti microscopici.* Giorn It Allergol Immunol Clin, 1991. **1**: p. 389-401.

62. Pacini, E. and M. Hesse, *Pollenkitt - its composition, forms and functions.* Flora - Morphology, Distribution, Functional Ecology of Plants, 2005. **200**(5): p. 399-415.

63. Hemsley, A. and I. Ferguson, *Pollen morphology of the genus Erythrina (Leguminosae: Papilionoideae) in relation to floral structure and pollinators.* Annals of the Missouri Botanical Garden, 1985: p. 570-590.

64. Pacini, E., *Tapetum character states: analytical keys for tapetum types and activities.* Canadian Journal of Botany, 1997. **75**(9): p. 1448-1459.

65. Yang, X., et al., *Synthesis of spinous ZrO2 core–shell microspheres with good hydrogen storage properties by the pollen bio-template route.* Scripta Materialia, 2011. **64**(12): p. 1075-1078.

66. Thio, B.J.R., K.K. Clark, and A.A. Keller, *Magnetic pollen grains as sorbents for facile removal of organic pollutants in aqueous media.* Journal of hazardous materials, 2011. **194**: p. 53-61.

67. Xia, Y., et al., *Biotemplated fabrication of hierarchically porous NiO/C composite from lotus pollen grains for lithium-ion batteries.* Journal of Materials Chemistry, 2012. **22**(18): p. 9209-9215.

68. Joseph, V., et al., *Surface-enhanced Raman scattering with silver nanostructures generated in situ in a sporopollenin biopolymer matrix.* Chem. Commun., 2011. **47**(11): p. 3236-3238.

69. Wang, Y., et al., *Carbon microspheres with supported silver nanoparticles prepared from pollen grains.* Langmuir, 2005. **21**(23): p. 10846-10849.

70. Hall, S.R., H. Bolger, and S. Mann, *Morphosynthesis of complex inorganic forms using pollen grain templates.* Chem. Commun., 2003(22): p. 2784-2785.

71. Cao, F. and D.-X. Li, *Morphology-controlled synthesis of SiO2 hollow microspheres using pollen grain as a biotemplate.* Biomedical Materials, 2009. **4**(2): p. 025009.

72. Wang, D., et al., *True Surface Topography and Nanomechanical Mapping Measurements on Block Copolymers with Atomic Force Microscopy.* Macromolecules, 2010. **43**(7): p. 3169-3172.

73. Tian, B., et al., *Doxorubicin-loaded lipid-quantum dot hybrids: Surface topography and release properties.* International Journal of Pharmaceutics, 2011. **416**(2): p. 443-447.

74. Weisenhorn, A.L., et al., *Forces in atomic force microscopy in air and water.* Applied Physics Letters, 1989. **54**(26): p. 2651-2653.

75. Binnig, G., C.F. Quate, and C. Gerber, *Atomic force microscope.* Physical review letters, 1986. **56**(9): p. 930.

76. Chirasatitsin, S. and A.J. Engler, *Detecting cell-adhesive sites in extracellular matrix using force spectroscopy mapping.* Journal of Physics: Condensed Matter, 2010. **22**(19): p. 194102.

77. Wong, S.S., et al., *Covalently functionalized nanotubes as nanometre-sized probes in chemistry and biology.* Nature, 1998. **394**(6688): p. 52-55.

78. Lee, J.-H., I. Gomez, and J.C. Meredith, *Non-DLVO Silica Interaction Forces in NMP–Water Mixtures. I. A Symmetric System.* Langmuir, 2011. **27**(11): p. 6897-6904.

79. Lee, J.-H., et al., *Role of Lewis Basicity and van der Waals Forces in Adhesion of Silica MFI Zeolites (010) with Polyimides.* Langmuir, 2009. **25**(16): p. 9101-9107.

80. Benli, B., et al., *Evaluation of Adhesion Forces in Alginate–Filler System Using an AFM Colloidal Probe Technique.* Journal of Adhesion Science and Technology, 2011. **25**(11): p. 1159-1173.

81. Zhang, X., et al., *Adhesion and friction studies of microsphere-patterned surfaces in contact with atomic force microscopy colloidal probe.* Colloids and Surfaces A: Physicochemical and Engineering Aspects, 2012. **401**(0): p. 90-96.

CHAPTER 2

QUANTIFYING THE STRUCTURAL FACTORS CONTRIBUTING TO POLLEN GRAIN ADHESION

This chapter was published in part in *Langmuir*, *29*, 3012, (2013) and is reproduced here with permission.

2.1 Overview

Plant pollens are microscopic particles exhibiting a remarkable breadth of complex solid surface features. In this chapter, we report AFM adhesion measurements of five pollen species, each with a unique surface morphology, with a series of test surfaces. Atomic force microscopy (AFM) was used to measure adhesion forces between echinate (ragweed, sunflower, and dandelion) and reticulate (poplar and olive) pollen grains and surfaces of varying wettability (polyvinyl alcohol (PVA), polyvinyl acetate (PVAc), polystyrene (PS), silicon (Si), and gold-coated silicon (Au-Si)) in air. The results indicate that pollen grains have adhesion strengths that are independent of surface chemistry and scalable with the tip radius of the pollen's ornamentation features according to the Hamaker model. To our knowledge, there exist no quantitative studies of the effects of the exine solid surface features on the adhesion of pollen grains.

2.2 Introduction

The adhesion of particles to surfaces has been of long-standing interest to scientific investigation of many natural and environmental phenomena, including pollination, bacterial, mold and fungal growth, and distribution of airborne pollutants. In addition, particle-surface adhesion is important in engineering applications including filtration, paints and pigments, coatings, sensors, drug delivery, xerography, and semiconductor processing [1]. It is well-recognized that adhesion is influenced by the shape, size, and surface morphology of the particles [1-5]. Increasingly there is interest in

the utilization of particles with complex surface morphologies, such as spiky shapes, in advanced materials. These applications include directed assembly of cells, conductive metal-polymer composites, Pickering emulsions, zeolite-polymer composite membranes for separations, and xerography [6-10]. In fact, the fabrication of such complex particles is beginning to become an experimental reality, including techniques such as flow lithography, templated hydrothermal synthesis, and coating processes [11-14]. However, most of our knowledge of particle adhesion is based upon experiments and models of simple geometries (sphere, cylinder) without organized fine-scale surface physical features.

In contrast, nature provides remarkable examples of evolutionary-optimized microscale biological particles with structures and/or chemistries tailored for effective adhesion to a variety of surfaces under different dynamic and environmental conditions. Prominent among these are pollens, which possess a range of ornamentations consisting of combinations of various morphologies and feature sizes making them model bioparticles for evaluating geometry effects on adhesion. For example, pollen microstructures range from smooth, to reticulate (grooves), to extremely spiny echinate varieties, structures that appear qualitatively to be related to dispersal mechanism and to allergenicity [15]. These structures are provided by a unique chemically and mechanically stable outer exine shell, composed predominantly of sporopollenin, a cross-linked complex polymer consisting of long-chain fatty acids and modest levels of oxygenated aromatic and phenylpropanoid residues [16-19]. Sporopollenin is one of the most chemically resistant naturally occurring materials and has been found intact in fossils that are ca. 500 million years old [20, 21]. This stability suggests that pollen could be used directly or as biotemplates to produce microparticles for encapsulation and dispersal (sensors, drug delivery, and agrochemical delivery), promoting stability and delivery of contents over long time and distance spans. However, the exact mechanisms of pollen adhesion to natural and manmade surfaces have remained elusive. A

quantitative description of the dependence of adhesion on microstructure is important to our understanding of plant biology, epidemiology of asthma and allergies, and biomimetic materials design, e.g., by mimicking pollen adhesive mechanisms to enable the design of microscale particles with specific tailored adherence.

Pollen grains are additionally coated with an oily liquid that resides on or within cavities in the exine wall [22]. This coating material (named pollenkitt by Knoll) is especially prevalent in entomophilous plants, is a mixture composed of saturated and unsaturated lipids and lesser amounts of carotenoids, flavonoids, proteins, and carbohydrates, and is of great importance in pollination ecology [16, 23, 24]. Pollen from land-based plants are largely dispersed by wind or animals (insects, bats, birds). Pollen dispersal is thought to be facilitated by pollenkitt's ability to keep pollen grains together during transport and promoting adhesion to animals. Pollen germination and fertilization of the ovum are possible because the pollenkitt supports pollen adhesion to the stigma and rehydration [25, 26].

To date, the quantitative dependence of pollen adhesion on solid exine feature size and shape has not been reported. In the present work, five distinct species of pollen were chosen as models, each with a unique surface morphology, and their adhesion with various substrates was determined using AFM. Naturally occurring pollenkitt was removed to isolate the effects of pollen morphology on adhesion. We demonstrate that the structural contribution to pollen adhesion is mediated by the geometry of the solid exine and is independent of the chemistry of the counter surface.

2.3 Experimental

2.3.1 Materials and Procedure

2.3.1.1 Materials

All the native non-defatted pollen grains were purchased from Greer Laboratories (Lenoir, NC) and stored at 0 °C. Polystyrene (PS, Mw = 230,000, Sigma-Aldrich, Co., St.

Louis, MO USA), poly(vinyl acetate) (PVAc, Mw = 50,000, Alfa Aesar, Ward Hill, MA USA), and poly(vinyl alcohol) (PVA, Mw = 89,000-98,000, Sigma-Aldrich, Co., St. Louis, MO USA) were used as received without further purification.

2.3.1.2 Sample Preparation

The PS solution was prepared by dissolving 10% by mass in toluene while 5% by mass PVAc and PVA solutions were prepared in hexafluoroisopropanol (HFIP, TCI America). Polymeric test surfaces were prepared as thin polymer films on piranha-etched (30/70 vol.% H_2O_2/concentrated H_2SO_4 at 80 °C for 2 h) silicon substrates by using a knife-edge coating technique described in detail elsewhere [27]. Films were dried at room temperature for 24 h after coating and then annealed at 80 °C under vacuum for 2 h. Film thickness, measured with interferometry, was approximately 1-2 μm, which far exceeds the range of van der Waals interactions (VDW) (~20 nm) and negates energetic effects of the underlying silicon substrate on the polymer-pollen interactions. The mean (Ra) and root-mean-square (rms) surface roughness of each surface coating were obtained from topography scans of three random 10 μm x 10 μm areas on each substrate surface using atomic force microscopy (AFM, Veeco Dimension 3100).

Pollen grains from five different species, each with unique ornamentation (as shown in Figure 2.1), were studied in this work, including olive (*Olea europaea*), poplar (*Populus nigra*), ragweed (*Ambrosia artemisiifolia*), dandelion (*Taraxacum officinale*), and sunflower (*Helianthus annuus*) pollen. For comparison of the effects of variations in particle surface topography, pollens representing two morphologies were explored: (1) a nanoscale reticulate (grooved) structure (olive and poplar pollen) and (2) an echinate (spiked) microstructure (ragweed, dandelion, and sunflower pollen). Olive, poplar, and ragweed are widespread anemophilous plants, in which pollen grains are spread primarily by wind and are coated by a thin layer of pollenkitt. In contrast, the pollen grains of dandelion and sunflower (entomophilious plants) are primarily spread by insects and are

covered by a relatively thick layer of pollenkitt [25, 26]. In order to isolate the effects of structural adhesion, we obtained non-defatted pollen grains and applied a solvent washing procedure to remove the pollenkitt. Non-defatted pollen samples were washed in a mixture of chloroform and methanol (3:1), a solvent for external pollenkitt, but a nonsolvent for the sporopollenin exine for 24 h before being deposited on filter paper (P5, Fisher Scientific, Pittsburgh, PA) supported on a stainless steel 47 mm screen (Kontes Glass, Vineland, NJ) [28]. Pollens subjected to this solvent washing procedure are referred to as “cleaned pollen”.

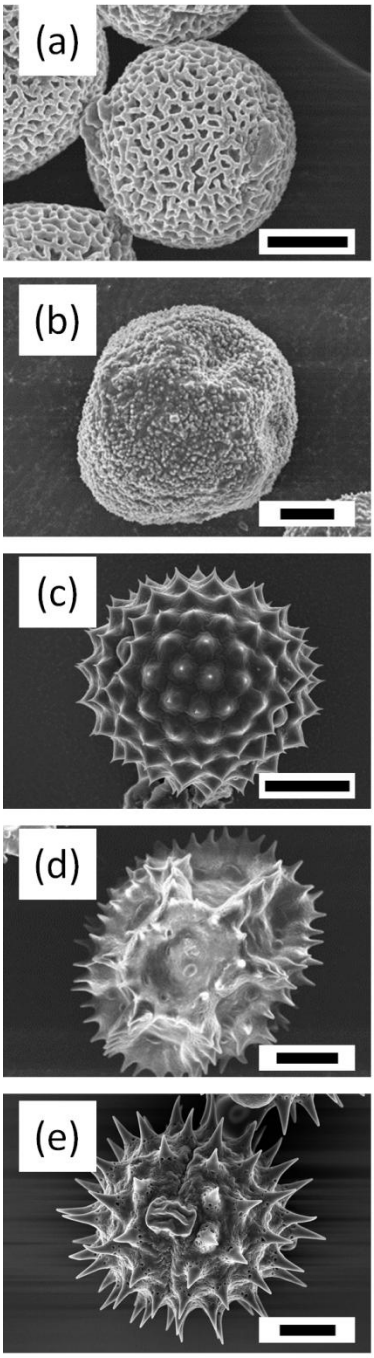

Figure 2.1. Scanning electron micrographs of a) poplar, b) olive, c) ragweed, d) dandelion, and e) sunflower pollen. Scale bars represent 6 µm.

2.3.2 Experimental Methods

2.3.2.1 Force Measurements

Adhesion forces were measured using atomic force microscopy (AFM, Veeco Dimension 3100). Tipless rectangular cantilevers with nominal spring constants of 0.1-0.6 N/m for cleaned pollen (AppliedNanoStructures, Inc., Santa Clara, CA) were used. Single pollen grains were glued to the tipless cantilevers with a small amount of epoxy resin, as seen in Figure 2.2, using a procedure described in detail elsewhere [29]. The actual spring constants for the cantilevers with the attached pollen grains were determined directly by the methods of Burnham and Hutter et al.[30, 31]. A series of 20 force-distance curves were measured for each combination of pollen tip-polymer surface, taken on three separate substrate surfaces within three randomly chosen 10 μm x 10 μm areas on each substrate under normal air condition (20 °C, 30% humidity). Three separate pollen AFM tips were used for each species. The applied load during force measurements was 2.5 nN.

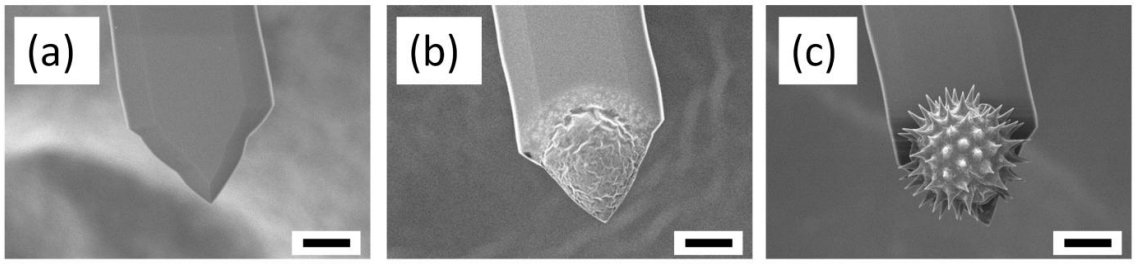

Figure 2.2. AFM colloidal probe at various stages of the fabrication process. Scanning electron micrographs of a) a tipless cantilever, b) a small amount of epoxy applied to the end of the tipless cantilever, and c) a sunflower pollen particle attached to the tipless cantilever with epoxy The scale bars represent 12 μm.

2.3.2.2 Contact Angle Measurements

Static water contact angles were measured at 20 °C on the different substrates using a video contact angle system (AST products 2500XE, Billerica, MA). Nine 1 μL drops of water were dispensed onto different regions of the sample surfaces. Both the

right and left angles between the sample surface and the tangent line to each droplet were measured for each droplet.

2.3.2.3 Scanning Electron Microscopy (SEM)

The pollen AFM probes were characterized by scanning electron microscopy (SEM) (ZeissUltra60 FE-SEM) after all force measurements were finished, at an accelerating potential of 10.0 kV. Probe tips were sputtered with gold and then mounted on metal stubs using carbon tape.

2.4 Results and Discussion

2.4.1 Pollen and Substrate Morphology

Five different substrates were used to examine the effect of surface chemistry on the adhesion forces of each pollen grain. PS was chosen as a model apolar hydrocarbon substrate. PVA and PVAc were chosen to represent organic materials with protic and basic characteristics, respectively. The polymer films used herein exhibited a range of water contact angles (θ_w) of 46°, 61°, and 101° for PVA, PVAc, and PS, respectively. Piranha-etched silicon (Si) is a model inorganic, hydrophilic, and protic surface with $\theta_w \approx 14°$. Piranha-treated Si is known to bear an oxide layer (2−10 nm) consisting of both oxygenated (SiO_x) and hydroxylated (SiOH) silicon. To provide a model metallic substrate as well as to explore the effect of masking silanol groups, a thin (~8 nm) gold coating was applied to the Si wafer ($\theta_w \approx 84°$) (Au-Si) [32]. One potential concern is variation in surface roughness, which might complicate interpretation of differences in chemistry between the substrates. The measured root-mean-square surface roughnesses of the polymer and silicon surfaces fall within a range of 0.3-2.7 nm (Table 2.1). Since the variation in roughness is orders of magnitude smaller than the scale of pollen surface microtopography (Figure 2.3) the effect of these small differences in roughness is likely to be negligible relative to other effects observed herein.

Table 2.1. Surface roughness and static water contact angles of the various substrates. Uncertainties represent ± 95% confidence interval.

Surface	Si	PVA	PVAc	PS
Ra (nm)	0.2 ± 0.1	1.1 ± 0.1	1.3 ± 0.1	2.2 ± 0.2
rms (nm)	0.3 ± 0.1	1.3 ± 0.1	1.7 ± 0.1	2.7 ± 0.2
Contact Angle (^{0})	13.7 ± 1.3	46.2 ± 1.4	60.7 ± 2.9	101.1 ± 3.0

Figure 2.3 shows high-magnification SEM images of surface ornamentations of each non-defatted (with native pollenkitt) and cleaned pollen (without pollenkitt). The cantilevers with pollen grains attached are shown in Figure 2.4, taken after all force measurements were completed. It is noteworthy that no damage to pollen grains was observed under typical applied load forces (2.5 nN, approximately the weight of a single pollen). As reported previously, the pollen grains are not subjected to measurable deformation and do not exhibit compliance under the small loading forces used here [29]. Both olive and poplar pollens exhibit a reticulate exine structure that is characterized by nanoscale raised "bumps" that serve as the outermost protuberances. An example is labeled with an arrow in Figure 2.3A1. The three other pollens had echinate (spiked) microstructures (ragweed, dandelion, sunflower) and were chosen from the same family (Asteraceae) to minimize deviations in sporopollenin composition. Table 2.2 shows the characteristics of each pollen sample, including morphology and size (length and radius determined from SEM) of morphological features (spines or grooves). The radii of the pollen morphological features did not change significantly after the solvent extraction with chloroform/methanol (3:1).

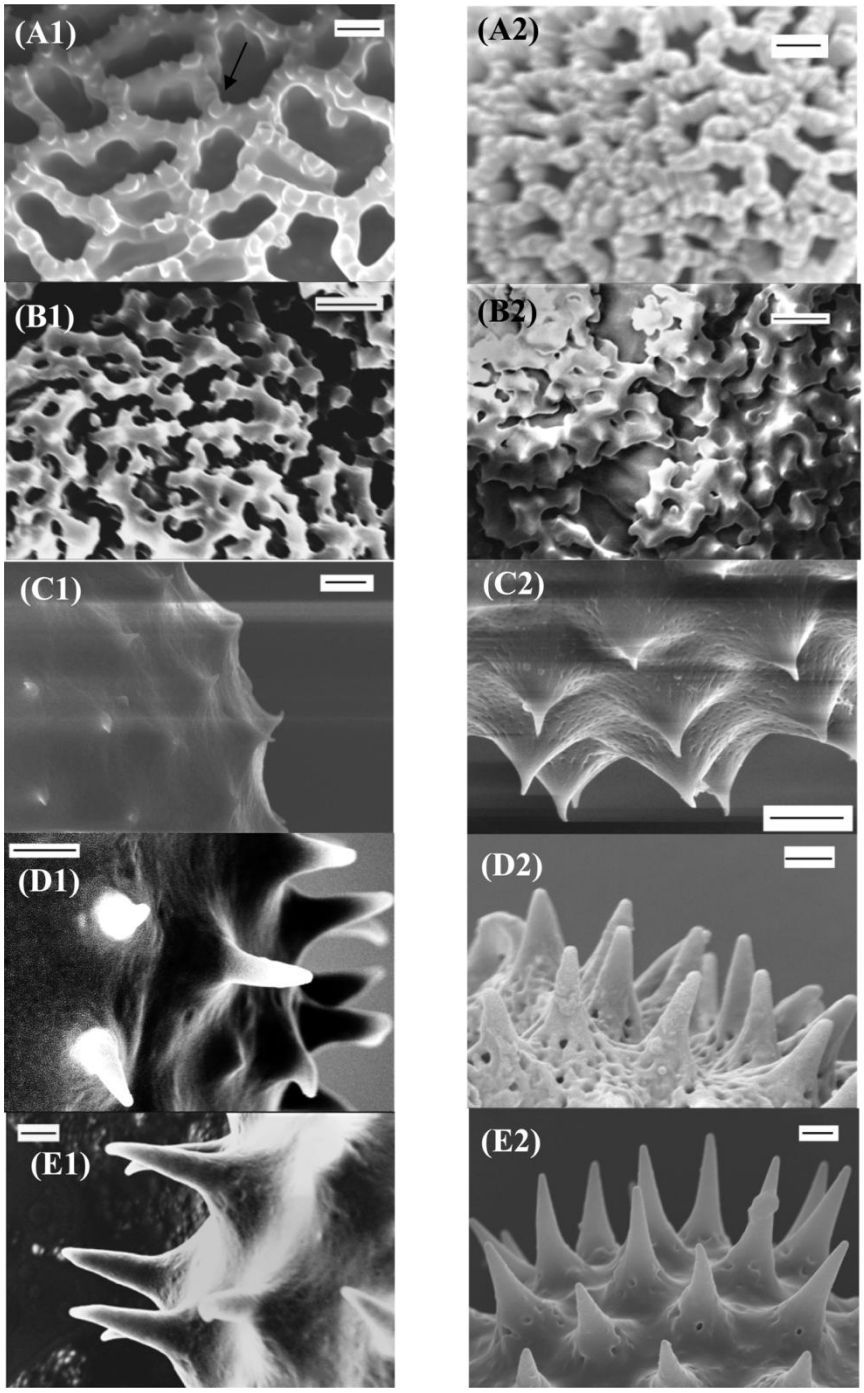

Figure 2.3. Scanning electron micrographs showing details of pollen grain surfaces with and without pollenkitt: A) olive, B) poplar, C) ragweed, D) dandelion, and E) sunflower. Label "1" indicates non-defatted (as received) and "2" indicates that pollens were prewashed by chloroform/methanol (3:1) to remove pollenkitt. The black scale bars indicate 1 µm.

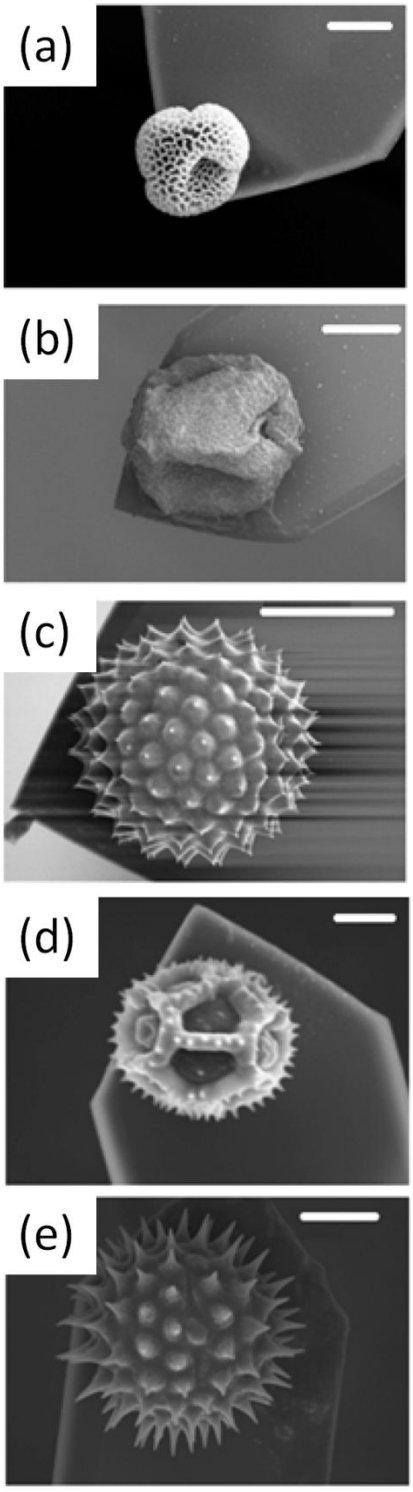

Figure 2.4. Scanning electron micrographs of AFM colloidal probes of cleaned a) olive, b) poplar, c) ragweed, d) dandelion, and e) sunflower pollen grains glued to the end of tipless AFM cantilevers. The white scale bars represent 10 µm.

Table 2.2. Morphology characteristics of pollen samples. The measured height and radius are of tips of reticulate bumps or echinate spines. Spine density is the number of spines per unit area of a sphere with the same radius as the base pollen.

Pollen	Surface Structure	Size (D, μm)	Height (μm)	Radius (nm)	Spike Density (μm^{-2})
Olive	Reticulate	20 ± 3	0.2 - 0.5	50 ± 5	--
Poplar	Reticulate	20 ± 3	0.1 - 0.2	50 ± 5	--
Ragweed	Echinate	15 ± 3	0.5 - 1.0	52 ± 5	0.84
Dandelion	Echinate	25 ± 4	0.8 - 1.3	90 ± 5	0.6
Sunflower	Echinate	30 ± 4	1.5 - 2.0	120 ± 10	0.32

2.4.2 Cleaned Pollen Adhesion

Figure 2.5 shows a typical force-distance curve for cleaned dandelion pollen on the Si surface, which are typical for other substrates investigated herein. Cleaned pollens did not show any evidence of large, long-ranged jump to contact forces, but rather showed short-ranged (a few nanometers) attractions of only several nanonewtons. The magnitude of the snap-on did not vary significantly for different surfaces. "Snap-on" refers to the initial jump to contact, which is caused by attractive forces between the pollen tip and substrate upon approach. During the retraction of cleaned pollens, a sudden pull-off event occurs in which the two solids separate suddenly at the maximum adhesion force. This is clearly indicative of a solid-solid short-ranged adhesion. In the case of cleaned pollens, initial contact with flat surfaces is made at the outermost surface protuberances, which are spines (in the case of echinate species) or bumps (in the case of reticulate species). The cleaned pollen force-distance data indicate that only one external feature (spine or bump) is making contact in each of the force-distance measurements used herein. The conclusion is made from the AFM force-distance curves (Figure 2.5 is one example). These curves just displayed a single contact event. For some AFM pollen probes, the pollen is oriented such that more than one spine contacts at one time, and this

is evident in the force-distance data. We have not utilized such “multiple contact” probes in this study.

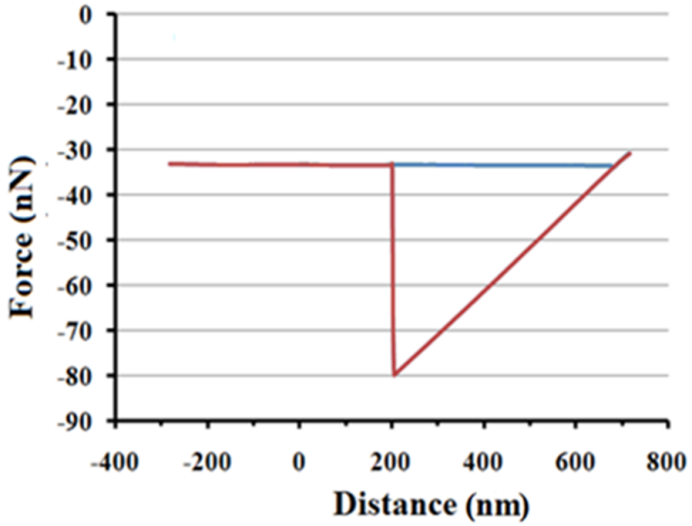

Figure 2.5. Force-distance curve between a cleaned dandelion pollen and a Si substrate. The blue line is the tip approach data and the red line is the tip retraction data.

In the results that follow, the pull-off adhesive force is taken as the difference between the minimum force (maximum absolute value) and the long distance baseline. Figure 2.6 shows the average pull-off adhesion forces of chloroform/methanol-washed pollen grains with different polymer substrates. The distinguishing characteristic of the cleaned pollens is the absence of adhesion force dependence on substrate chemistry. Additionally, the magnitude of the adhesion force is related to the size of the pollen protuberances rather than the size of the pollen particles (Table 2.2).

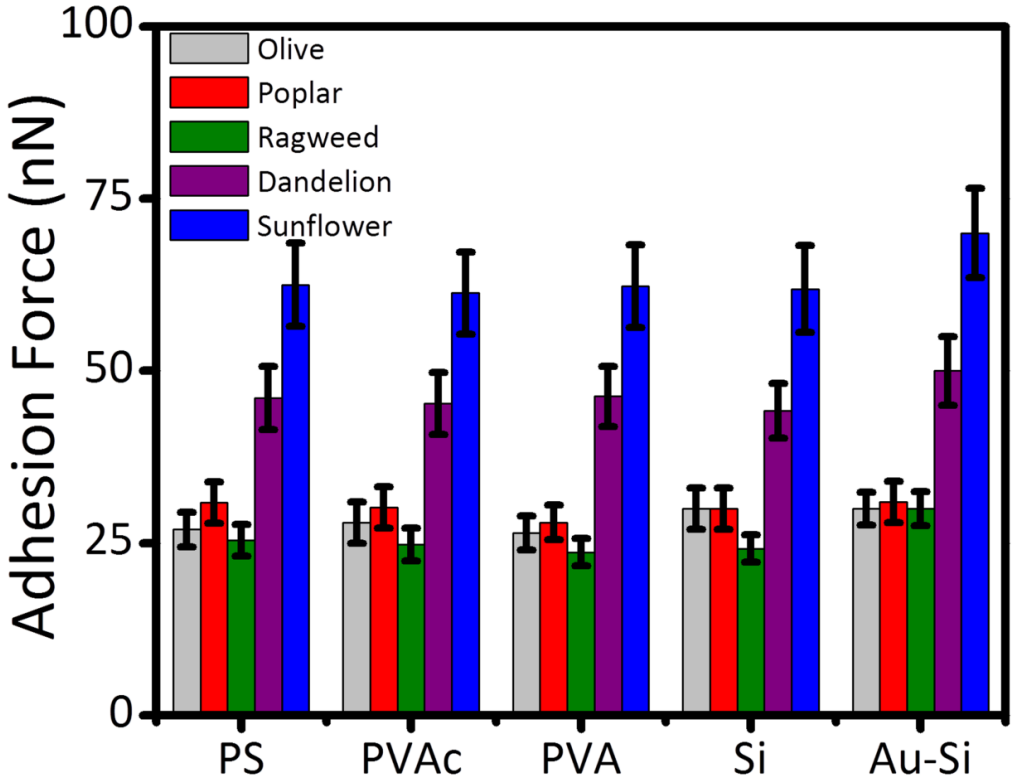

Figure 2.6. Adhesion forces between the cleaned pollen AFM probes and various substrates. Error bars are 95% confidence intervals.

2.4.3 Mechanism of Cleaned Pollen Adhesion

Pollen surface morphology and feature size is expected to affect the adhesion force by altering the contact area between the surface features and other surfaces. If adhesion is governed by VDW forces, then the dependence of adhesion on the size of pollen ornamentations should be approximated well by the Hamaker model in Eq. (2.1) [33]:

$$F_{Hamaker} = \frac{AR}{6d^2} \tag{2.1}$$

where A is the material-dependent nonretarded Hamaker constant, R is radius of contact (estimated as the pollen ornamentation radius from Table 2.2), and d is the cutoff separation distance, taken to be 0.165 nm. According to Eq. (2.1), the adhesion force is

expected to scale proportionately with the exine spine or groove radii. While contact radius at the exact moment of measurement is not directly available from AFM force-distance measurements, the contact radius is estimated as the radius of outermost protuberances determined from SEM and listed in Table 2.2. Figure 2.7 shows a plot of adhesion force (Force) versus protuberance radius (Radius) for all five species on silica, indicating an excellent linear fit with an A value of 8.5 x 10^{-20} J.

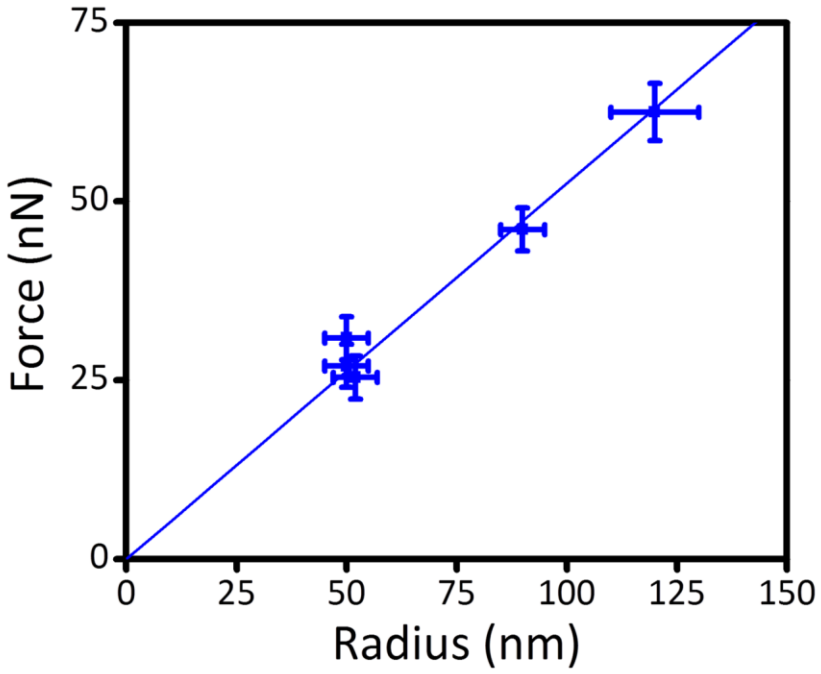

Figure 2.7. Cleaned pollen adhesion force on silicon versus feature size radius. Line is linear regression from which a Hamaker constant (A) is estimated.

The Hamaker constant of sporopollenin can be estimated by using a combining relation based on the contributions of each medium in Eq. (2.2):

$$A_{132} \approx \left(\sqrt{A_{11}} - \sqrt{A_{33}}\right)\left(\sqrt{A_{22}} - \sqrt{A_{33}}\right) \tag{2.2}$$

where A_{11} is the Hamaker constant for sporopollenin, A_{22} is the Hamaker constant for the substrate, A_{33} is the Hamaker constant for air, and A_{132} is the effective nonretarded Hamaker constant for sporopollenin and the substrate interacting across air [33]. Using this relation, the nonretarded Hamaker constant of sporopollenin is 1.1 x 10^{-19} J. These

values are larger than those of organic small molecules, A ≈ (4-6) x 10^{-20} J, e.g., toluene = 5.4 x 10^{-20} J and propylene oxide = 4.0 x 10^{-20} J, and are comparable to those of other natural and synthetic hydrocarbon polymers. For example, the A values for several such polymers have been reported as 8.6 x 10^{-20} J (natural rubber), 8.9 x 10^{-20} J (PVAc), and 9.8 x 10^{-20} J (PS) [34]. It is well-known that Hamaker constants of n-alkanes increase as the number of carbons increases and reach a plateau value near (7-8) x 10^{-20} J as the number of carbons exceeds 20 [34]. This value of sporopollenin Hamaker (1.1 x 10^{-19} J) is consistent with the reported structure and chemistry of sporopollenin as a crosslinked mixture of long-chain fatty acids (number of carbons >13) and oxygenated aromatic moieties [17, 18].

The presence of nanoscale protuberances on pollens is likely a mechanism for reducing adhesion. Compared to spherical particles of similar sizes (tens of microns), surface protuberances (tens of nanometers) effectively reduce the magnitude of adhesion by several orders of magnitude. In nature, the role of surface morphology in promoting pollen dispersal and transport during pollination must be considered with the contributions from the natural liquid pollenkitt coating. In the absence of pollenkitt, however, pollens possessing structure-dependent adhesion serve as potential model biotemplates for applications requiring the manipulation of microparticles possessing nanoscale interactions with select surfaces.

2.5 Conclusions

We report AFM adhesion measurements of five pollen species with a series of test surfaces representing unique combinations of solid surface morphologies. The results indicate that the surface morphology (size and shape of echinate or reticulate features) provides pollens with a mechanism for tuning the adhesion force within a magnitude of ~30-60 nN. Cleaned pollen grains (with pollenkitt removed) had adhesion strengths that were independent of surface chemistry and scalable with the tip radius of the pollen's

ornamentation features, according to the Hamaker model. We propose that the structural mechanisms observed for natural pollen adhesion may serve as a useful model for the design of novel synthetic microparticle adhesion strategies.

2.6 References

1. Rimai, D., L.H. Sharpe, and Adhesion Society. Meeting, Advances in particle adhesion1996, Amsterdam: Gordon and Breach. viii, 216 p.

2. Jaiswal, R.P. and S.P. Beaudoin, Nanoparticle adhesion models: applications in particulate contaminant removal from extreme ultraviolet lithography photomasks. Journal of Adhesion Science and Technology, 2011. 25(8): p. 781-797.

3. Cooper, K., A. Gupta, and S. Beaudoin, Simulation of the adhesion of particles to surfaces. Journal of Colloid and Interface Science, 2001. 234(2): p. 284-292.

4. Komvopoulos, K. and W. Yan, Three-dimensional elastic-plastic fractal analysis of surface adhesion in microelectromechanical systems. Journal of tribology, 1998. 120(4): p. 808-813.

5. Mizes, H., Surface roughness and particle adhesion. The Journal of Adhesion, 1995. 51(1-4): p. 155-165.

6. Du, Y., et al., Directed assembly of cell-laden microgels for fabrication of 3D tissue constructs. Proceedings of the National Academy of Sciences, 2008. 105(28): p. 9522-9527.

7. Stassi, S. and G. Canavese, Spiky nanostructured metal particles as filler of polymeric composites showing tunable electrical conductivity. Journal of Polymer Science Part B: Polymer Physics, 2012. 50(14): p. 984-992.

8. Huang, Y., et al., Controllable Underwater Oil-Adhesion-Interface Films Assembled from Nonspherical Particles. Advanced Functional Materials, 2011. 21(23): p. 4436-4441.

9. Shu, S., S. Husain, and W.J. Koros, A general strategy for adhesion enhancement in polymeric composites by formation of nanostructured particle surfaces. The Journal of Physical Chemistry C, 2007. 111(2): p. 652-657.

10. Rimai, D., M. Dejesus, and D. Weiss, The effect of surface-adhering nanoclusters on the adhesion and cohesion of micrometer-size particles. Journal of Adhesion Science and Technology, 2008. 22(5-6): p. 529-543.

11. Helgeson, M.E., S.C. Chapin, and P.S. Doyle, Hydrogel microparticles from lithographic processes: Novel materials for fundamental and applied colloid science. Current Opinion in Colloid & Interface Science, 2011. 16(2): p. 106-117.

12. Ping, L., et al., Hydrothermal synthesis of TiO2 hollow spheres using rapeseed pollen grains as template. Journal of Inorganic Materials, 2008. 23(1): p. 49-54.

13. Fang, Y., et al., Syntheses of nanostructured Cu-and Ni-based micro-assemblies with selectable 3-D hierarchical biogenic morphologies. Journal of Materials Chemistry, 2012. 22(4): p. 1305-1312.

14. Thio, B.J.R., K.K. Clark, and A.A. Keller, Magnetic pollen grains as sorbents for facile removal of organic pollutants in aqueous media. Journal of hazardous materials, 2011. 194: p. 53-61.

15. Traidl-Hoffmann, C., et al., Impact of pollen on human health: more than allergen carriers? International archives of allergy and immunology, 2003. 131(1): p. 1-13.

16. Domínguez, E., et al., Pollen sporopollenin: degradation and structural elucidation. Sexual Plant Reproduction, 1999. 12(3): p. 171-178.

17. Ivleva, N.P., R. Niessner, and U. Panne, Characterization and discrimination of pollen by Raman microscopy. Analytical and Bioanalytical Chemistry, 2005. 381(1): p. 261-267.

18. Kano, H. and H.-o. Hamaguchi, Vibrational imaging of a single pollen grain by ultrabroadband multiplex coherent anti-stokes Raman scattering microspectroscopy. Chemistry Letters, 2006. 35(10): p. 1124-1125.

19. Scott, R.J. and A.D. Stead, Pollen exine - the sporopollenin enigma and the physics of pattern, in Molecular and cellular aspects of plant reproduction1994, New York : Cambridge University Press: Cambridge ;. p. xii, 315 p.

20. Brooks, J. and G. Shaw, Chemical structure of the exine of pollen walls and a new function for carotenoids in nature. 1968.

21. Brooks, J. and G. Shaw, Geochemistry of sporopollenin. Chemical Geology, 1972. 10(1): p. 69-87.

22. Knoll, F., Über Pollenkitt und Bestäubungsart: Ein Beitrag zur experimentellen Blütenökologie. Zeitschrift für Botanik, 1930. 23: p. 609-675.

23. Blackmore, S., et al., Pollen Wall Development in Flowering Plants. New Phytologist, 2007. 174(3): p. 483-498.

24. Howlett, B., R. Knox, and J. Heslop-Harrison, Pollen-wall proteins: release of the allergen antigen E from intine and exine sites in pollen grains of ragweed and Cosmos. Journal of Cell Science, 1973. 13(2): p. 603-619.

25. Pacini, E. and M. Hesse, Pollenkitt – its composition, forms and functions. Flora - Morphology, Distribution, Functional Ecology of Plants, 2005. 200(5): p. 399-415.

26. Pacini, E., Tapetum character states: analytical keys for tapetum types and activities. Canadian Journal of Botany, 1997. 75(9): p. 1448-1459.

27. Meredith, J.C., A. Karim, and E.J. Amis, High-throughput measurement of polymer blend phase behavior. Macromolecules, 2000. 33(16): p. 5760-5762.

28. Dobson, H.E.M., Survey of Pollen and Pollenkitt Lipids -- Chemical Cues to Flower Visitors? American Journal of Botany, 1988. 75(2): p. 170-182.

29. Thio, B.J.R., J.-H. Lee, and J.C. Meredith, Characterization of ragweed pollen adhesion to polyamides and polystyrene using atomic force microscopy. Environmental science & technology, 2009. 43(12): p. 4308-4313.

30. Burnham, N., et al., Comparison of calibration methods for atomic-force microscopy cantilevers. Nanotechnology, 2003. 14(1): p. 1.

31. Hutter, J.L. and J. Bechhoefer, Calibration of atomic-force microscope tips. Review of Scientific Instruments, 1993. 64: p. 1868.

32. Sharma, A. and G. Reiter, Instability of thin polymer films on coated substrates: rupture, dewetting, and drop formation. Journal of Colloid and Interface Science, 1996. 178(2): p. 383-399.

33. Israelachvili, J., Intermolecular and Surface Forces. 2nd ed: Academic Press: London, 1992.

34. Croucher, M.D. and M.L. Hair, Hamaker constants and the principle of corresponding states. The Journal of Physical Chemistry, 1977. 81(17): p. 1631-1636.

CHAPTER 3

PREPARATION OF METAL NANOPARTICLE-COATED POLLEN PARTICLES FOR ENHANCED SHORT-RANGE VAN DER WAALS ADHESION AND RAMAN SCATTERING

3.1 Overview

In this chapter, we utilize pollen as a bio-organic core material for the first reported ex-situ preparation of nanoparticle (NP)-pollen composite particles. Electrostatic interactions facilitated the heteroaggregation of gold nanoparticles (AuNPs) and silver nanocubes (AgNCs) onto the surface of aminosilane-functionalized pollen particles. Metal NP surface coverage was controlled by varying the NP concentration and pH environment. Atomic force microscopy (AFM) was utilized to investigate the adhesion behavior of NP-coated pollen particles compared to uncoated pollen particles. While the magnitude of short-range van der Waals (VDW) adhesion typically scales with pollen spine tip radius, NP-covered spine tips provided multiple contacts with substrates and exhibited enhanced VDW adhesion. Raman measurements revealed that NP-covered pollen particles displayed potential for use as surface enhanced Raman scattering (SERS) substrates by enhancing the Raman signal of PVP chains bound to the metal NPs. This chapter provides a framework for utilizing pollen-NP composites for enhanced adhesion and as SERS substrates by selecting appropriate pollen particles, NP chemistries, and NP sizes.

3.2 Introduction

Interest in microparticle adhesion has been driven by advances in applications involving ultrafiltration, inhalation therapy, fouling processes, dry powder dispersions, and cell therapy [1-6]. The presence of microparticle surface asperities can provide control over particle-particle and particle-substrate interactions. Chapter 2 demonstrated

the feasibility of using pollen grains as model particles for microstructure-controlled adhesion. To this point, pollen's chemically-resistant, uniquely-structured exine shell has been employed for applications in microencapsulation, emulsion stabilization, and fillers in composite films [7-9]. As biotemplates, the in-situ deposition of metal and metal oxides into the sporopollenin shell has proved useful in Raman scattering, waste treatment, Li-ion batteries, and gas sensing technology [10-13]. However, the ex-situ deposition of metal onto the sporopollenin shell has yet to be demonstrated. The successful attachment of metal NPs to pollen's shell and spines could potentially be used to modify pollen adhesion due to the introduction of nano-scale surface roughness [14-16].

Applications involving the incorporation of metal nanoparticles (NPs) into core polymeric particles are of particular interest in catalysis, surface enhanced Raman scattering (SERS), drug delivery, bioassays, and medical imaging [17-21]. Gold (Au) and silver (Ag) NPs are especially attractive because of their biocompatibility, optical properties, electronic properties, and magnetic properties [22-25]. SERS is a useful technique for significantly enhancing the Raman signals of molecules which have been attached to nanometer sized metallic structures [26]. SERS enhancement factors have been reported as high as 10-15 orders of magnitude for single-molecule SERS experiments on Ag and Au colloids [27]. The Raman enhancement mechanism is due to the excitation of localized surface plasmons (LSPs), charge density oscillations confined to metallic NPs and metallic nanostructures, by an electric field (light) at an incident wavelength where resonance occurs [28]. Additionally, metal electron-mediated Raman resonance occurs via a charge transfer intermediate state at Raman active sites [26, 29]. Immobile substrates, i.e., metal NPs deposited on polymer films, microparticles, and roughened surfaces, are typically used as SERS substrates [30-32]. Utilizing a naturally-derived core material, metal NP-coated pollen particles can potentially serve as sustainable SERS substrates for biological and chemical sensors [33, 34].

In this chapter, the ex-situ attachment of preformed metal NPs to pollen's exine shell via electrostatic interactions has a two-fold purpose: 1) to modify the adhesive properties of pollen particles via nanoparticle-mediated contact and 2) to demonstrate the potential of NP-pollen composites as SERS substrates. The framework for preparing NP-pollen composites provides a means for tailoring pollen morphology, NP chemistry, and NP size for modified adhesion and Raman enhancement.

3.3 Experimental

3.3.1 Materials and Procedure

3.3.1.1 Materials

Native defatted ragweed (*Ambrosia artemisiifolia*) pollen grains were purchased from Greer Laboratories (Lenoir, NC USA) and stored at 4 °C. Defatted indicates that the manufacturer used an ethyl ether (ACS grade) washing step to partially remove the pollen's pollenkitt. Deionized water (DIW, 18.2 MΩ cm, pH 6.4) was prepared in a Barnstead Easypure RoDi purification system. Collaborators contributed 30 nm gold nanoparticles (AuNPs, 29 ± 2 nm by scanning electron microscopy (SEM), 6.9×10^{9} particles mL^{-1}) and 60 nm silver nanocubes (AgNCs, 57 ± 2 nm by SEM, 9.7×10^{15} particles mL^{-1}) prepared by a previously described method [18].

3.3.1.2 Pollen Treatments

3.3.1.2.1 Base/Acid Pollen Treatment

A 1 g batch of defatted ragweed pollen was treated with 100 mL of 6 w/v% potassium hydroxide (EMD Millipore, Billerica, MA USA) in DIW at 23 °C for 6 h. At the end of the treatment, the basic solution was neutralized with hydrochloric acid (38%, BDH Chemicals Ltd., Radnor, PA USA) and centrifuge-washed with boiling DIW (three times) and boiling ethanol (100%, VWR International, Inc., West Chester, PA USA) (three times). The base-treated pollen was then dried in a convection oven at 30 °C for two days. Dried base-treated ragweed pollen was then added to 100 mL of ortho-

phosphoric acid (85%, EMD Millipore, Billerica, MA USA) at 50 °C for 7 days. At the end of the treatment, the acidic solution was neutralized with NaCl and centrifuge-washed with boiling DIW (three times) and boiling ethanol (three times). The base/acid-treated ragweed pollen (BA-RW, $8.8x10^4$ pollen μL^{-1} by optical microscope (Olympus BX51 microscope, Olympus America, Inc., Center Valley, PA USA)) was stored in an ethanol solution at 4 °C.

3.3.1.2.2 APTES Pollen Treatment

A 0.08 g batch of BA-RW pollen was dried in a vacuum oven at 100 °C for 24 h. The dried pollen was then dispersed in 70 mL of anhydrous toluene (99.8%, Sigma-Aldrich, Co., St. Louis, MO USA) and sealed in a three-neck flask equipped with two rubber stoppers and a condenser sealed with rubber stopper. An argon atmosphere was created by inserting an argon feed (70 mL min^{-1}) into one of the rubber stoppers and inserting a syringe needle into the rubber stopper atop the condenser as a gas purge. After 30 min of purging, 2 mL of 3-aminopropyltriethoxysilane (APTES, 99%, Sigma-Aldrich, Co., St. Louis, MO USA) was injected into the pollen/toluene suspension through the third, unused rubber stopper and the temperature was increased to 85 °C. The mixture was stirred for 24 h at 85 °C and an argon flow rate of 70 mL min^{-1}. At the end of the treatment, the solution was centrifuge-washed with toluene (three times), n-heptane (Honeywell J&B Chemicals, Muskegon, MI USA) (three times), and ethanol (three times). The APTES-treated ragweed pollen (APTES-RW, $5.2x10^4$ pollen μL^{-1} by optical microscope) was stored in an ethanol solution at 4 °C.

3.3.1.3 Pollen-Nanoparticle Composite Preparation

A 5 µL portion of APTES-ragweed pollen in ethanol was transferred into a 1.7 mL centrifuge tube and dried in a 30 °C convection oven for 2 days. The dried APTES-RW pollen was resuspended in 500 µL of DIW and 500 µL of the desired metal colloidal dispersion was added and vortex-mixed for 30 s followed by agitation using a rotational

shaker for 24 h. The mixture was then washed with DIW via three centrifugation cycles. The total mixture volume was kept constant for all samples. Metal nanoparticle (NP) surface coverage was controlled by adjusting the ratio of the number of metal NPs to APTES-RW particles used. Samples prepared with an increased pH required that the pH of the individual components (APTES-RW or metal NP in DIW) were adjusted prior to mixing by adding sodium hydroxide (NaOH, BDH Chemicals Ltd., Radnor, PA USA) and measured using a pH meter (Fisher Science Education, Thermo Fisher Scientific, Inc., Waltham, MA USA). Metal NP surface coverage was estimated from SEM images using ImageJ software.

3.3.1.4 Substrate Preparation

Five types of substrates were utilized for adhesion studies: silicon (Si), polyvinyl alcohol (PVA), polyvinyl acetate (PVAc), polystyrene (PS), and gold-coated silicon (Au-Si). The Si substrates (Silicon, Inc., Boise, ID USA) were piranha-etched using a solution of 75 vol.% sulfuric acid (97 wt.%, BDH Chemicals Ltd.) and 25 vol.% hydrogen peroxide (30 wt.%, BDH Chemicals Ltd.) at 80°C for 1 h. The polymer substrates (PVA, PVAc, and PS) consisted of blade-cast polymer films on the cleaned Si substrates. Solutions comprised of 15 wt.% PS (MW = 100,000, Avocado Research Chemicals, Lancashire UK) in toluene (Sigma-Aldrich, St. Louis, MO USA), 20 wt.% PVAc (MW = 50,000, Alfa Aesar, Ward Hill, MA USA) in tetrahydrofuran (THF, BDH Chemicals Ltd.), or 3 wt.% PVA (MW = 89,000-98,000, Sigma-Aldrich) in hexafluoroisopropanol (HFIP, TCI America, Portland, OR USA) were used during blade casting. Blade casting (3540 Bird Film Applicator, Elcometer, Rochester Hills, MI USA) was conducted using a gap height of 1.2 mm, followed by slow drying under a saturated solvent environment for 2 days at 23 °C. The films were then air-dried for 2 days at 23 °C, followed by annealing in a vacuum oven for 1 day at 100 °C. The resulting polymer films possessed thicknesses

ranging from 20 to 100 μm and completely covered the underlying Si substrate. Au-Si substrates were prepared by sputtering a ~8 nm gold coating onto cleaned Si substrates.

The surface roughness of each type of substrate was evaluated with a scanning probe microscope (Dimension 3100 SPM equipped with a Nanoscope V Controller, Veeco Instruments, Inc., Plainview, NY USA) operated in tapping mode at 200-400 kHz using a pyramidal tip silicon cantilever (Applied NanoStructures, Inc., Santa Clara, CA USA). For each particular substrate, 3 randomly-located scans (10 μm x 10 μm) were conducted, with each scan area split into 4 sectors. The average roughness value for a given substrate was obtained from analysis of these 12 sectors.

3.3.2 Experimental Methods

3.3.2.1 Pollen Characterization

The pollen chemistries were characterized by Fourier transform infrared (FTIR) spectroscopy using a Vertex 80v FTIR spectrometer (Bruker Optics, Inc., Billerica, MA USA). Measurements were averaged over 64 scans and were collected in the mid-IR range, 4000-400 cm^{-1} with a resolution of 4 cm^{-1}, using a KBr beamsplitter. FTIR samples were prepared by mixing a small amount of dry pollen powder with 100 mg of potassium bromide (FTIR grade, Alfa Aesar) in a mortar and pressing the mixture into a pellet. The FTIR software was used to baseline correct each spectrum. Pollen surface morphologies were characterized by scanning electron microscopy (SEM) (ZeissUltra60 FE-SEM, Carl Zeiss SMT, Ltd., Thornwood, NY USA) after all force measurements were completed, at an accelerating potential of 5.0 kV. SEM samples were sputtered with gold and then mounted on metal stubs using carbon tape.

3.3.2.2 Zeta Potential Measurements

Metal NP zeta potentials were measured on a Malvern Zetasizer Nano S90. For every pH condition, four measurements (each measurement was averaged over 20 runs) were taken and averaged. Pollen zeta potentials were measured using a SurPASS

electrokinetic analyzer (Anton Paar USA, Inc., Ashland, VA USA) equipped with a rectangular adjustable gap cell (20 mm x 10 mm). Due to the sedimentation of the larger pollen particles, measuring their zeta potential requires the measurement of streaming potential via the electrokinetic analyzer. By forcing an electrolyte solution through a slit between two pollen-coated surfaces, the charges in the mobile part of the electric double layer are carried toward one end of the slit and create a streaming potential [35]. Accumulating ions with one sign at one end of the slit generates a potential difference between the two ends of the slits. This potential difference opposes the mechanical transfer of charge and causes back conduction by ion diffusion and electro-osmotic flow [36]. The streaming potential is measured when the back flow of ions, known as the leak current, reaches a steady state and equals the streaming current [37]. Streaming current is then related to zeta potential via the Helmholtz-Smoluchowski equation, calculated by in Eq. (3.1):

$$\zeta = \frac{dU}{dp}\frac{\eta}{\varepsilon_r \varepsilon_o}\frac{L}{A}\frac{1}{R} \tag{3.1}$$

where $\frac{dU}{dp}$ is the slope of streaming potential versus pressure, η is the electrolyte viscosity, ε_r is the relative liquid permittivity, ε_o is the vacuum permittivity, L is the length of the streaming channel, A is the cross-section of the streaming channel, and R is the DC resistance inside the measuring cell [38]. A standard cell is available for measuring the streaming potential of particles greater than 25 µm, however the ragweed pollen particles in this study are ~15 µm. Therefore, pollen substrates were prepared by attaching dried pollen particles to glass slides (20 mm x 10 mm, 0.16-0.19 mm thickness) using Tempfix (Electron Microscopy Sciences, Hatfield, PA USA), a thermoplastic adhesive. Two pollen substrates were then attached to the adjustable gap cell using double-sided adhesive tape. The pH and conductivity were calibrated before the start of each run of experiments and a DIW rinse was performed before switching to a new pH environment.

During a measurement, the pressure was linearly ramped from 0-300 mbar in both directions between the channel (~100 μm width). Two cycles of pressure ramping in both directions were used to obtain four zeta potentials, which were then averaged. All zeta potentials were measured in the presence of 1 mM sodium chloride (NaCl, VWR International, Inc.) and at a temperature of 23 °C.

3.3.2.3 Substrate Preparation and Characterization

The substrate preparation and characterization methods from Chapter 2 were utilized.

3.3.2.4 Adhesion Measurements

Adhesion measurements were conducted using AFM probes consisting of a single particle attached to an atomic force microscope (AFM) cantilever. A small amount of epoxy resin (Epoxy Marine, Loctite, Westlake, OH USA) was used to attach a given particle to a tipless silicon AFM cantilever (FORT-TL, Applied NanoStructures, Inc.). For each type of pollen particle (ragweed, BA-RW, AP-RW, Au/AP-RW, Ag/AP-RW), three single-particle-bearing cantilever probes were prepared (for a total of 15 particle-cantilever probes). The spring constants, as determined with the scanning probe microscope, of the cleaned ragweed pollen-bearing, BA-RW pollen-bearing, AP-RW pollen-bearing, Au/AP-RW pollen-bearing, and Ag/AP-RW pollen-bearing cantilever probes fell in the ranges of 0.1-0.6 N m^{-1}, 0.1-0.2 N m^{-1}, 1.2-1.5 N m^{-1}, 1.2-1.7 N m^{-1}, and 1.2-1.6 N m^{-1}, respectively. The adhesion force between an individual ragweed pollen particle and a particular substrate was evaluated with the scanning probe microscope operated in contact mode. For each particular particle-cantilever probe and particular substrate, 20 separate force-distance scans were randomly obtained, and the depth of adhesion wells upon retraction were averaged. The load force applied during the contact adhesion measurements was 2.5 nN. The ambient relative humidity in the laboratory during the adhesion measurements ranged from 30-35%.

3.3.2.5 Raman Measurements

A Raman microscope (Thermo Nicolet Almega Dispersive Raman, Thermo Fisher Scientific, Inc.) with a 785 nm laser excitation was used for surface Raman measurement under 50x magnification. Measurements were taken from a 5 µm x 5 µm spot area on the surface of a single pollen particle at an accumulation time of 1 s with 30 scans.

3.4 Results and Discussion

3.4.1 Pollen Preparation

Pollen particles, as found in nature, are known to contain a relatively large mass of degradable material (up to 80 % w/w) [39]. Removing pollen's degradable material (Figure 3.1a) associated with the intracellular triacylglycerols and phospholipids, pollenkitt's medium- and long-chain fatty acids, and the polysaccharides of the intine allows for the isolation of the insoluble sporopollenin shell [40]. Using a conventional isolation method, defatted ragweed (DRW) pollen was treated with potassium hydroxide and phosphoric acid [8, 41, 42]. DRW pollen was used as a starting material, rather than non-defatted pollen, because an ethyl ether washing was performed by the manufacturer to partially remove the pollenkitt coating. At the completion of the treatment, the base/acid-treated ragweed (BA-RW) pollen is essentially a hollow, chemically-stable sporopollenin shell (Figure 3.1b). Comparing the FTIR spectra of DRW and BA-RW pollen in Figure 3.2 confirms the removal of all soluble components. Using the C-H stretch at 2975-2950 cm^{-1} and 2885-2865 cm^{-1} as a reference, the removal of hydroxyl-rich fatty acids, polysaccharides, and lipidic components results in a significantly reduced and narrowed O-H stretch at 3600-3000 cm^{-1} [43]. Again using the C-H stretch as a comparison, the carbonyl (C=O) stretch is reduced in the BA-RW after removal of fatty acids and triacylglycerols. The C=O stretch also shifts from 1665 cm^{-1} in DRW to 1704 cm^{-1} with a shoulder at 1651 cm^{-1} in BA-RW, likely indicating the presence of free

unconjugated carbonyl groups. Cellulose and hemicellulose from pollen's intine possess characteristic peaks corresponding to polysaccharides at 1200-900 cm^{-1}, C-H vibrations at 1316 cm^{-1}, ether (C-O-C) vibrations at 1157 cm^{-1}, and C-O stretches at 1059 cm^{-1} [44-46]. From the FTIR spectra, it is evident that this cellulosic fingerprint has been reduced after the base/acid treatment. Successful isolation of ragweed's insoluble sporopollenin generates a stable shell with many potential uses.

From the FTIR spectrum of BA-RW (Figure 3.2), it is apparent that the sporopollenin shell is rich in hydroxyl groups. As a result, an abundance of reaction sites exist for functionalizing BA-RW with 3-aminopropyltriethoxysilane (APTES) (AP-RW in Figure 3.1c), using a standard protocol [47-49]. Comparing the FTIR spectra of BA-RW with AP-RW in Figure 3.2 confirms the successful functionalization with APTES. The appearance of a shoulder at 3294 cm^{-1} is due to the NH_2 stretching vibration, a peak at 1650 cm^{-1} due to the N-H bending vibration, a peak at 1121 cm^{-1} and 1051 cm^{-1} due to Si-O-Si stretching, and a peak at 696 cm^{-1} due to Si-O-Si asymmetric stretching confirms the successful adsorption of APTES onto the sporopollenin shell [50, 51].

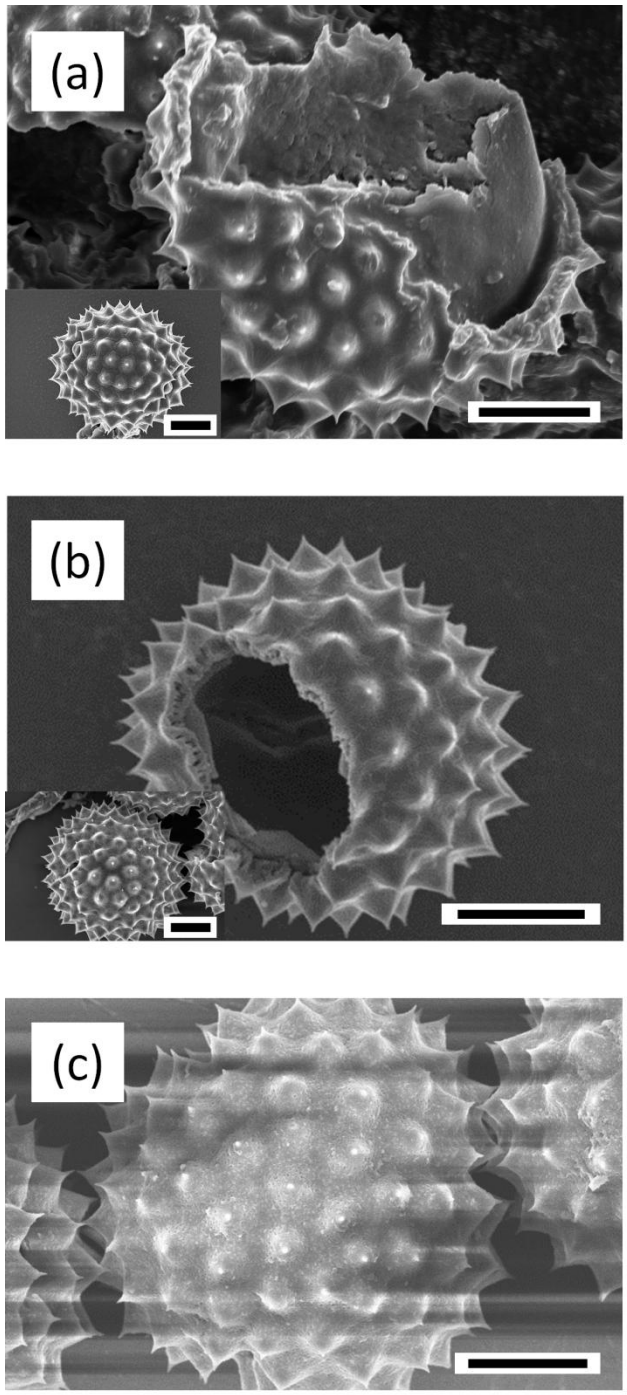

Figure 3.1. Scanning electron micrographs of: a) a DRW pollen broken with liquid nitrogen (inset: intact DRW pollen grain), b) a BA-RW pollen broken with liquid nitrogen (inset: intact BA-RW pollen grain), and c) an AP-RW pollen grain. Scale bars indicate 5 µm.

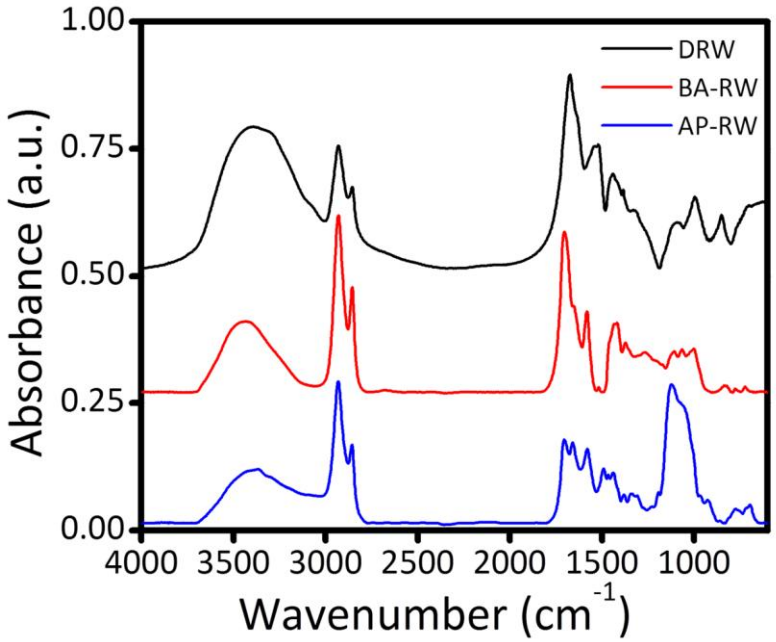

Figure 3.2. FTIR spectra of DRW, BA-RW, and AP-RW pollen.

Table 3.1. Size of ragweed pollen's characteristic features after exine shell isolation and APTES functionalization.

	Particle Diameter (μm)	Tip Radius (nm)
Cleaned RW	15 ± 3	52 ± 5
BA-RW	14 ± 1	45 ± 4
AP-RW	15 ± 1	47 ± 6

The durability of the ragweed exine shell is assessed by observing the pollen size and spike tip radius after each treatment (Table 3.1). The pollen diameter and spike tip radius of cleaned ragweed pollen, from Chapter 2, is used as a reference. The pollen diameters and spike tip radii after the base/acid treatment and the APTES functionalization are nearly unchanged from the cleaned ragweed pollen dimensions. This conservation of ragweed pollen surface features maintains pollen's utility as a model bioparticle.

3.4.2 Pollen-Nanoparticle Composite Preparation

Utilizing sporopollenin as a core material for NP-pollen composites can be accomplished via electrostatic heteroaggregation. Figure 3.3a displays the zeta potentials of 30 nm gold nanoparticles (AuNPs) and 60 nm silver nanocubes (AgNCs), capped by PVP, over a range of pH conditions (6.4, 8.9, 10.6, and 11.4) in the presence of 1 mM NaCl. The zeta potentials of both nanoparticles were consistently less than -25 mV, indicating the stability of AuNP and AgNC dispersions. The metal NPs prepared for this study were synthesized in the presence of polyvinylpyrrolidone (PVP). PVP is a widely used capping agent for its ability to promote metal reduction onto specific crystal faces (shape-controlling reducing agent) and prevent metal particle aggregation (steric hinderance and electrostatic repulsion) [52-54]. PVP facilitates the transfer of C=O n-electrons from a nucleophilic PVP molecule to an electrophilic nanoparticle causing a sharing of localized surface charge density [55, 56]. The accumulation of n-electrons at the surface of the NP results in a negative zeta potential that aids in stabilizing the colloidal dispersion and preventing flocculation [57].

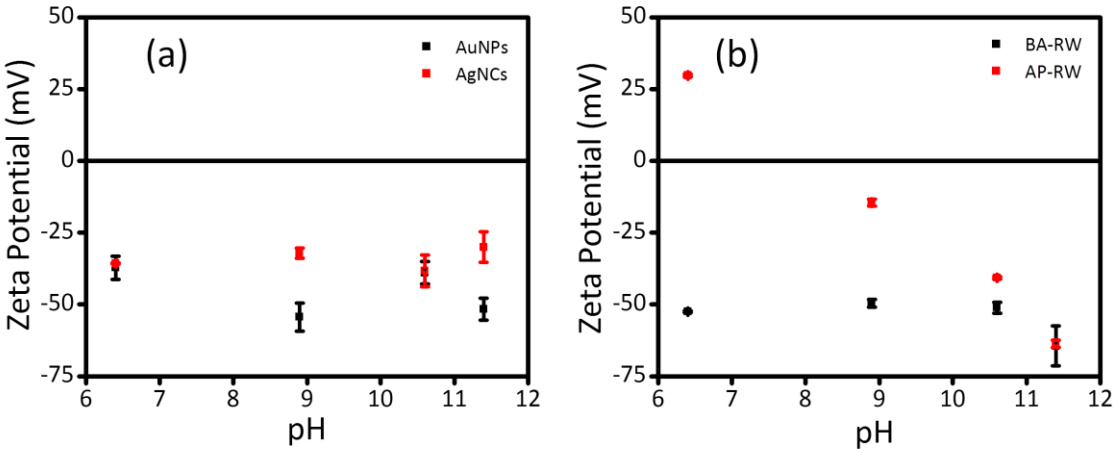

Figure 3.3. Zeta potentials of: a) BA-RW and AP-RW pollen and b) AuNPs and AgNCs at various pH conditions in the presence of 1 mM NaCl.

The zeta potentials of BA-RW pollen, in Figure 3.3b, are less than -50 mV at pH conditions greater than 6 and support the presence of carboxyl groups. This is in agreement with the knowledge that the isolated sporopollenin is known to contain carboxylic acid groups capable of imparting a negative surface charge to pollen via its deprotonation in pH environments above its pKa (~2-5) [8, 58, 59]. Functionalizing sporopollenin with APTES provides a means for imparting a positive surface charge to pollen via the protonation of amine groups (terminal primary amine pKa ~9.5-10.8) [60-63]. The zeta potentials of AP-RW pollen, in Figure 3.3b, vary from +30 mV at pH 6.4 to -66 mV at pH 11.4. Additionally, the isoelectric point occurs at pH 8-9. The Helmholtz-Smoluchowski theory operates under the main assumptions that a uniform surface charge exists along the nonporous flat surface under investigation [36, 64, 65]. Because ragweed pollen particles possess nanoscale surface pores, roughness created from 500-1000 nm tall spikes, and roughness created by the packing of ~15 μm pollen particles onto a planar surface, the measured zeta potential of pollen particles is likely an effective zeta potential rather than a true zeta potential. Although the magnitude of measured pollen zeta potentials may deviate from true pollen zeta potentials, the sign and trend of zeta potential still has value in studying the role of electrostatics in heteroaggregation.

When negatively charged AuNPs and AgNCs are mixed with the negatively charged BA-RW at pH 6.4 at varying ratios of metal NPs to pollen particles, no heteroaggregation occurs (Figure 3.4). When negatively charged AuNPs and AgNPs are mixed with positively charged AP-RW at pH 6.4 at varying ratios of metal NPs to AP-RW pollen particles, the metal NP coverage on the surface of AP-RW increases at increasing ratios of metal NPs to pollen particles (Figure 3.5). The metal NP surface coverage (Figure 3.6a and 3.6b) increases linearly with the ratio of metal NPs to AP-RW pollen particles, but eventually approaches a plateau at higher NP concentrations. The maximum AuNP surface coverage was ~55% and the maximum AgNC coverage was ~48%. The theoretical maximum surface coverage of spheres is as low as 78% surface

coverage for a 2-D square packing array and as high as 91% surface coverage from a 2-D hexagonal array [66]. The theoretical maximum surface coverage of cubes is as low as 50% for 2-D packing of cubes contacting only on their edges and as high as 100% for 2-D packing of cubes contacting at their faces. Close packing configurations may likely be hindered by a competition between normal attractive forces (oppositely charged metal NPs and AP-RW) and lateral repulsive forces (negatively charged NPs) [67, 68] .

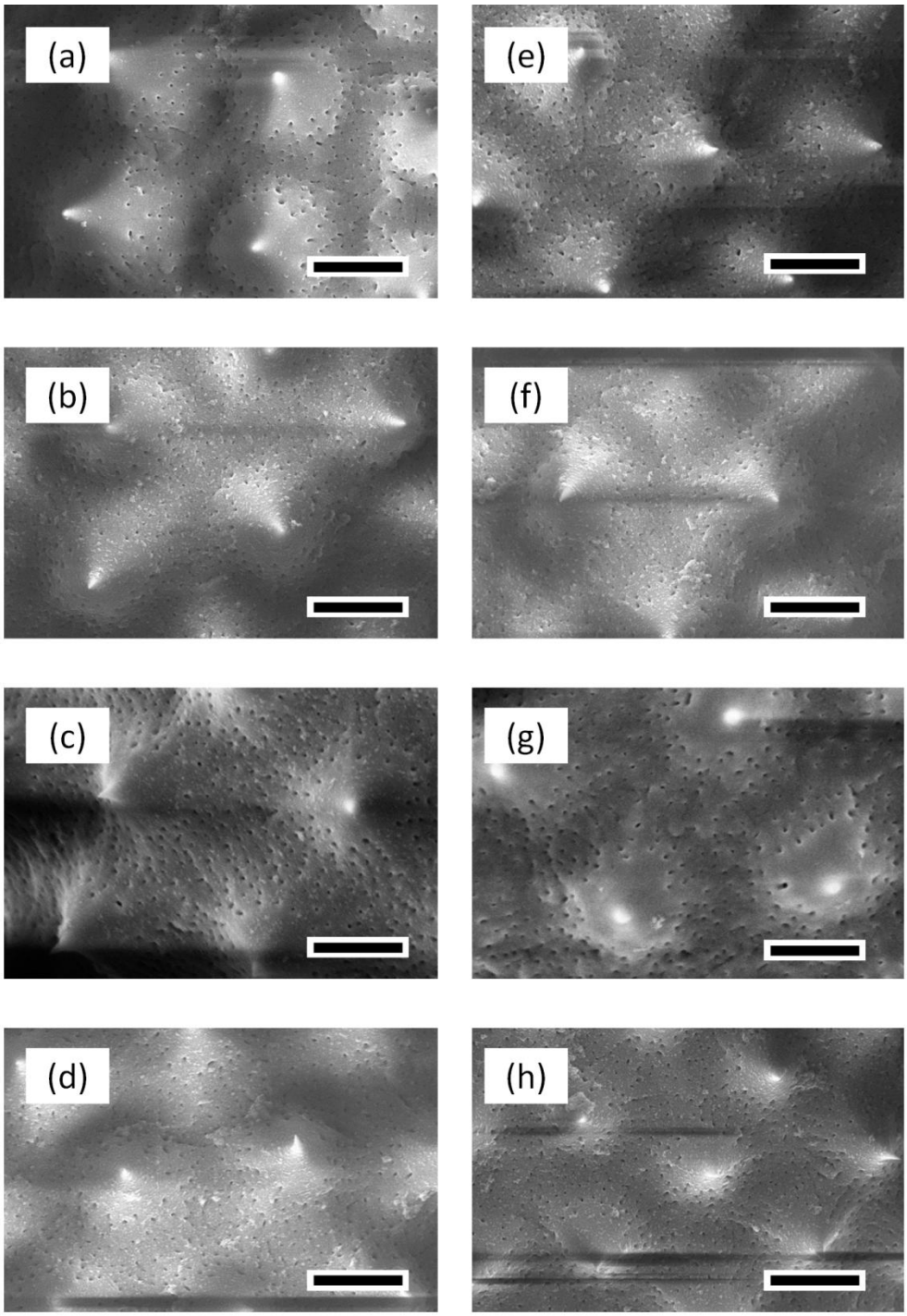

Figure 3.4. Scanning electron micrographs of BA-RW pollen mixed with metal NPs: a) n= the ratio of the number of AuNPs to pollen = $3.3x10^5$, b) n= $6.6x10^5$, c) n = $1.3x10^6$, d) n = $2.0x10^6$, e) m = the ratio of the number of AgNCs to pollen = $1.5x10^9$, f) m = $3.1x10^9$, g) m = $6.2x10^9$, and h) m = $9.3x10^9$. Scale bars represent 1 µm.

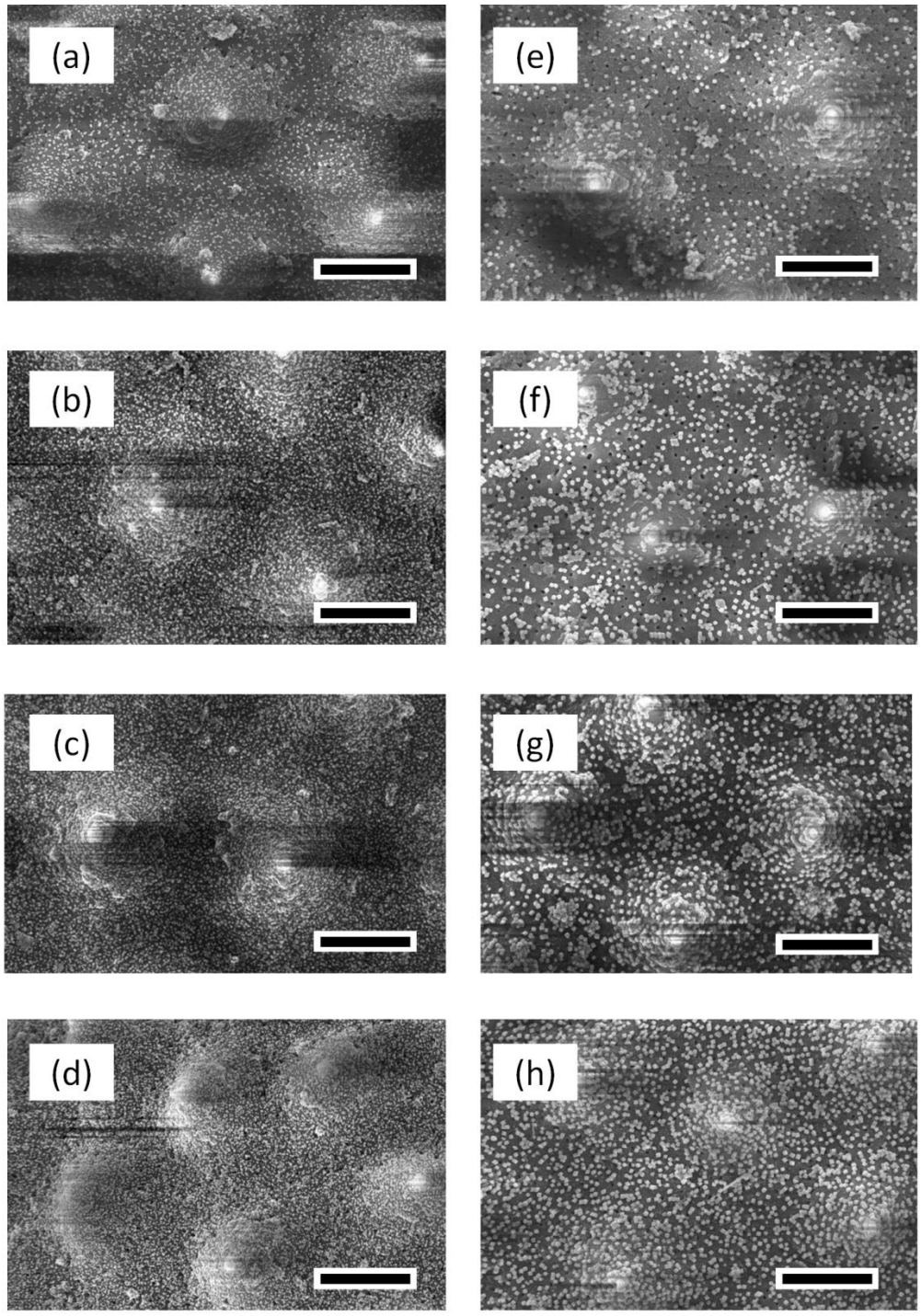

Figure 3.5. Scanning electron micrographs of AP-RW pollen mixed with metal NPs: a) n= the ratio of the number of AuNPs to pollen = 3.3x105 , b) n= $6.6x10^5$, c) n = $1.3x10^6$, d) n = $2.0x10^6$, e) m = the ratio of the number of AgNCs to pollen = $1.5x10^9$, f) m = $3.1x10^9$, g) m = $6.2x10^9$, and h) m = $9.3x10^9$. Scale bars represent 1 µm.

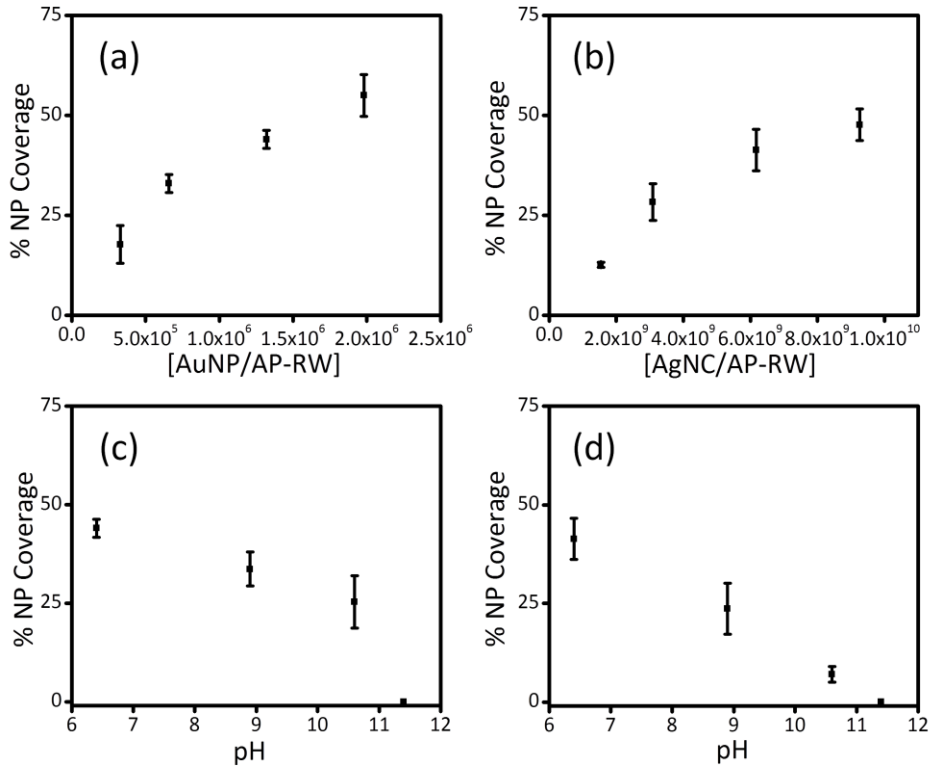

Figure 3.6. Change in % NP surface coverage on AP-RW pollen when: a) varying n (the ratio of AuNPs to AP-RW), b) varying m (the ratio of AgNCs to AP-RW), c) varying the pH of the individual components before mixing at n = $1.3x10^6$, and d) varying the pH of the individual components before mixing at m = $6.2x10^9$.

The zeta potential dependence on pH environment, positive at low pH values and negative at high pH values, for AP-RW pollen supports the presence of both carboxyl groups and amine groups on sporopollenin. The effect of pH environment on heteroaggregation was investigated by changing the pH conditions of the DIW-dispersed pollen particles and the DIW-dispersed metal NPs before mixing at a constant ratio (n = $3.3x10^5$ and m = $1.5x10^9$). Consistent with the zeta potential results, Figure 3.7 shows that no heteroaggregation occurs with negatively charged BA-RW pollen and the negatively charged metal NPs at any pH condition. Conversely, Figure 3.8 shows that the heteroaggregation of metal NPs onto AP-RW decreases with increasing pH and eventually ceases above pH 10.6. The metal NP surface coverage (Figure 3.6c and 3.6d) decreases linearly with increasing pH and disappears at pH 11.4. Although metal NPs

heteroaggreate onto AP-RW above the measured isoelectric point of AP-RW pollen, where there is a net negative zeta potential, amphoteric surfaces can still possess local regions of high positive charge [69]. The decrease in surface coverage with increasing pH can then be attributed to the decrease in local positive charges up until pH 11.4 where primary amines become deprotonated (estimated pKa range of 9.5-10.8).

The stability of AuNP-coated AP-RW (AuNP/AP-RW) and AgNC-coated AP-RW (AgNC/AP-RW) composite particles, prepared with a maximum surface coverage at pH 6.4, was investigated by increasing the solution pH post-heteroaggregation. Figure 3.9 demonstrates that increasing the solution pH to 11.4 decreases the surface coverage of AuNP/AP-RW composites from 55% to 44% and decreases the surface coverage of AgNC/AP-RW composites from 48% to 40%. These results suggest a strong anchoring of metal NPs to the AP-RW surface. The diameter of AP-RW pollen increases by as much as 12% in DIW compared to dried AP-RW pollen. As a result, the irreversible heterocoagulation is likely mediated by the entanglement of PVP chains, bound to the metal NPs, with the swollen sporopollenin matrix [18, 70].

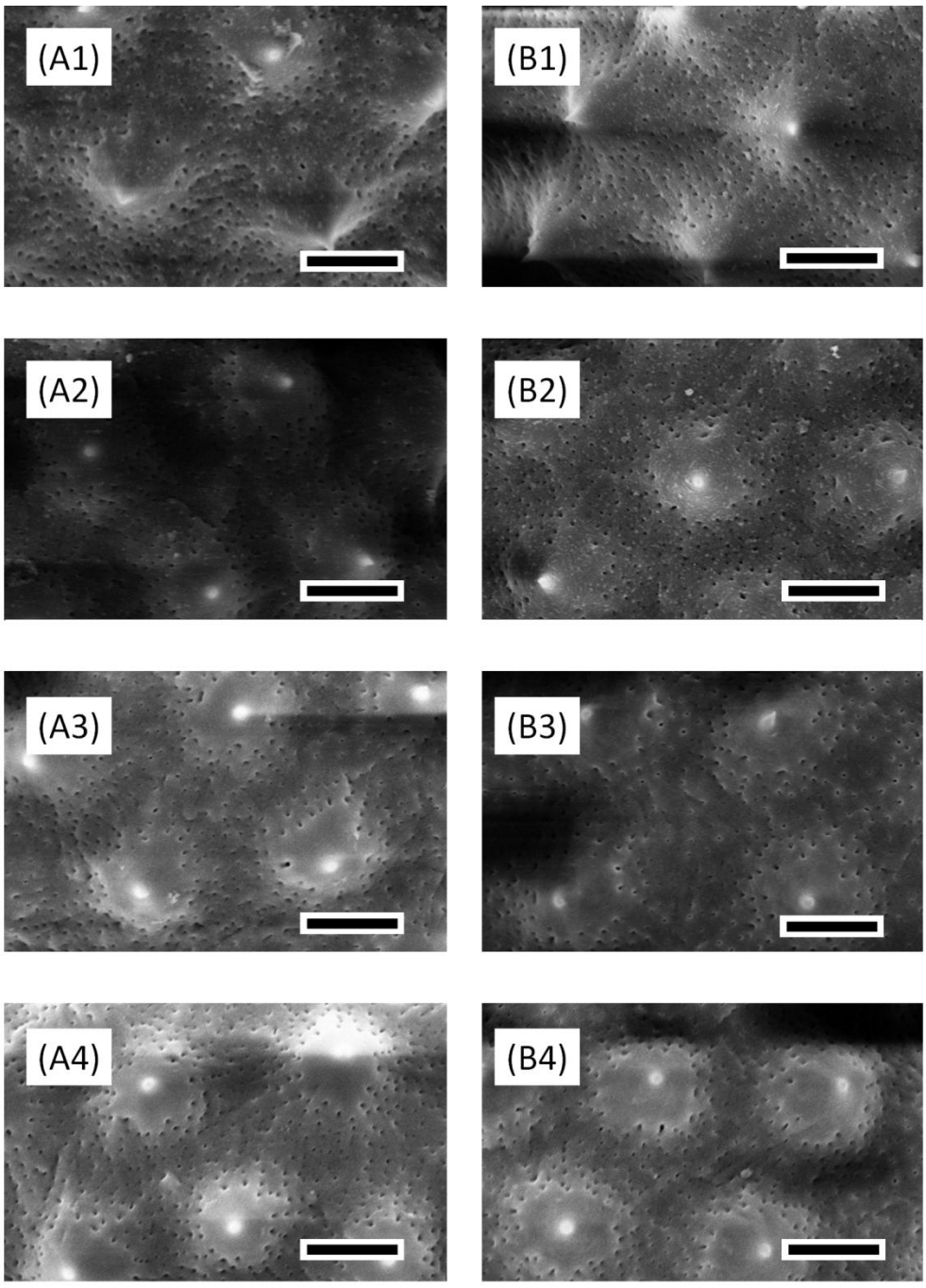

Figure 3.7. Scanning electron micrographs of BA-RW mixed with: A) AuNPs (n = the ratio of the number of AuNPs to pollen = $1.3x10^6$) and B) AgNCs (m = the ratio of the number of AgNCs to pollen = $6.2x10^9$). Label "1" indicates a mixture pH of 6.4, label "2" indicates a mixture pH of 8.9, label "3" indicates a mixture pH of 10.6, and label "4" indicates a mixture pH of 11.4. Scale bars represent 1 μm.

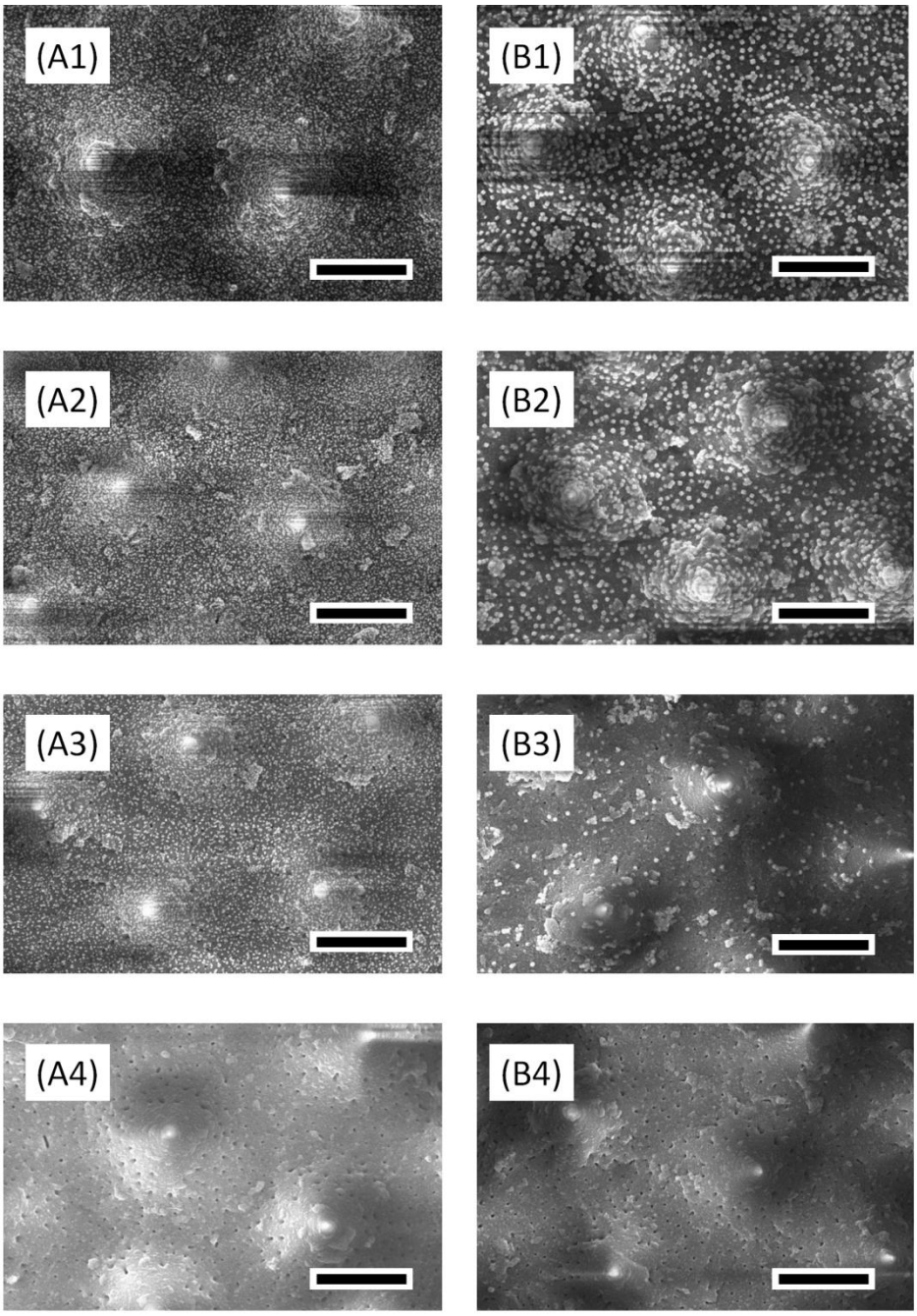

Figure 3.8. Scanning electron micrographs of AP-RW mixed with: A) AuNPs (n = the ratio of the number of AuNPs to pollen = $1.3x10^6$) and B) AgNCs (m = the ratio of the number of AgNCs to pollen = $6.2x10^9$). Label "1" indicates a mixture pH of 6.4, label "2" indicates a mixture pH of 8.9, label "3" indicates a mixture pH of 10.6, and label "4" indicates a mixture pH of 11.4. Scale bars represent 1 μm.

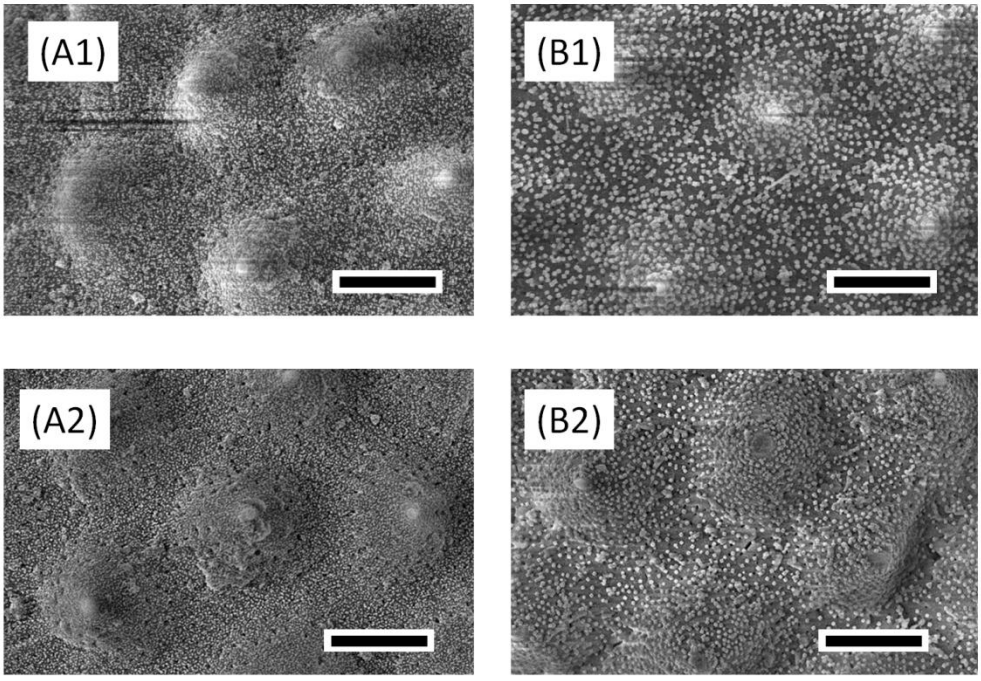

Figure 3.9. Scanning electron micrographs of AP-RW mixed with: A) AuNPs (n = the ratio of the number of AuNPs to pollen = $2.0x10^6$) and B) AgNCs (m = the ratio of the number of AgNCs to pollen = $9.3x10^9$). Label "1" indicates a mixture pH of 6.4 and label "2" indicates the composites suspension pH 6.4 was increased to pH 11.4. Scale bars represent 1 µm.

3.4.3 Nanoparticle-Pollen Composite Adhesion

The adhesion strength of the pollen particles prepared in this study (BA-RW, AP-RW, AuNP/AP-RW (n = $2.0x10^6$), and AgNC/AP-RW (m = $9.3x10^9$) pollen grains) are examined using AFM. The adhesion results are compared to cleaned ragweed pollen adhesion from Chapter 2. Polyvinyl alcohol (PVA), polyvinyl acetate (PVAc), polystyrene (PS), piranha-etched silicon (Si), and gold-coated silicon (Au-Si) substrates were used to examine the effect of surface chemistry on the adhesion forces. The measured average surface roughnesses of the polymer and silicon surfaces, from Chapter 2, fall within a range of 0.2-2.2 nm. SEM images of cantilevers with pollen grains attached are shown in Figure 3.10, taken after all force measurements were completed.

Figure 3.11a-c show typical force-distance curve for AP-RW pollen, AuNP/AP-RW, and AgNC/AP-RW pollen, respectively, on the Au-Si surface, which are typical for other substrates investigated herein. In should be noted that force-distance curves for cleaned ragweed and BA-RW pollen showed the same behavior as AP-RW force-distance curves. All pollens investigated did not show evidence of long-ranged jump to contact forces, but rather short-ranged (a few nanometers) attractions of tens of nanonewtons. During the approach and retraction of all pollens, a sudden pull-off event occurs in which the two solids separate suddenly at the maximum adhesion force. This is clearly indicative of a solid-solid short-ranged adhesion. However, in the case of AuNP/AP-RW pollens, initial contact with flat surfaces produced multiple contacts (Figure 3.11b). Figure 3.10D2 clearly shows that AuNPs have coated the tips of all AP-RW pollen spikes, whereas Figure 3.10E2 shows that AgNCs do not coat any AP-RW spike tips resulting in one contact event in Figure 3.11c. The appearance of multiple contact points in the force-distance curves of AuNP/AP-RW pollen suggests that multiple AuNPs are contacting the substrates.

The average adhesion forces of cleaned ragweed, BA-RW, AP-RW, AuNP/AP-RW, and AgNC/AP-RW pollen particles with PVA, PVAc, PS, Si, and Au-Si substrates are shown in Figure 3.12. As seen in Chapter 2, no substantial adhesion dependence on substrate chemistry was observed. The average adhesion forces of cleaned, BA-RW, AP-RW, AuNP/AP-RW, and AgNC/AP-RW pollen are tabulated in Table 3.2. Interestingly, AuNP/AP-RW particles exhibited enhanced adhesion (~45 nN) compared to AgNC/AP-RW particles (~27 nN), which aligned with the adhesion forces of cleaned ragweed, BA-RW, and uncoated AP-RW particles (~22-26 nN).

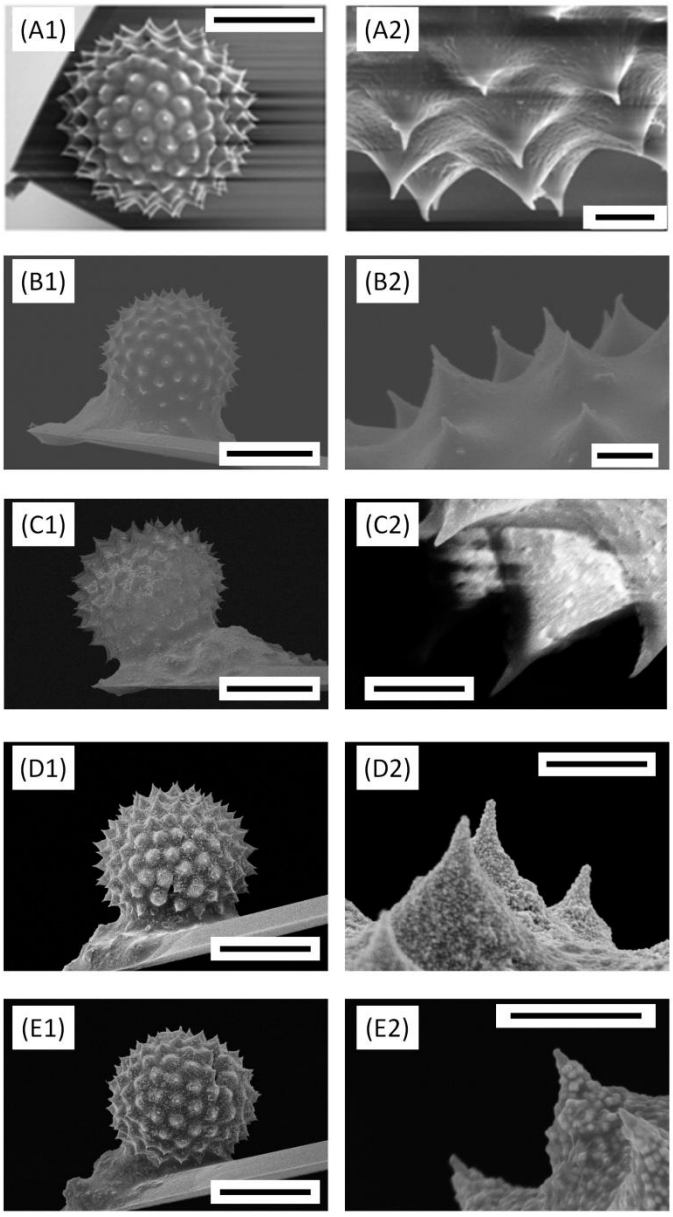

Figure 3.10. Scanning electron micrographs of single-particle-bearing cantilever probes of A) cleaned ragweed pollen, B) BA-RW pollen, C) APTES-RW, D) AuNP/AP-RW (n= the ratio of the number of AuNPs to pollen = 2.0×10^6), and E) AgNC/AP-RW pollen (m = the ratio of the number of AgNCs to pollen = 9.3×10^9). Label "1" indicates low magnification image and "2" indicates high magnification images for each pollen type. Low magnification scale bar represents 10 µm and high magnification scale bars represent 1 µm.

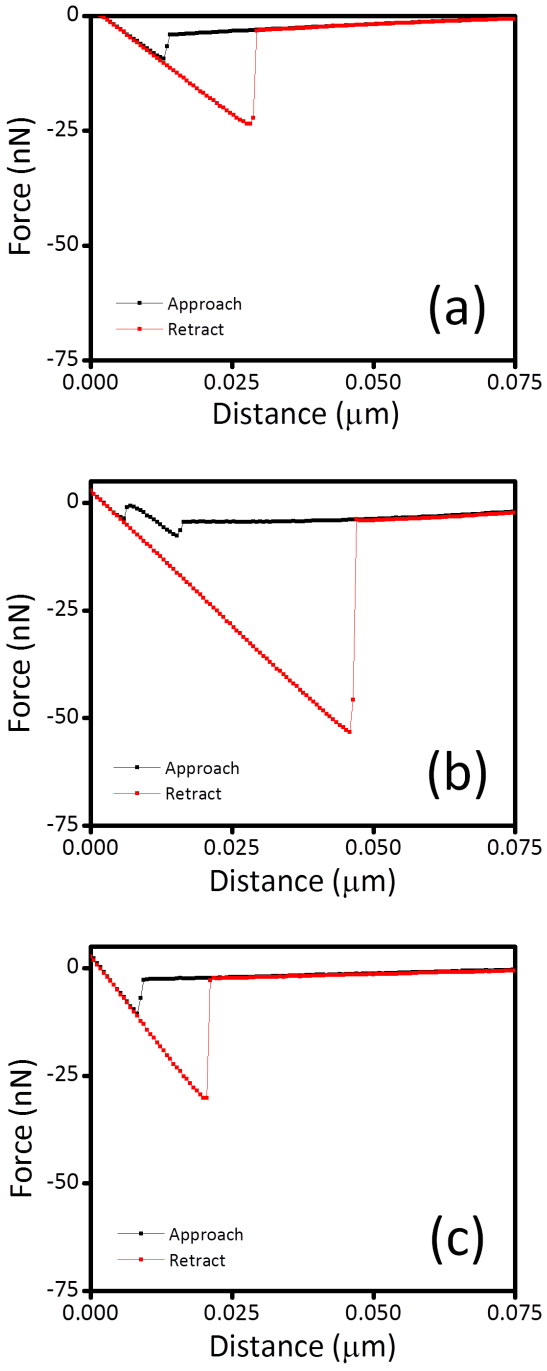

Figure 3.11. Representative force-distance curve between an Au-Si substrate and: a) AP-RW pollen, b) AuNP/AP-RW pollen, and c) AgNC/AP-RW pollen substrate.

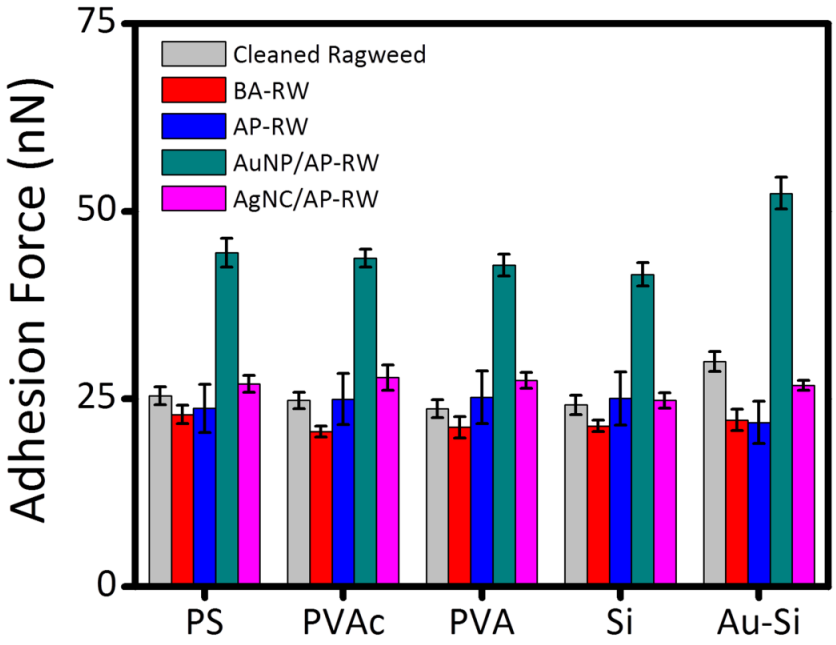

Figure 3.12. Adhesion forces between cleaned ragweed, BA-RW, AP-RW, AuNP/AP-RW, and AgNC/AP-RW pollen AFM probes and select substrates. Error bars are 95% confidence intervals.

Table 3.2. Average measured values of adhesion, measured spike tip radius, and calculated contact radius. Error indicates 95% confidence interval.

	Adhesion Force (nN)	Measured Tip Radius (nm)	Calculated Tip Radius (nm)
Cleaned Ragweed	26 ± 2	52 ± 5	--
BA-RW	22 ± 1	45 ± 4	44 ± 3
AP-RW	24 ± 1	47 ± 6	50 ± 6
AuNP/AP-RW	45 ± 4	47 ± 6[a]	46 ± 7[b]
AgNC/AP-RW	27 ± 1	47 ± 6[a]	55 ± 5

Note. [a] Measured tip radius of AP-RW pollen is used. [b] Calculated contact radius assuming gold-substrate interactions.

Analyses of the VDW-based adhesion forces were conducted using the Hamaker model in Eq. (3.2):

$$F_{vdw} = \frac{A_{132}R}{6d^2} \tag{3.2}$$

where A_{132} is the non-retarded Hamaker constant of material 1 and 2 interacting across medium 3 (air), R is the contact radius, and D is the cutoff separation distance for the VDW interaction (≈ 0.165 nm) [69]. Using cleaned ragweed pollen as a model (from Chapter 2), A_{132} values for PS-, PVAc-, PVA-, Si-, and Au-Si-ragweed pollen interactions were calculated by inserting the cleaned ragweed adhesion force and spine tip radius into Eq. (3.2) to calculate the appropriate A_{132}. A_{132} values for PS- and Au-Au interactions were obtained from literature [71, 72]. Approximate A_{132} values for PVAc-, PVA, and Si-Au interactions were obtained using a combining relation via Eq. (3.3):

$$A_{132} \approx \left(\sqrt{A_{11} - A_{33}}\right)\left(\sqrt{A_{22} - A_{33}}\right) \tag{3.3}$$

where available A_{11} is the Hamaker constant of Au (available in the literature), A_{22} is the Hamaker constant of the substrate (available in the literature), and A_{33} is the Hamaker constant of the medium (A_{33} = 0 for air) [69, 73-75]. Although estimating the Hamaker constant of interactions involving a metallic medium using Eq. (3.3) may be an oversimplification, we deem it to be suitable as a first-order analysis. The average calculated contact radii of BA-RW, AP-RW, AuNP/AP-RW, and AgNC/AP-RW particles are shown in Table 3.2. For BA-RW, AP-RW, AgNC/AP-RW, the calculated contact radii were consistent with the contact of a single spine tip to a given substrate. Together with SEM images and force-distance curves, the calculated contact radius of AuNP/AP-RW was consistent with the contact of multiple AuNPs (~15 nm radius). The size of the metal NPs (AuNPs ~15 nm radius, AgNCs ~30 nm radius) relative to the size of AP-RW spine tips (~47 nm radius) may be one possible reason why AP-RW spine tips were successfully coated by AuNPs but unsuccessfully coated by AgNCs. With

comparable sizes, the curvature of the AP-RW spines may have had a more significant impact on AgNCs' inability to attach to the tips.

3.4.4 Nanoparticle-Pollen Composite Effectiveness as SERS Substrates

The effectiveness of metal NP-AP-RW pollen particles as SERS substrates is evaluated by measuring their Raman scattering relative to uncoated AP-RW and neat metal NPs. Figure 3.13 shows the SERS enhancement caused by NP-coated AP-RW particles. No detectable Raman bands are present for uncoated AP-RW pollen and, besides a strong Si band at 517 cm^{-1} from the underlying Si substrate, no appreciable Raman bands are present for neat metal NPs [76]. As the degree of metal surface coverage increases to maximum coverage, Raman bands appear for AuNP/AP-RW particles. Conversely, Raman bands appear at the lowest metal coverage for AgNCs and remain fairly consistent as the metal coverage increases. A large Raman band corresponding to Si-C stretching vibrations from APTES and the sporopollenin shell appear at 781 cm^{-1} in AgNC/AP-RW particles, while a less distinct Raman band appears at the same location in AuNP/AP-RW particles [10, 43]. Raman bands at 671 cm^{-1} and 659 cm^{-1} from AuNP/AP-RW and AgNC/AP-RW, respectively, correspond to N=C=O ring deformation from the PVP ring. Additionally, AuNP/AP-RW displayed enhanced Raman bands at 956, 1258, and 1335 cm^{-1} that are characteristic of the sporopollenin matrix and Raman bands at 759, 881, 1377, and 1466 cm^{-1} that correspond to the PVP capping agent [77]. Interestingly, the enhanced Raman bands of the AuNP/AP-RW and AgNC/AP-RW composites are not equivalent. Although it might be expected that the Raman enhancement of the two composites would be similar, there may be a number of factors contributing to this inconsistency. The enhancement of Raman bands in AuNP/AP-RW composites compared to AgNC/AP-RW composites might be caused by the degree of metal NP coverage (~55% for AuNP/AP-RW and ~48% for AgNCs), however it is more likely that the discrepancy is a factor of the composite optical

properties. Because surface plasmons are excited by an incident laser source, the excitation wavelength must be adapted to the resonance wavelength of the metal surface [78]. One way to tune the optical properties to fit the excitation source is by tuning the shape and size of the metal NPs of a SERS substrate (i.e., high-aspect ratio, anisotropic structures) [79, 80]. Although the metal NP-pollen composites are not optimized for use as SERS substrates, the fact that the composites can enhance Raman bands consistent with the PVP capping agent and the sporopollenin chemistry are promising. Selecting appropriate NP particles with more favorable sizes and chemistries that are conducive for Raman applications could make metal NP-pollen composites potentially useful SERS substrates.

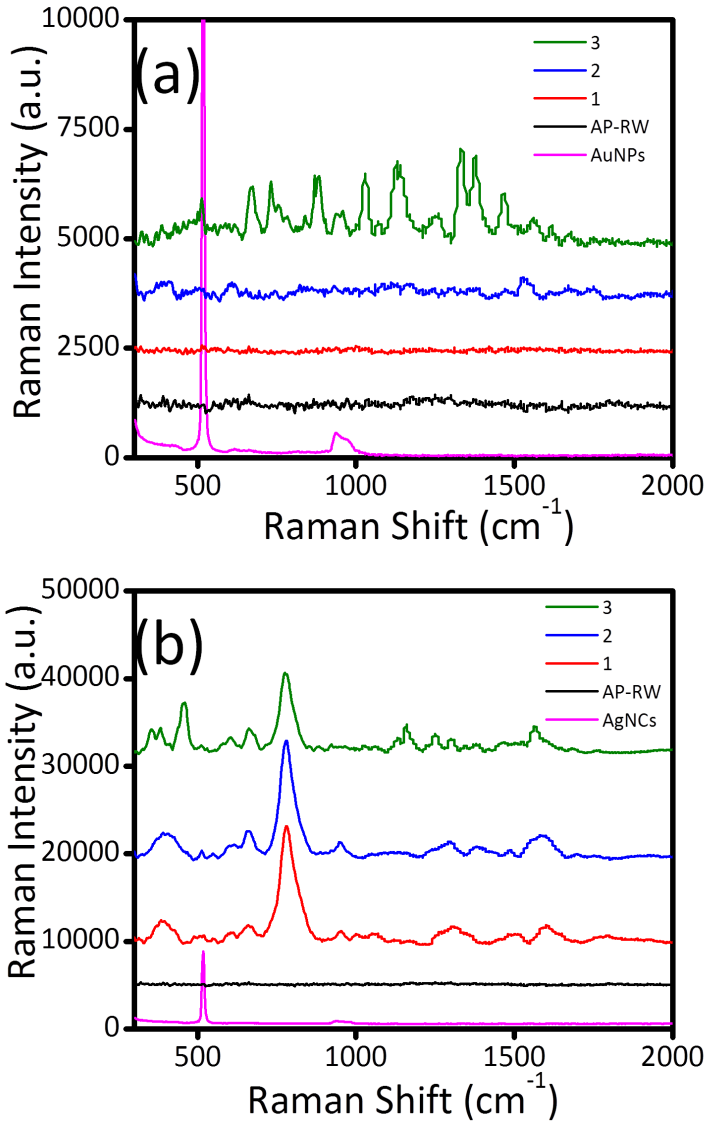

Figure 3.13. Surface enhanced Raman spectra of a) AuNP/AP-RW composite particles with different levels of metal coverage: 1) n = $3.3x10^5$, 2) n= $6.6x10^5$, and 3) n = $2.0x10^6$ and b) AgNC/AP-RW composite particles with different levels of metal coverage: 1) m = $1.5x10^9$, 2) m = $3.1x10^9$, and 3) m = $9.3x10^9$ relative to neat AP-RW particles and neat metal NPs.

3.5 Conclusions

This chapter demonstrates the first ex-situ preparation of metal NP-pollen composites displaying enhanced nanoparticle-mediated adhesion. The hydroxyl-enriched

surface of sporopollenin supported functionalization with an aminosilane, which imparted a positive surface charge in neutral pH conditions. Electrostatic-driven heteroaggregation between positively charged pollen particles and negatively charged AuNPs and AgNCs enabled surface coverage up to 55%. The bio-organic ragweed (*Ambrosia artemisiifolia*) pollen core possessed well-defined spine protuberances. Cleaned, base/acid-treated, amine-functionalized, and AgNC composite ragweed pollen exhibited short-range VDW-based adhesion dependent on the contact with a single spine tip. NP-covered tips of AuNP-ragweed pollen particles displayed enhanced adhesion (nearly double) compared to uncoated pollen spines. Multiple nanoparticle contacts as well as an increased Hamaker constant facilitated the increase in short-range VDW adhesion. Additionally, NP-pollen composites showed potential for use as SERS substrates capable of enhancing the Raman signal of molecules bound to the NP surface. The approach developed in this chapter provides a framework for utilizing bio-organic pollen-NP composite particles for enhanced adhesion and as SERS substrates, in addition to a myriad of applications, by tailoring the pollen morphology, NP size, and NP chemistry.

Acknowledgement: We are grateful to Dr. Behrens for his generous support in providing access to his equipment for measuring zeta potentials (Zetasizer and SurPASS elctrokinetic analyzer). We are grateful to Dr. Mahmoud A. Mahmoud for synthesizing and providing the gold and silver nanoparticles for this study.

3.6 References

1. Wang, S., G. Guillen, and E.M. Hoek, *Direct observation of microbial adhesion to membranes.* Environmental science & technology, 2005. **39**(17): p. 6461-6469.

2. Adi, S., et al., *Micro-particle corrugation, adhesion and inhalation aerosol efficiency.* European Journal of Pharmaceutical Sciences, 2008. **35**(1–2): p. 12-18.

3. Henry, C., J.-P. Minier, and G. Lefèvre, *Numerical Study on the Adhesion and Reentrainment of Nondeformable Particles on Surfaces: The Role of Surface Roughness and Electrostatic Forces.* Langmuir, 2011. **28**(1): p. 438-452.

4. Balachandran, D.K., et al., *Adhesion of dry nano-coated microparticles to stainless steel: A physical interpretation.* Powder Technology, 2012. **226**(0): p. 1-9.

5. Quintanilla, M.A.S., et al., *From Single Particle Interactions to Bulk Powder Flow: Application to Uranium Oxide Powders.* Particle & Particle Systems Characterization, 2006. **23**(2): p. 121-126.

6. Wen, Y., et al., *Biodegradable nanocomposite microparticles as drug delivering injectable cell scaffolds.* Journal of Controlled Release, 2011. **156**(1): p. 11-20.

7. Hamad, S.A., et al., *Encapsulation of living cells into sporopollenin microcapsules.* Journal of Materials Chemistry, 2011. **21**(44): p. 18018-18023.

8. Binks, B.P., et al., *Sporopollenin capsules at fluid interfaces: particle-stabilised emulsions and liquid marbles.* Soft Matter, 2011. **7**(8): p. 4017-4024.

9. Lee, J.H., et al., *Pollen: A Novel, Biorenewable Filler for Polymer Composites.* Macromolecular Materials and Engineering, 2011. **296**(11): p. 1055-1062.

10. Joseph, V., et al., *Surface-enhanced Raman scattering with silver nanostructures generated in situ in a sporopollenin biopolymer matrix.* Chem. Commun., 2011. **47**(11): p. 3236-3238.

11. Thio, B.J.R., K.K. Clark, and A.A. Keller, *Magnetic pollen grains as sorbents for facile removal of organic pollutants in aqueous media.* Journal of hazardous materials, 2011. **194**: p. 53-61.

12. Xia, Y., et al., *Biotemplated fabrication of hierarchically porous NiO/C composite from lotus pollen grains for lithium-ion batteries.* Journal of Materials Chemistry, 2012. **22**(18): p. 9209-9215.

13. Song, F., et al., *Bioinspired Hierarchical Tin Oxide Scaffolds for Enhanced Gas Sensing Properties.* The Journal of Physical Chemistry C, 2012. **116**(18): p. 10274-10281.

14. Zhang, X., et al., *Adhesion and friction studies of nano-textured surfaces produced by self-assembling Au nanoparticles on silicon wafers.* Tribology Letters, 2012. **46**(1): p. 65-73.

15. Zhang, X., et al., *Adhesion and friction studies of microsphere-patterned surfaces in contact with atomic force microscopy colloidal probe.* Colloids and Surfaces A: Physicochemical and Engineering Aspects, 2012. **401**(0): p. 90-96.

16. Jacobs, T.D., et al., *The Effect of Atomic-Scale Roughness on the Adhesion of Nanoscale Asperities: A Combined Simulation and Experimental Investigation.* Tribology Letters, 2013: p. 1-13.

17. Tamai, T., et al. *Metal Nanoparticle/Polymer Hybrid Particles: The Catalytic Activity of Metal Nanoparticles Formed on the Surface of Polymer Particles by UV-Irradiation*. in *Macromolecular Symposia*. 2009. Wiley Online Library.

18. Lee, J.-H., et al., *Highly Scattering, Surface-Enhanced Raman Scattering-Active, Metal Nanoparticle-Coated Polymers Prepared via Combined Swelling−Heteroaggregation.* Chemistry of Materials, 2009. **21**(23): p. 5654-5663.

19. Urbina, M.C., et al., *Investigation of Magnetic Nanoparticle−Polymer Composites for Multiple-controlled Drug Delivery.* The Journal of Physical Chemistry C, 2008. **112**(30): p. 11102-11108.

20. Quach, A.D., et al., *Gold Nanoparticle− Quantum Dot− Polystyrene Microspheres as Fluorescence Resonance Energy Transfer Probes for Bioassays.* Journal of the American Chemical Society, 2011. **133**(7): p. 2028-2030.

21. Liu, J., et al., *Synthesis, characterization, and application of composite alginate microspheres with magnetic and fluorescent functionalities.* Journal of Applied Polymer Science, 2009. **113**(6): p. 4042-4051.

22. Bhattacharya, R. and P. Mukherjee, *Biological properties of "naked" metal nanoparticles.* Advanced Drug Delivery Reviews, 2008. **60**(11): p. 1289-1306.

23. Kelly, K.L., et al., *The Optical Properties of Metal Nanoparticles: The Influence of Size, Shape, and Dielectric Environment.* The Journal of Physical Chemistry B, 2002. **107**(3): p. 668-677.

24. Henry, C.R., *Surface studies of supported model catalysts.* Surface science reports, 1998. **31**(7–8): p. 231-325.

25. Teja, A.S. and P.-Y. Koh, *Synthesis, properties, and applications of magnetic iron oxide nanoparticles.* Progress in Crystal Growth and Characterization of Materials, 2009. **55**(1–2): p. 22-45.

26. Kneipp, K., et al., *Single molecule detection using surface-enhanced Raman scattering (SERS).* Physical review letters, 1997. **78**(9): p. 1667.

27. Xu, H., et al., *Electromagnetic contributions to single-molecule sensitivity in surface-enhanced Raman scattering.* Physical Review E, 2000. **62**(3): p. 4318.

28. Hutter, E. and J.H. Fendler, *Exploitation of localized surface plasmon resonance.* Advanced Materials, 2004. **16**(19): p. 1685-1706.

29. Otto, A., et al., *Surface-enhanced Raman scattering.* Journal of Physics: Condensed Matter, 1992. **4**(5): p. 1143.

30. Lu, Y., G.L. Liu, and L.P. Lee, *High-density silver nanoparticle film with temperature-controllable interparticle spacing for a tunable surface enhanced Raman scattering substrate.* Nano letters, 2005. **5**(1): p. 5-9.

31. Li, J.-M., et al., *Poly (styrene-co-acrylic acid) core and silver nanoparticle/silica shell composite microspheres as high performance surface-enhanced Raman spectroscopy (SERS) substrate and molecular barcode label.* Journal of Materials Chemistry, 2011. **21**(16): p. 5992-5998.

32. Cintra, S., et al., *Sculpted substrates for SERS.* Faraday Discussions, 2006. **132**(0): p. 191-199.

33. Kim, K., et al., *Easy deposition of Ag onto polystyrene beads for developing surface-enhanced-Raman-scattering-based molecular sensors.* Journal of Colloid and Interface Science, 2008. **318**(2): p. 195-201.

34. Jans, H. and Q. Huo, *Gold nanoparticle-enabled biological and chemical detection and analysis.* Chemical Society Reviews, 2012. **41**(7): p. 2849-2866.

35. Afonso, M.D., G. Hagmeyer, and R. Gimbel, *Streaming potential measurements to assess the variation of nanofiltration membranes surface charge with the concentration of salt solutions.* Separation and Purification Technology, 2001. **22**: p. 529-541.

36. Elimelech, M., W.H. Chen, and J.J. Waypa, *Measuring the zeta (electrokinetic) potential of reverse osmosis membranes by a streaming potential analyzer.* Desalination, 1994. **95**(3): p. 269-286.

37. Xie, H., T. Saito, and M.A. Hickner, *Zeta Potential of Ion-Conductive Membranes by Streaming Current Measurements.* Langmuir, 2011. **27**(8): p. 4721-4727.

38. Buksek, H., *Zeta potential determination of polymeric materials using two differently designed measuring cells of an electrokinetic analyzer.* Acta Chim. Slov, 2010. **57**: p. 700-706.

39. Domínguez, E., et al., *Pollen sporopollenin: degradation and structural elucidation.* Sexual Plant Reproduction, 1999. **12**(3): p. 171-178.

40. Piffanelli, P., J.H.E. Ross, and D.J. Murphy, *Biogenesis and function of the lipidic structures of pollen grains.* Sexual Plant Reproduction, 1998. **11**(2): p. 65-80.

41. Zetzsche, F. and K. Huggler, *Untersuchungen über die Membran der Sporen und Pollen. I. 1. Lycopodium clavatum L.* Justus Liebigs Annalen der Chemie, 1928. **461**(1): p. 89-109.

42. Guilford, W.J., et al., *High Resolution Solid State 13C NMR Spectroscopy of Sporopollenins from Different Plant Taxa.* Plant Physiology, 1988. **86**(1): p. 134-136.

43. Socrates, G., *Infrared and Raman characteristic group frequencies : tables and charts*. 3rd ed2001, Chichester ; New York: Wiley. xv, 347 p.

44. Fang, K., et al., *Isolation of de-exined pollen and cytological studies of the pollen intines of Pinus bungeana Zucc. Ex Endl. and Picea wilsonii Mast.* Flora-Morphology, Distribution, Functional Ecology of Plants, 2008. **203**(4): p. 332-340.

45. Yang, H., et al., *Characteristics of hemicellulose, cellulose and lignin pyrolysis.* Fuel, 2007. **86**(12): p. 1781-1788.

46. Pandey, K. and A. Pitman, *FTIR studies of the changes in wood chemistry following decay by brown-rot and white-rot fungi.* International biodeterioration & biodegradation, 2003. **52**(3): p. 151-160.

47. Yilmaz, E., et al., *Immobilization of Candida rugosa lipase on glass beads for enantioselective hydrolysis of racemic Naproxen methyl ester.* Bioresource technology, 2011. **102**(2): p. 499-506.

48. Wang, Y.-P., et al., *Preparation and characterization of poly (N-isopropylacrylamide) films on a modified glass surface via surface initiated redox polymerization.* Materials Letters, 2005. **59**(14): p. 1736-1740.

49. Arslan, G., et al., *Surface modification of glass beads with an aminosilane monolayer.* Turkish Journal of Chemistry, 2006. **30**(2): p. 203-210.

50. Yamaura, M., et al., *Preparation and characterization of (3-aminopropyl) triethoxysilane-coated magnetite nanoparticles.* Journal of magnetism and magnetic materials, 2004. **279**(2): p. 210-217.

51. Gwon, J.G., et al., *Characterization of chemically modified wood fibers using FTIR spectroscopy for biocomposites.* Journal of Applied Polymer Science, 2010. **116**(6): p. 3212-3219.

52. Narayanan, R. and M.A. El-Sayed, *Catalysis with Transition Metal Nanoparticles in Colloidal Solution: Nanoparticle Shape Dependence and Stability.* The Journal of Physical Chemistry B, 2005. **109**(26): p. 12663-12676.

53. Tao, A.R., S. Habas, and P. Yang, *Shape control of colloidal metal nanocrystals.* small, 2008. **4**(3): p. 310-325.

54. Narayanan, R. and M.A. El-Sayed, *Shape-Dependent Catalytic Activity of Platinum Nanoparticles in Colloidal Solution.* Nano letters, 2004. **4**(7): p. 1343-1348.

55. Behera, M. and S. Ram, *Synthesis and characterization of core–shell gold nanoparticles with poly (vinyl pyrrolidone) from a new precursor salt.* Applied Nanoscience, 2013. **3**(1): p. 83-87.

56. Behera, M. and S. Ram, *Spectroscopy-based study on the interaction between gold nanoparticle and poly (vinylpyrrolidone) molecules in a non-hydrocolloid.* International Nano Letters, 2013. **3**(1): p. 1-7.

57. Behera, M. and S. Ram, *Inquiring the mechanism of formation, encapsulation, and stabilization of gold nanoparticles by poly (vinyl pyrrolidone) molecules in 1-butanol.* Applied Nanoscience, 2013: p. 1-8.

58. Barrier, S., et al., *Access to a primary aminosporopollenin solid support from plant spores.* Green Chemistry, 2010. **12**(2): p. 234-240.

59. Zhang, J., T. Kleinöder, and J. Gasteiger, *Prediction of pKa Values for Aliphatic Carboxylic Acids and Alcohols with Empirical Atomic Charge Descriptors†.* Journal of Chemical Information and Modeling, 2006. **46**(6): p. 2256-2266.

60. Vansant, E.F., P. Van Der Voort, and K.C. Vrancken, *Characterization and chemical modification of the silica surface*1995: Access Online via Elsevier.

61. Kurayama, F., et al., *Facile method for preparing organic/inorganic hybrid capsules using amino-functional silane coupling agent in aqueous media.* Journal of Colloid and Interface Science, 2010. **349**(1): p. 70-76.

62. Kim, Y.J., N. Korkmaz, and C.H. Nam, *Phage assembly using APTES-conjugation of major coat p8 protein for possible scaffolds.* 2012.

63. Coche-Guérente, L., V. Desprez, and P. Labbé, *Characterization of organosilasesquioxane-intercalated-laponite-clay modified electrodes and (bio) electrochemical applications.* Journal of Electroanalytical Chemistry, 1998. **458**(1): p. 73-86.

64. Christoforou, C.C., G.B. Westermann-Clark, and J.L. Anderson, *The streaming potential and inadequacies of the Helmholtz equation.* Journal of Colloid and Interface Science, 1985. **106**(1): p. 1-11.

65. Cohen, R.R. and C.J. Radke, *Streaming potentials of nonuniformly charged surfaces.* Journal of Colloid and Interface Science, 1991. **141**(2): p. 338-347.

66. Brass, P., W.O.J. Moser, and J.n. Pach, *Research problems in discrete geometry*2005, New York: Springer. xii, 499 p.

67. Luckham, P., B. Vincent, and T.F. Tadros, *The controlled flocculation of particulate dispersions using small particles of opposite charge. IV. Effect of surface coverage of adsorbed polymer on heteroflocculation.* Colloids and Surfaces, 1983. **6**(2): p. 119-133.

68. Harley, S., D.W. Thompson, and B. Vincent, *The adsorption of small particles onto larger particles of opposite charge Direct electron microscope studies*. Colloids and Surfaces, 1992. **62**(1): p. 163-176.

69. Israelachvili, J., *Intermolecular and Surface Forces*. 2nd ed: Academic Press: London, 1992.

70. Chen, C.-W., T. Serizawa, and M. Akashi, *Preparation of Platinum Colloids on Polystyrene Nanospheres and Their Catalytic Properties in Hydrogenation†.* Chemistry of Materials, 1999. **11**(5): p. 1381-1389.

71. Kim, T., et al., *Control of Gold Nanoparticle Aggregates by Manipulation of Interparticle Interaction.* Langmuir, 2005. **21**(21): p. 9524-9528.

72. Weber, R., et al., *Embedding of gold nanoclusters on polystyrene surfaces: influence of the surface modification on the glass transition.* Macromolecules, 2003. **36**(24): p. 9100-9106.

73. Dunn, A. and L.H. Chong, *Application of the theory of colloid stability to the problem of particle formation in aqueous solutions of vinyl acetate.* British Polymer Journal, 1970. **2**(1): p. 49-59.

74. Visser, J., *On Hamaker constants: A comparison between Hamaker constants and Lifshitz-van der Waals constants.* Advances in Colloid and Interface Science, 1972. **3**(4): p. 331-363.

75. Huang, Y., et al., *Mechanisms for nano particle removal in brush scrubber cleaning.* Applied Surface Science, 2011. **257**(7): p. 3055-3062.

76. Li, B., D. Yu, and S.-L. Zhang, *Raman spectral study of silicon nanowires.* Physical Review B, 1999. **59**(3): p. 1645.

77. Borodko, Y., et al., *Probing the interaction of poly (vinylpyrrolidone) with platinum nanocrystals by UV-Raman and FTIR.* The Journal of Physical Chemistry B, 2006. **110**(46): p. 23052-23059.

78. Hering, K., et al., *SERS: a versatile tool in chemical and biochemical diagnostics.* Analytical and Bioanalytical Chemistry, 2008. **390**(1): p. 113-124.

79. Wiley, B.J., et al., *Maneuvering the surface plasmon resonance of silver nanostructures through shape-controlled synthesis.* The Journal of Physical Chemistry B, 2006. **110**(32): p. 15666-15675.

80. Orendorff, C.J., et al., *Aspect ratio dependence on surface enhanced Raman scattering using silver and gold nanorod substrates.* Physical Chemistry Chemical Physics, 2006. **8**(1): p. 165-170.

CHAPTER 4

CONVERSION OF POLLEN PARTICLES INTO THREE-DIMENSIONAL CERAMIC REPLICAS TAILORED FOR MULTIMODAL ADHESION

This chapter was published in part in *Chem. Mater.*, in press, (2013) and is reproduced here with permission.

4.1 Overview

In this chapter, we report the first syntheses of three-dimensional (3-D) nanocrystalline, all-oxide replicas of pollen microparticles tailored for multimodal (bio-enabled and synthetic) adhesion via use of a scalable, highly-conformal, layer-by-layer (LbL) surface sol-gel (SSG) coating process. High fidelity replication allowed the pollen-shaped oxide microparticles to be utilized for adhesion via tailorable short-range (~10 nm) van der Waals (VDW) attraction, with the magnitude of such VDW-based adhesion influenced by the nanoscale topography of surface features retained by the replicas. Conversion of the pollen into ferrimagnetic (Fe_3O_4) microparticle replicas allowed for the use of magnetic attraction at short and long ranges (up to ~1 mm). By selecting pollen particles with particular surface features, and by LbL SSG-enabled conversion of such pollen into 3-D nanocrystalline replicas comprised of an appropriate type and amount of magnetic oxide, adhesive microparticles utilizing tunable short- and long-range attractive forces can be generated.

4.2 Introduction

Adhesion by or on microparticles plays a critical role in a wide range of developing and mature technologies, including drug delivery, catalysis, water/chemical purification, sensing, anti-fouling coatings and membranes, semiconductor device processing, composite processing, paints, printing, and xerography [1-10]. While predominant models and mechanistic experimental studies for understanding adhesion

have been based on smooth, spherical particles, microparticles with rough surfaces and non-spherical shapes are desired for a number of such technologies [11-17]. However, the scalable fabrication of microparticles with well-controlled surface asperities, in a variety of three-dimensional (3-D) morphologies, and with tailorable chemistries to allow for tunable adhesion remains a difficult synthetic challenge.

A rich sustainable source of 3-D microparticles, with complex morphologies affecting dispersion and adhesion in nature, is pollen. Pollen particles come in a wide variety of 3-D shapes and surface topographies, and are produced in large and growing quantities worldwide by plants [18-31]. Atomic force microscopy (AFM) based adhesion measurements, discussed in Chapter 2, have shown that the van der Waals (VDW) attraction of pollen particles to various inorganic and organic surfaces scales directly with the contact radii of asperities on the pollen surface; that is, the selection of pollen particles with particular surface structural features may be used to affect such VDW-based adhesion. The purpose of this chapter is to show, for the first time, how such pollen particles may be converted into 3-D ceramic replicas endowed with tunable multimodal adhesion. In this demonstration, native pollen particles have been converted, via use of a highly-conformal layer-by-layer (LbL) surface sol-gel (SSG) coating process, into 3-D replicas comprised of ferromagnetic hematite (α-Fe_2O_3) or ferrimagnetic magnetite (Fe_3O_4). The nanoscale surface topography, and the magnetic oxide content, of such high-fidelity replicas can provide for multimodal attraction to surfaces via both short-range VDW and short-to-long-range magnetic forces. Although other authors have used coating or infiltration methods to chemically modify/transform pollen and other biological microparticles for desired (bio)chemical, optical, electrical, structural, or fluid dynamic properties, the conversion of sustainable biogenic particles like pollen into all-inorganic 3-D replicas for the purpose of achieving tunable multimodal adhesion has not been reported [32-48].

4.3 Experimental

4.3.1 Material and Procedure

4.3.1.1 Pollen Preparation

The conversion of sunflower (*Helianthus annuus*) pollen (Greer Laboratories, Lenoir, NC USA) into iron oxide replicas has been examined in this work. The pollen grains were first cleaned by immersion in a mixture of chloroform and methanol (3:1) for 24 h, followed by deposition onto filter paper (P5, Fisher Scientific, Pittsburgh, PA USA) and drying under vacuum at 60 °C for 12 h [49]. A second immersion was conducted in 1 M hydrochloric acid (VWR, Suwanee, GA USA) for 1 h to remove residual inorganic material, followed by rinsing three times with de-ionized water, and drying by vacuum aspiration at room temperature for 5 min.

4.3.1.2 Computer-automated LbL SSG Deposition

Fe-O-bearing coatings were applied to cleaned pollen grains via a computer-automated, LBL SSG deposition process [50-53]. For the first step of a given SSG cycle, pollen grains were immersed for 10 min with stirring in a solution of 0.0125 M Fe(III) isopropoxide (Alfa Aesar, Ward Hill, MA USA) in anhydrous 2-propanol (>99.8% purity, Acros Organics, Geel, Belgium), to allow for the chemisorption of a Fe-O-bearing layer. After rinsing three times with anhydrous 2-propanol and vacuum filtration, the pollen grains were immersed in de-ionized water (DIW) with stirring for 5 min, to allow for hydrolysis of the chemisorbed alkoxide layer. The grains were then rinsed three times with anhydrous 2-propanol, vacuum filtered, and dried by vacuum aspiration for 5 min. This process (alkoxide exposure, 2-propanol rinsing, DIW exposure, 2-propanol rinsing, drying) was repeated for a total of 30 cycles to build up a Fe-O-bearing coating.

4.3.1.3 Thermal Processing

The coated pollen particles were heated in air at 0.5 °C min^{-1} to 600 °C and held at this temperature for 4 h to allow for organic pyrolysis and oxide crystallization. The

resulting hematite replicas were converted into magnetite via thermal treatment with a Rhines pack powder mixture of Fe (99% purity, Acros Organics) and Fe_3O_4 (99.95% purity, Alfa Aesar) [54]. The hematite pollen replicas were sealed along with the Fe/ Fe_3O_4 powder mixture ($Fe:Fe_3O_4:Fe_2O_3$ replica mole ratio = 14:14:1) inside a mild steel ampoule. The sealed samples were then heated at 3 °C min^{-1} to 550 °C and held at this temperature for 2 h. After cooling to room temperature, the ampoules were cut open and the magnetite pollen replicas were extracted.

4.3.2 Experimental Methods

4.3.2.1 Substrate Preparation and Characterization

Six types of substrates were utilized for adhesion studies: silicon (Si), polyvinyl alcohol (PVA), polyvinyl acetate (PVAc), polystyrene (PS), nickel (Ni), and a nickel-coated neodymium (Ni-Nd) alloy. The Si substrates (Silicon, Inc., Boise, ID USA) were piranha-etched using a solution of 75 vol.% sulfuric acid (97% purity, BDH Chemicals Ltd., Radnor, PA USA) and 25 vol.% hydrogen peroxide (30 wt.%, BDH Chemicals Ltd.) at 80 °C for 1 h. The polymer substrates (PVA, PVAc, PS) consisted of blade-cast polymer films on the cleaned Si substrates. Solutions comprised of 15 wt.% PS (MW = 100,000, Avoca-do Research Chemicals, Lancashire UK) in toluene (Sig-ma-Aldrich, St. Louis, MO USA), 20 wt.% PVAc (MW = 50,000, Alfa Aesar) in tetrahydrofuran (THF, BDH Chemicals Ltd.), or 3 wt.% PVA (MW = 89,000-98,000, Sigma-Aldrich) in hexafluoroisopropanol (HFIP, TCI America, Portland, OR USA) were used for blade casting. Blade casting (3540 Bird Film Applicator, Elcometer, Rochester Hills, MI USA) was conducted using a gap height of 1.2 mm, followed by slow drying under a saturated solvent environment for 2 days at 23 °C. The films were then air-dried for 2 days at 23 °C, followed by annealing in a vacuum oven for 1 day at 100 °C. The resulting polymer films possessed thicknesses ranging from 20 to 100 μm and completely covered the underlying Si substrate. Ni substrates were prepared by polishing (PM5 System, Logitech

Ltd., Glasgow, Scotland UK) nickel foil (0.150 mm thickness, grade 200, 99.5% purity, Shop-aid, Inc., Woburn, MA USA) to a surface finish of 0.06 μm using a colloidal SiO_2 suspension (Metlab Corp., Niagara Falls, NY USA). The Ni-Nd substrate consisted of an axially-poled, neodymium-iron-boron alloy permanent magnet disk (ND022N-35, 5 mm diameter, 1.5 mm thick, Master Magnetics, Inc., Castle Rock, CO USA) onto which was attached the polished nickel foil.

The surface roughness of each type of substrate was evaluated with a scanning probe microscope (Dimension 3100 SPM equipped with a Nanoscope V Controller, Veeco Instruments, Inc., Plainview, NY USA) operated in tapping mode at 200-400 kHz using a pyramidal tip silicon cantilever (Applied NanoStructures, Inc., Santa Clara, CA USA). For each particular substrate, 3 randomly-located scans (10 μm x 10 μm) were conducted, with each scan area split into 4 sectors. The average roughness value for a given substrate was obtained from analysis of these 12 sectors.

4.3.2.2 Pollen and Pollen Replica Characterization

Scanning electron microscopy (SEM) was conducted with a field emission gun instrument (Carl Zeiss SMT, Ltd., Thorn-wood, NY USA) equipped with an energy dispersive X-ray spectrometer (INCA EDS, Oxford Instruments, Abingdon, Oxfordshire UK). The average spine tip radii of cleaned sunflower pollen particles, and of oxide replicas of sunflower pollen particles, were obtained from SEM images of particles attached to cantilever probes (described below). For each particle-bearing probe, 5 spine tips located closest to the position where the particle made contact to the substrates were evaluated (for a total of 15 analyzed spine tips for all 3 similar types of particle-bearing probes). X-ray diffraction (XRD) analyses were conducted with Cu Kα radiation using a diffractometer (X-Pert Pro Alpha 1, PANalytical, Almelo, The Netherlands) equipped with an incident beam Johannsen monochromator (PANalytical) and an Xcelerator linear detector (PANalytical). Thermogravimetric (TG) analysis was used to assess the presence

of organic pollen material remaining after conversion to α-Fe_2O_3 and Fe_3O_4 replicas. TG analyses were carried out in a temperature range of 30-600 °C, in air and with a constant heating rate of 50 °C min^{-1} for all experiments. The sample mass was ~0.5 g for all measurements.

4.3.2.3 Adhesion Measurements

Adhesion measurements were conducted using colloidal probes consisting of a single particle (a native sunflower pollen particle or oxide replica particle) attached to an atomic force microscope (AFM) cantilever. A small amount of epoxy resin (Epoxy Marine, Loctite, Westlake, OH USA) was used to attach a given particle to a tipless silicon AFM cantilever (FORT-TL, Applied NanoStructures, Inc.). For each type of pollen-shaped particle (cleaned sunflower pollen, α-Fe_2O_3 replica, or Fe_3O_4 replica), three single-particle-bearing cantilever probes were prepared (for a total of 9 particle/cantilever probes). The spring constants, as determined with the scanning probe microscope, of the sunflower-pollen-bearing, α-Fe_2O_3-replica-bearing, and Fe_3O_4-replica-bearing cantilever probes fell in the ranges of 1.84-2.34 N/m, 1.19-1.91 N/m, and 1.63-1.69 N/m, respectively. The adhesion force between an individual sunflower pollen particle, or oxide replica particle, and a particular substrate was evaluated with the scanning probe microscope operated in contact mode. For each particular particle/cantilever probe and particular substrate, 20 separate force-distance scans were randomly obtained, and the depth of adhesion wells upon retraction were averaged. The load force applied during the contact adhesion measurements was 2.5 nN. The ambient relative humidity in the laboratory during the adhesion measurements ranged from 30 to 35%.

4.4 Results and Discussion

4.4.1 Pollen Replica Preparation

Sunflower pollen particles were converted into magnetic oxide replicas via use of a computer-automated LbL SSG coating process [50-53]. SEM images of a starting,

cleaned pollen grain are shown in Figure 4.1a. The sunflower pollen grains were roughly spherical in shape and possessed echini (spines) of relatively high aspect ratio (height:width-at-midheight ratio of ~5:1). Because the exine (outer layer) of such pollen grains is comprised of sporopollenin (a complex polymer consisting of carboxylic acids and aromatic moieties cross-linked with aliphatic chains), the pollen surfaces were enriched with hydroxyl groups that provided an abundance of reaction sites for the chemisorption of alkoxide precursors during the SSG coating process [55-57]. An SEM image and energy-dispersive X-ray (EDX) analysis of a sunflower pollen particle after exposure to 30 SSG deposition cycles are shown in Figures 4.1b and 4.2b, respectively. Comparison of the EDX analyses in Figures 4.2a and 4.2b confirmed that the SSG-coated particle was enriched in iron and oxygen. The highly-conformal nature of the SSG Fe-O-bearing coating was evident from the preservation of the echini and the fine pores at the base of the echini (as indicated by the arrows in Figure 4.1b).

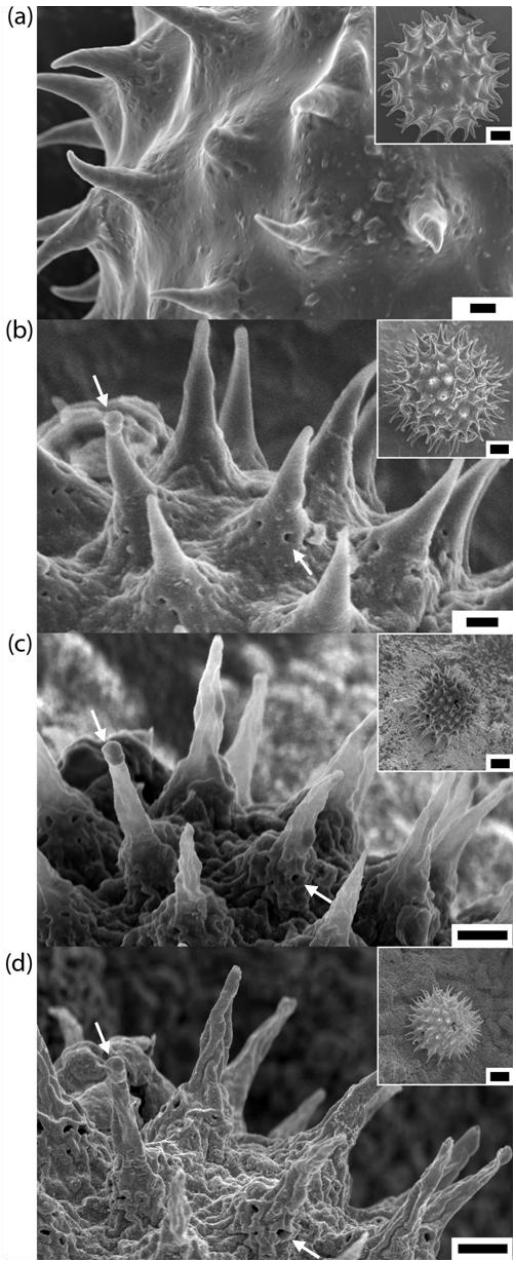

Figure 4.1. SEM images of sunflower pollen particles at various stages of conversion into Fe_3O_4: a) the exine of a natural grain, b) an Fe-O-coated grain after 30 SSG deposition cycles, c) an α-Fe_2O_3 replica of the same grain in b) after pyrolysis at 600 ^{0}C for 4 h in air, d) a Fe_3O_4 replica of the same α-Fe_2O_3 grain in c) generated by partial reduction using a Rhines pack (Fe/ Fe_3O_4) at 550 ^{0}C for 3 h. The scale bars indicate 5 µm for the low-magnification insert images and 2 µm for the higher-magnification images.

The coated pollen particles were then heated in air at 600 °C for 4 h to allow for pyrolysis of the pollen template, and crystallization of the oxide coating. Complete pyrolysis of the sporopollenin during this treatment was confirmed by thermogravimetric (TG) analysis (Figure 4.3). TG analyses shows that with increasing number of coating layers, the remaining mass after pyrolysis increases from 9.8% with 10 layers to 13.8% with 20 layers and to 17.7% with 30 layers. TG analyses also shows that at 600 °C all the organic material of the sunflower pollen has been pyrolized, with 0.4% of inorganic ash remaining. EDX analyses (Figure 4.2c) also revealed the loss of carbon, and retention of iron and oxygen, after such pyrolysis. X-ray diffraction (XRD) analysis (Figure 4.4a) indicated that these fired particles were comprised of phase-pure, nanocrystalline hematite (α-Fe_2O_3). Scherrer analyses of the XRD peaks yielded an average hematite crystallite size of 35 nm. Although smaller than the starting, as-coated pollen particles, these hematite particles retained the 3-D shapes and surface features of the starting pollen grains (Figure 4.1c). Indeed, the high-fidelity nature of such replication was revealed by SEM images of *the same particle* before (Figure 4.1b) and after (Figure 4.1c) the thermal treatment (note: the arrows in Figures 4.1b and 4.1c reveal the same spine and fine pore present before and after this thermal treatment). Conversion of the hematite replicas into magnetite was conducted via use of a thermal treatment with a Rhines pack [54]. The oxygen partial pressure established within the ampoule by the Fe/ Fe_3O_4 equilibrium at 550 °C (note: wüstite, $Fe_{1-x}O$, is thermodynamically unstable below 570 °C) allowed for complete conversion of the replica particles into phase-pure nanocrystalline magnetite, as confirmed by XRD analysis (Figure 4.4b) [58]. Scherrer analyses yielded an average magnetite crystallite size of 34 nm. SEM images (Figure 4.1d) indicated that the 3-D morphology and sharp echini of the sunflower pollen were retained by the magnetite replicas (note: the arrows in Figures 4.1c and 4.1d show the same spine and fine pore before and after this Rhines pack thermal treatment). No detectable change in replica

particle size was detected upon conversion of the hematite into magnetite, which was consistent with the similarity in the volumes of these oxides on a per mole of iron basis (15.2 cm^3 Fe_2O_3/mole Fe; 14.9 cm^3 Fe_3O_4/mole Fe).

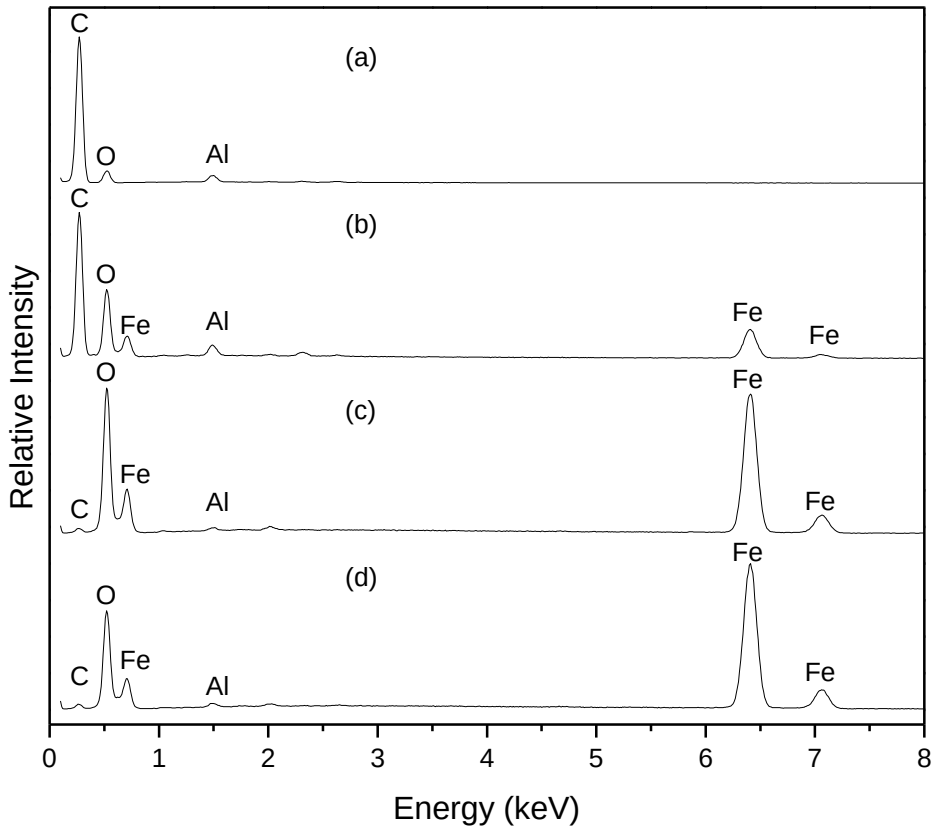

Figure 4.2. EDX analyses of: a) the exine of a natural sunflower pollen grain, b) an Fe-O-coated sunflower grain after 30 SSG deposition cycles, c) an α-Fe_2O_3 replica of a sunflower grain generated by pyrolysis at 600 ^{0}C for 4 h in air, and d) a Fe_3O_4 replica of a α-Fe_2O_3 grain generated by partial reduction using a Rhines pack (Fe/ Fe_3O_4 powder mixture) at 550 ^{0}C for 3 h. (Note: the Al peak was obtained from the underlying aluminum stub used to support the particles during EDX analyses.)

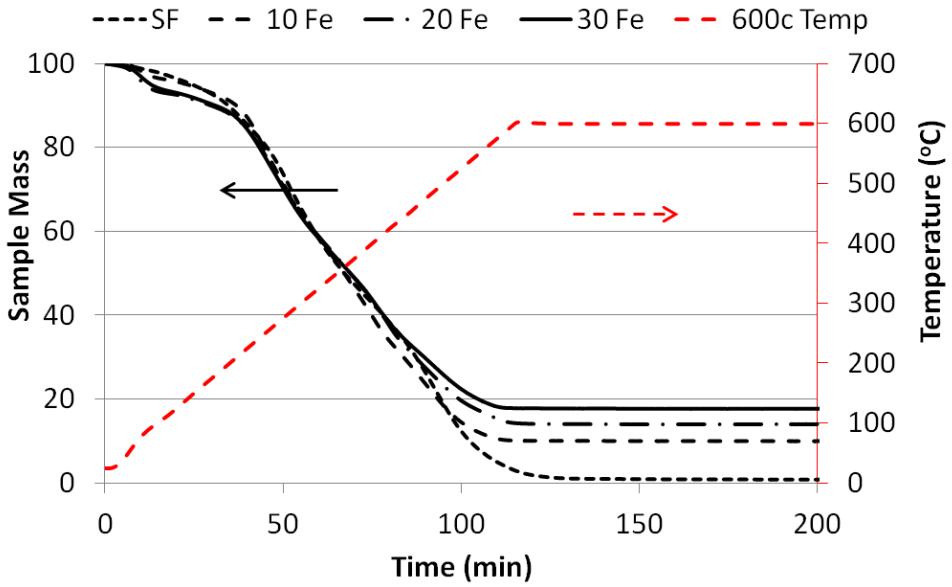

Figure 4.3. TG analysis of sunflower pollen grains and Fe-O-coated sunflower pollen (10, 20, and 30 SSG deposition cycles) during pyrolysis by heating in air at 5 °C min^{-1} to 600 °C.

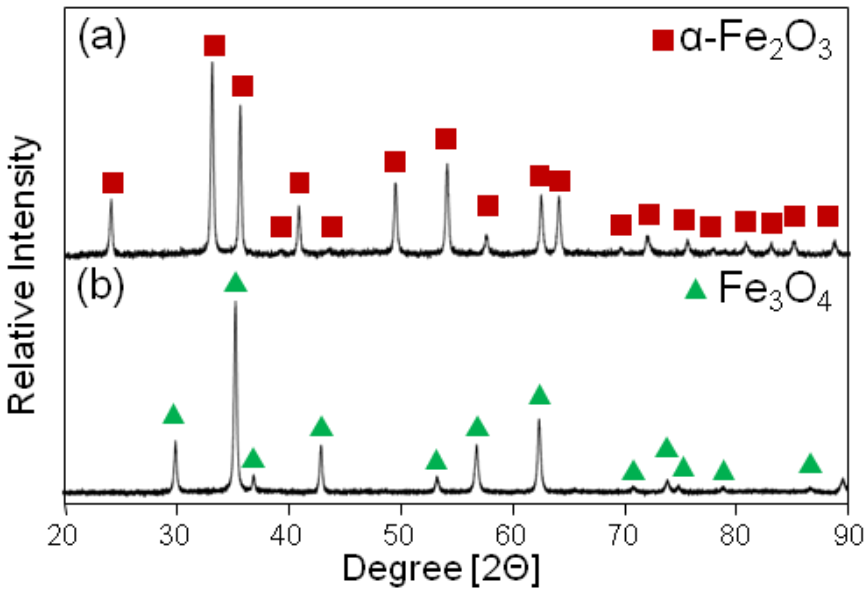

Figure 4.4. XRD analyses of iron oxide replicas of sunflower pollen generated by exposing the pollen particles to 30 SSG LbL deposition cycles and then: a) firing at a peak temperature of 600 °C for 4 h in air, followed by b) sealing the resulting α-Fe_2O_3 samples, along with an excess powder mixture of Fe and Fe_3O_4 (a Rhines pack), within a mild steel ampoule and heating to a peak temperature of 550 °C for 2 h.

4.4.2 Pollen and Pollen Replica Adhesion

To allow for quantitative evaluation of the adhesion of the sunflower pollen and oxide pollen replicas to various substrate surfaces, the pollen and replica particles were attached to AFM cantilevers (Figure 4.5) using a procedure described previously [59]. Six substrates were chosen to analyze the effects of substrate surface chemistry and magnetic properties on particle attraction. Polyvinyl alcohol (PVA) and polyvinyl acetate (PVAc) were selected as model proton donor and proton acceptor substrates, respectively. Polystyrene (PS) was chosen as a model apolar hydrocarbon substrate. Piranha-etched silicon (Si), which possessed a thin (~2-10 nm) hydroxylated oxide layer, acted as a hydrophilic substrate [60]. Unpoled, polished nickel (Ni) foil served as a weakly ferromagnetic substrate. An axially-poled, neodymium-iron-boron alloy was used as a strongly-magnetized ferromagnetic substrate (residual induction = 12,300 G). The polished nickel foil was attached to this permanent magnet to provide a substrate (Ni-Nd) with the same roughness as the Ni substrate. The measured average surface roughness values of the six substrates fell within a range of 0.2 to 2.8 nm (Table 4.1).

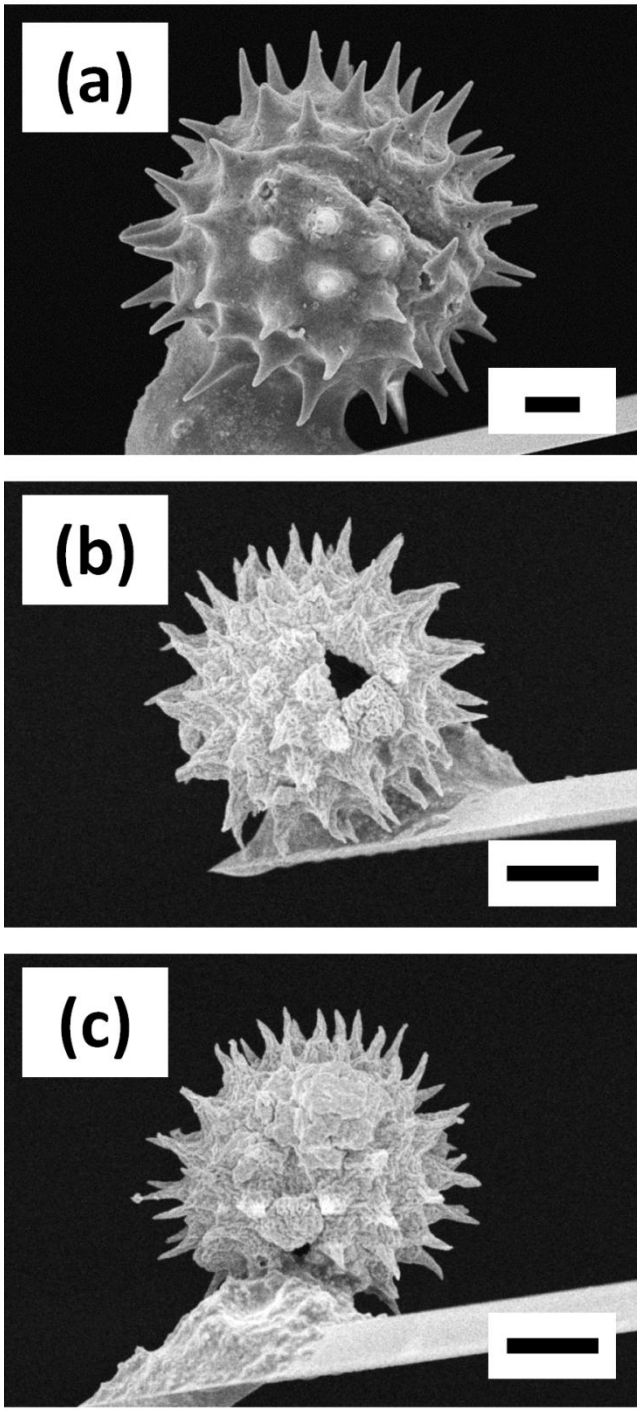

Figure 4.5. SEM images of single-particle-bearing cantilever probes containing: a) a cleaned sunflower pollen grain, b) an α-Fe_2O_3 sunflower pollen replica, and c) a Fe_3O_4 sunflower pollen replica used in the AFM adhesion study. The scale bars indicate 5 µm.

Table 4.1. Average surface roughness (Ra, in nm) of the substrates used in this study. Error indicates a range of ± one standard deviation.

Si	PVA	PVAc	PS	Ni	Ni-Nd
0.2 ± 0.06	1.3 ± 0.03	0.3 ± 0.06	0.3 ± 0.02	2.7 ± 0.7	2.8 ± 0.4

Contact mode AFM measurements were used to evaluate the short-range (VDW-based) adhesion of the sunflower pollen, and the hematite and magnetite replica particles, to the Si, PVA, PVAc, PS, Ni, and Ni-Nd substrates. Average values of the VDW-based adhesion for the different particle and substrate combinations are shown in Figure 4.6 (note: each average value was obtained from 60 measurements consisting of 20 analyses for each of three similar particle/cantilever probes). Given the observed range in measured values, no appreciable difference in contact mode adhesion force was detected for each type of particle on different substrates. Combining the data from all of the substrates for a given type of particle yielded average VDW adhesion force values of 55 ± 9 nN, 36 ± 7 nN, and 34 ± 7 nN for the cleaned sunflower pollen, α-Fe_2O_3 replicas, and Fe_3O_4 replicas, respectively.

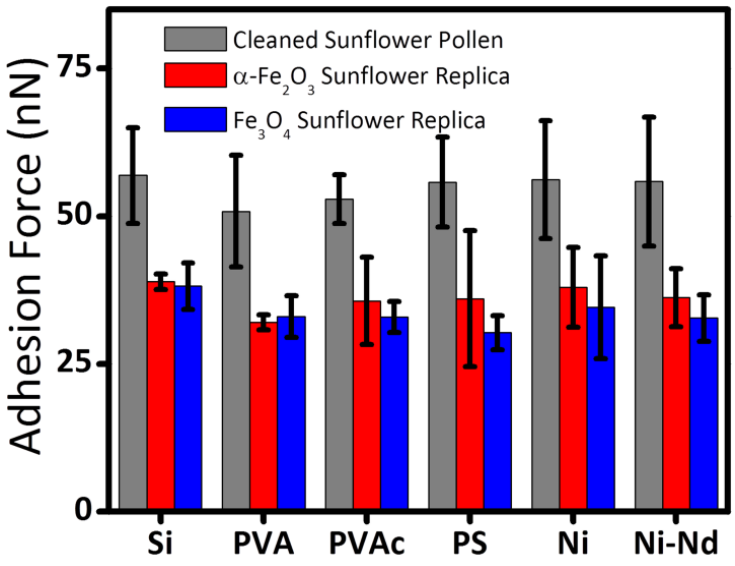

Figure 4.6. AFM measurements of short-range VDW-based adhesion forces for cleaned sunflower pollen probes, α-Fe_2O_3 sunflower replica probes, and Fe_3O_4 sunflower replica probes on various substrates (note: measurements on the disk-shaped Ni-Nd substrate were conducted at its outer edge). The error bars indicate a range of ± one standard deviation.

First order analyses of these values of VDW-based adhesion force were conducted using the following Hamaker relation in Eq. (4.1):

$$F_{vdw} = \frac{A_{132}R}{6D^2} \tag{4.1}$$

where A_{132} is the non-retarded Hamaker constant of material 1 and 2 interacting across a medium 3 (air), R is the contact radius, and D is the cutoff separation distance for the VDW interaction (≈ 0.165 nm) [61]. Approximate A_{132} values for sunflower pollen on the Si, PVA, PVAc, and PS substrates were calculated from appropriate A_{11} and A_{22} values available in the literature, and with the assumption that $A_{33} = 0$, via Eq. (4.2) [59, 61-66]:

$$A_{132} \approx A_{11}^{1/2} A_{22}^{1/2} \tag{4.2}$$

The simplified expression in Eq. (4.2) is not applicable, however, to media with high dielectric constants. Therefore, interactions involving hematite and magnetite were calculated on the basis of the Lifshitz theory via Eq. (4.3) [61]:

$$A_{132} \approx \frac{3}{4}kT\left(\frac{\varepsilon_1-\varepsilon_3}{\varepsilon_1+\varepsilon_3}\right)\left(\frac{\varepsilon_2-\varepsilon_3}{\varepsilon_2+\varepsilon_3}\right)+\frac{3h\nu_e}{8\sqrt{2}}\frac{\left(n_1^2-n_3^2\right)\left(n_2^2-n_3^2\right)}{\left(n_1^2+n_3^2\right)^{1/2}\left(n_2^2+n_3^2\right)^{1/2}\left\{\left(n_1^2+n_3^2\right)^{1/2}+\left(n_2^2+n_3^2\right)^{1/2}\right\}} \quad (4.3)$$

where k is Boltzmann's constant, T is temperature, h is Planck's constant, ν_e is the media absorption frequency, ε_1 and ε_2 are dielectric constants, and n_1 and n_2 are refractive indices. A_{132} values for sunflower pollen on the Ni or Ni-Nd substrates and hematite or magnetite replicas on all substrates were calculated from Eq. (4.3) by using appropriate ε_1, ε_2, n_1, and n_2 values available in the literature, with the assumption that the absorption frequencies of all media are the same [67-73]. We took the ε_1 value for sporopollenin to be the average of the values for PS, PVAc, and PVA for lack of a literature value. This assumption is consistent with the organic content of sporopollenin and produces A_{132} values of the expected magnitude. If the substrate is assumed to be flat, then R in Eq. (4.1) refers to the contact radius of the spine tip from the probe particle. By inserting the measured average values of adhesion force into Eq. (4.1) along with the calculated A_{132} constants, values of contact radii for the cleaned sunflower pollen, α-Fe_2O_3 replicas, and Fe_3O_4 replicas with the various substrates were calculated (Table 4.2) to be 93 ± 14 nm, 27 ± 8 nm, and 25 ± 8 nm, respectively. For the native sunflower pollen, the calculated contact radius (93 ± 14 nm) was similar to the average spine-tip radius (120 ± 12 nm) measured by SEM analysis; that is, the VDW-based adhesion force for this native pollen particle was consistent with the contact of a single spine tip to a given substrate. However, the calculated contact radii for the hematite (27 ± 8 nm) and magnetite (25 ± 8 nm) replica particles were much smaller than the average spine tip radii of these replicas (i.e., 94 ± 14 nm and 100 ± 14 nm for hematite and magnetite, respectively) obtained

from SEM analyses. Instead, the calculated contact radii for these oxide replicas were not far from the average crystallite radii (17-18 nm) of these particles obtained from XRD analyses; that is, the VDW-based adhesion forces of the oxide pollen replicas were consistent with the contact of one or two nanocrystals located at the spine tips to the substrates.

Variations in substrate roughness will have some effect on measured adhesion values. The pollen tip radii are considerably larger than the roughness variation, and the expected effect of increased roughness would be to decrease contact area and decrease adhesion forces. This behavior could potentially obscure calculated pollen-tip and replica crystallite radii. However, in Figure 4.6, for surfaces that have the same Hamaker constant (PS, PVA), changes in roughness from 0.3 nm (PS) to 1.3 nm (PVA) do not have a measureable effect on the adhesive forces. Examining other values in Table 4.1 and Figure 4.6, we conclude that one cannot detect any consistent trend between roughness and adhesion force within the measurement precision.

Table 4.2. Average measured values of adhesion force, calculated Hamaker constants, and calculated contact radii. Error indicates a range of one standard deviation.

	Si	PVA	PVAc	PS	Ni	Ni-Nd
Cleaned Sunflower						
A_{132} ($x10^{19}$)	0.85	0.84	0.98	0.84	1.2	1.2
Force (nN)	57± 8	51 ± 9	53 ± 4	56 ± 8	56 ± 10	56 ± 11
Radius (nm)	109	98	88	109	78	77
Hematite						
A_{132} ($x10^{19}$)	1.7	2.0	1.8	2.1	3.4	3.4
Force (nN)	39 ± 1	32 ± 1	36 ± 7	36 ± 11	38 ± 7	36 ± 5
Radius (nm)	37	27	32	28	18	17
Magnetite						
A_{132} ($x10^{19}$)	1.7	2.0	1.8	2.1	3.4	3.4
Force (nN)	38 ± 4	33 ± 3	33 ± 3	30 ± 3	35 ± 9	33 ± 4
Radius (nm)	36	27	30	24	17	16

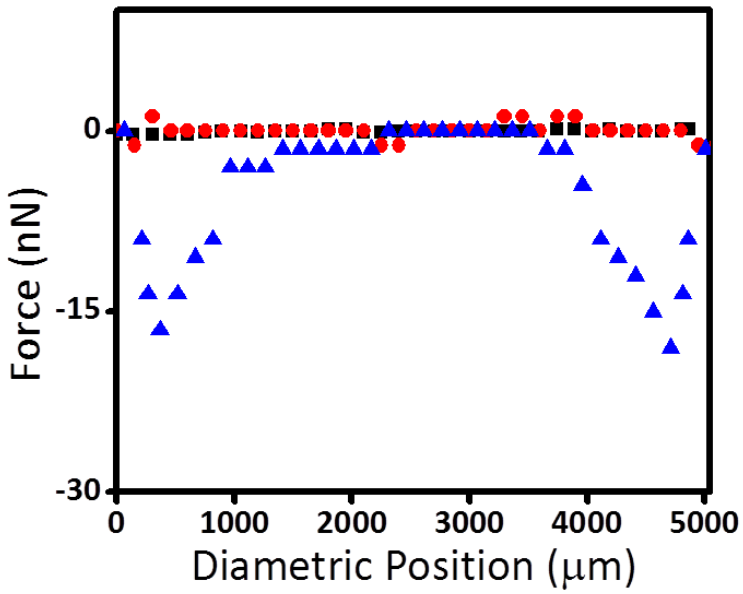

Figure 4.7. Analyses of the magnetic force acting on cleaned sunflower pollen, α-Fe_2O_3 sunflower pollen replicas, and Fe_3O_4 sunflower pollen replicas upon scanning across the diameter of the permanent magnet Ni-Nd substrate at a fixed height of 140 µm above the substrate surface.

4.4.3. Pollen and Pollen Replica Long-Range Forces

The longer-range magnetic forces acting between particle/cantilever probes and the axially-magnetized, permanent magnet Ni-Nd substrate were evaluated by scanning the probes across the diameter of this disk-shaped substrate at a fixed height of 140 µm above the substrate surface. As revealed in Figure 4.7, a noticeable attractive force was detected between the ferrimagnetic Fe_3O_4 sunflower pollen replica and the disk-shaped Ni-Nd substrate at locations near the outer perimeter of this substrate, which was where the magnetic field intensity associated with this magnetized Ni-Nd substrate was highest [74]. No appreciable magnetic attraction was detected between the weakly ferromagnetic α-Fe_2O_3 replicas, or the non-magnetic native sunflower pollen, at any location across the Ni-Nd substrate (at a distance of 140 µm from the surface of this substrate). To demonstrate this effect, the magnetic response of the magnetic replicas is seen in Figure

4.8. When a magnetic is placed next to both the hematite and magnetite sample, only the magnetite replicas are visibly affected.

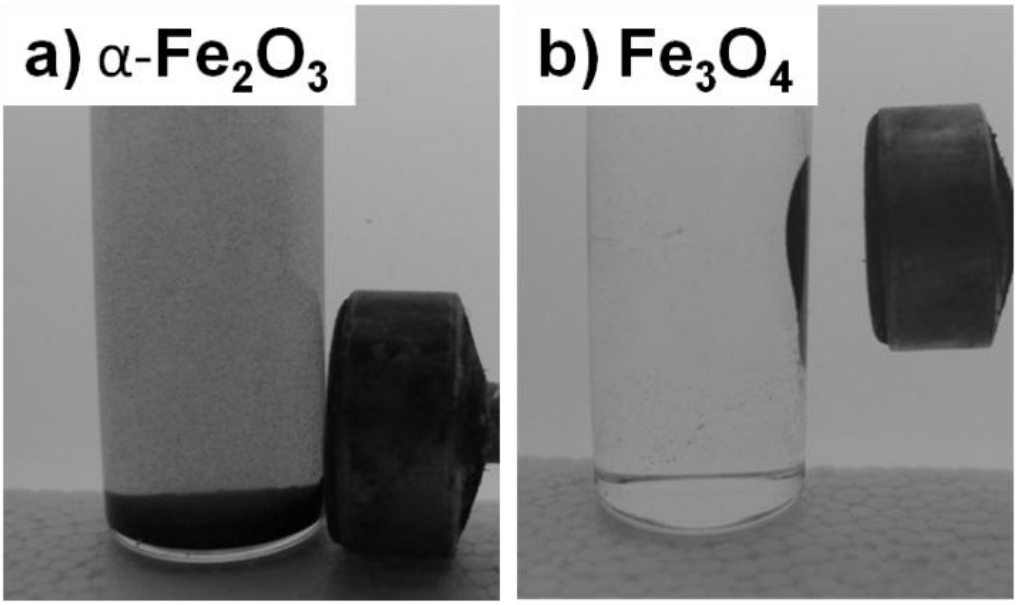

Figure 4.8. Optical images of sunflower replicas in DIW next to a permanent magnet: a) α -Fe_2O_3 sunflower pollen replicas and b) Fe_3O_4 sunflower pollen replicas.

The total adhesion force acting between a given type of particle and the Si or Ni-Nd substrate is plotted against probe distance from the substrate surface in Figure 4.9 (note: for the Ni-Nd substrate, measurements were obtained either at the disk center or at a distance of ~300 μm from the edge of the Ni foil). Only short range (~10 nm) attractive forces were detected between the native sunflower pollen, or α-Fe_2O_3 sunflower replicas, and these substrates (Figures 4.9a and 4.9b). However, both magnetic and VDW attractive forces were detected (Figure 4.9c) between the Fe_3O_4 sunflower pollen replicas and the magnetized Ni-Nd near the outer edge of this substrate. For this Fe_3O_4 particle/Ni-Nd-edge substrate pairing, the total adhesion force (~70 nN) acting over a short distance (~10 nm) consisted of the sum of the VDW force (~40 nN) and the magnetic force (~30 nN). At distances just beyond the range of VDW-based adhesion, a steady magnetic force (~30 nN) was detected. The magnetic interaction between the

Fe_3O_4 sunflower pollen replicas and the magnetized edge of the Ni-Nd substrate persisted out to a separation distance of ~1 mm.

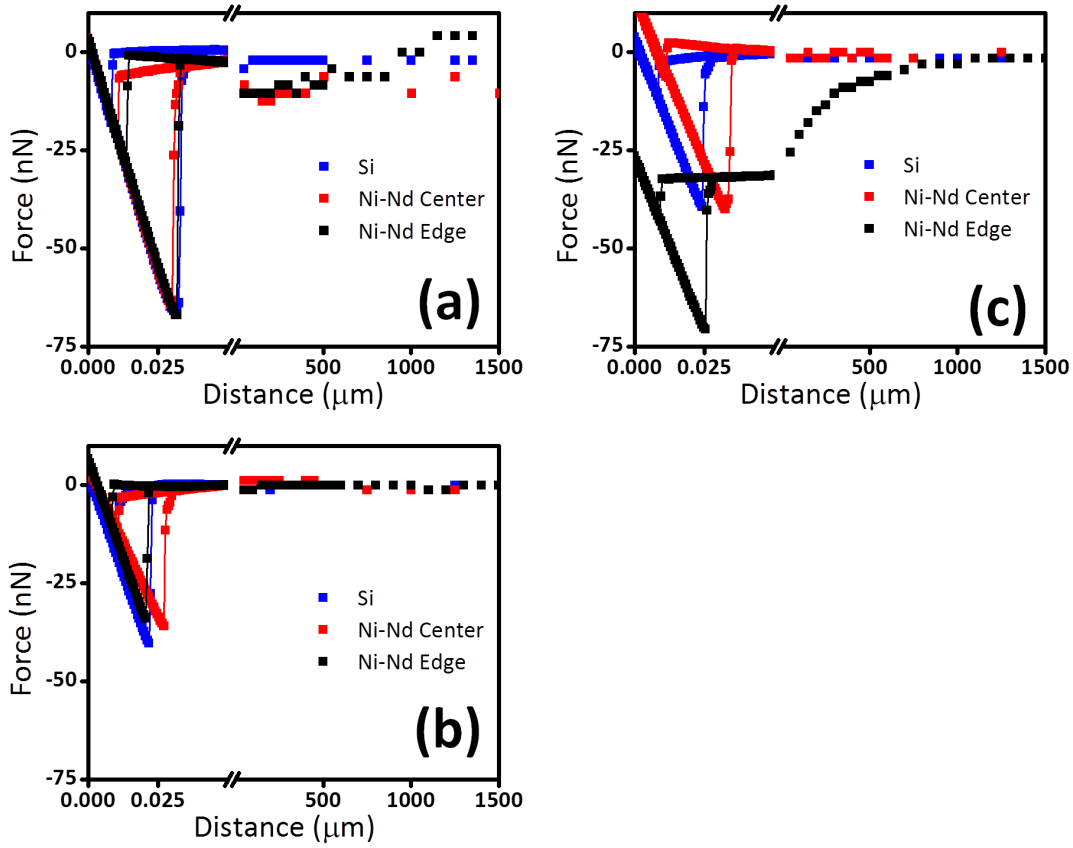

Figure 4.9. AFM measurements of the total (VDW + magnetic) adhesion force vs. distance for: a) a cleaned sunflower pollen probe, b) an α-Fe_2O_3 sunflower replica probe and c) a Fe_3O_4 sunflower pollen replica probe with the Si substrate and the Ni-Nd substrate (Ni-Nd Center and Ni-Nd Edge refer to analyses obtained at the center and at ~300 μm from the edge, respectively, of the disk-shaped Ni-Nd substrate).

This chapter demonstrates that a highly-conformal LbL SSG coating process can be used, along with controlled modest-temperature thermal treatments, to convert sunflower pollen particles into nanocrystalline ferrimagnetic (Fe_3O_4) replicas exhibiting multimodal adhesion via short-range (~10 nm) VDW-based attraction and short-to-long-range (up to ~1 mm) magnetic attraction. Although the work here has focused on

generating oxide replicas of sunflower pollen, this process may generally be applied to numerous other types of pollen. Indeed, the wide variety of 3-D particle shapes and surface topographies available from pollen generated by different plants, and the ability of this LbL SSG-based process to produce high-fidelity nanocrystalline replicas with controlled amounts of magnetic oxide (by adjusting the number of deposited layers), allows for the syntheses of pollen-derived microparticles with highly-tailorable multimodal adhesion.

4.5 Conclusions

This chapter demonstrates, for the first time, the ability to generate high-fidelity, all-oxide replicas of pollen particles exhibiting tailorable multimodal (short-range VDW and short-to-long-range magnetic) adhesion. The hydroxyl-rich nature of the exine of pollen has allowed for the use of a computer-automated, LbL SSG process to apply highly-conformal Fe-O-bearing coatings to pollen particles. For this demonstration, sunflower pollen (*Helianthus annuus*), with surfaces containing sharp, high-aspect-ratio spines, has been coated with 30 Fe-O-bearing layers. Subsequent firing at 600 °C in air yielded high-fidelity replicas comprised of nanocrystalline, phase-pure ferro-magnetic hematite (α-Fe_2O_3). Partial reduction of these hematite replicas, via use of a controlled oxygen partial pressure (Rhines pack-based) heat treatment, yielded nanocrystalline, phase-pure ferrimagnetic magnetite (Fe_3O_4) replicas. The Fe_3O_4 replicas were found to exhibit short-range (~10 nm) VDW-based adhesion, governed by the contact of oxide nanocrystals present on the sharp spines inherited from the starting sunflower pollen, and short-to-long-range (up to 1 mm) magnetic adhesion governed by the ferrimagnetic magnetite. By selecting pollen with particular 3-D morphologies and surface features, and by using the LbL SSG process to tailor the amount of nanocrystalline magnetite present in the ceramic replicas, microparticles with tunable short-range (VDW-based) and longer-range (magnetic) adhesion can be synthesized.

Acknowledgement: We are grateful to Dr. Ken Sandhage and Brandon Goodwin for their contributions to this work. They performed the preparation and characterization of hematite and magnetite pollen replicas and supplied the data in Figures 4.1, 4.2, 4.3, 4.4, and 4.8.

4.6 References

1. Ott, M.L. and H.A. Mizes, *Atomic force microscopy adhesion measurements of surface-modified toners for xerographic applications.* Colloids and Surfaces A: Physicochemical and Engineering Aspects, 1994. **87**(3): p. 245-256.

2. Richard Bowen, W. and T.A. Doneva, *Atomic force microscopy studies of membranes: Effect of surface roughness on double-layer interactions and particle adhesion.* Journal of Colloid and Interface Science, 2000. **229**(2): p. 544-549.

3. Cooper, K., A. Gupta, and S. Beaudoin, *Simulation of the adhesion of particles to surfaces.* Journal of Colloid and Interface Science, 2001. **234**(2): p. 284-292.

4. Meitl, M.A., et al., *Transfer printing by kinetic control of adhesion to an elastomeric stamp.* Nature materials, 2005. **5**(1): p. 33-38.

5. Mitragotri, S. and J. Lahann, *Physical approaches to biomaterial design.* Nature materials, 2009. **8**(1): p. 15-23.

6. Huang, Y., et al., *Controllable Underwater Oil-Adhesion-Interface Films Assembled from Nonspherical Particles.* Advanced Functional Materials, 2011. **21**(23): p. 4436-4441.

7. Fischer, K.E., et al., *Hierarchical nanoengineered surfaces for enhanced cytoadhesion and drug delivery.* Biomaterials, 2011. **32**(13): p. 3499-3506.

8. Zhang, L., et al., *Facile preparation of robust microcapsules by manipulating metal-coordination interaction between biomineral layer and bioadhesive layer.* ACS Applied Materials & Interfaces, 2011. **3**(2): p. 597-605.

9. Stassi, S. and G. Canavese, *Spiky nanostructured metal particles as filler of polymeric composites showing tunable electrical conductivity.* Journal of Polymer Science Part B: Polymer Physics, 2012. **50**(14): p. 984-992.

10. Lee, I., *Molecular Self-Assembly: Smart Design of Surface and Interface via Secondary Molecular Interactions.* Langmuir, 2013. **29**(8): p. 2476-2489.

11. Johnson, K., K. Kendall, and A. Roberts, *Surface energy and the contact of elastic solids.* Proceedings of the Royal Society of London. A. Mathematical and Physical Sciences, 1971. **324**(1558): p. 301-313.

12. Derjaguin, B., V. Muller, and Y.P. Toporov, *Effect of contact deformations on the adhesion of particles.* Journal of Colloid and Interface Science, 1975. **53**(2): p. 314-326.

13. Tabor, D., *Surface forces and surface interactions.* Journal of Colloid and Interface Science, 1977. **58**(1): p. 2-13.

14. Muller, V., V. Yushchenko, and B. Derjaguin, *On the influence of molecular forces on the deformation of an elastic sphere and its sticking to a rigid plane.* Journal of Colloid and Interface Science, 1980. **77**(1): p. 91-101.

15. Maugis, D. and H. Pollock, *Surface forces, deformation and adherence at metal microcontacts.* Acta Metallurgica, 1984. **32**(9): p. 1323-1334.

16. Ducker, W.A., T.J. Senden, and R.M. Pashley, *Direct measurement of colloidal forces using an atomic force microscope.* Nature, 1991. **353**(6341): p. 239-241.

17. Maugis, D., *Adhesion of spheres: the JKR-DMT transition using a Dugdale model.* Journal of Colloid and Interface Science, 1992. **150**(1): p. 243-269.

18. Kremp, G.O.W., *Morphologic encyclopedia of palynology; an international collection of definitions and illustrations of spores and pollen*. Arizona University Program in geochronology, contribution1965, Tuscon,: University of Arizona Press. xiii, 185 p.

19. Walker, J.W. and J.A. Doyle, *The bases of angiosperm phylogeny: palynology.* Annals of the Missouri Botanical Garden, 1975. **62**: p. 664-723.

20. Erdtman, G., *Pollen morphology and plant taxonomy*. Vol. 1. 1986: E.J. Brill: Leiden, The Netherlands.

21. Blackmore, S. and S.H.e. Barnes, *Pollen and spores: patterns of diversification*1991: Clarendon Press: Oxford, UK. xi, 391 p.

22. Ressayre, A., et al., *Aperture pattern ontogeny in angiosperms.* Journal of Experimental Zoology, 2002. **294**(2): p. 122-135.

23. Hesse, M., *Pollen terminology : an illustrated handbook* 2009, Wien ; New York: Springer. 261 p.

24. Horn, E., *A summer hay fever plant survey of Manhattan, Kansas.* Transactions of the Kansas Academy of Science (1903-), 1933. **36**: p. 91-97.

25. Grater, W.C. and T.R. Stemen, *The plant, the pollen and the patient.* Review of Palaeobotany and Palynology, 1967. **4**(1): p. 187-192.

26. Ziska, L.H., et al., *Cities as harbingers of climate change: common ragweed, urbanization, and public health.* Journal of allergy and clinical immunology, 2003. **111**(2): p. 290-295.

27. Beggs, P., *Impacts of climate change on aeroallergens: past and future.* Clinical & Experimental Allergy, 2004. **34**(10): p. 1507-1513.

28. Rogers, C.A., et al., *Interaction of the onset of spring and elevated atmospheric CO2 on ragweed (Ambrosia artemisiifolia L.) pollen production.* Environmental Health Perspectives, 2006. **114**(6): p. 865-869.

29. Fumanal, B., B. Chauvel, and F. Bretagnolle, *Estimation of pollen and seed production of common ragweed in France.* Annals of Agricultural and Environmental Medicine, 2007. **14**(2): p. 233.

30. Ziska, L., et al., *Recent warming by latitude associated with increased length of ragweed pollen season in central North America.* Proceedings of the National Academy of Sciences, 2011. **108**(10): p. 4248-4251.

31. Bajin, M.D., et al., *Global warming and allergy in Asia Minor.* European Archives of Oto-Rhino-Laryngology, 2013. **270**(1): p. 27-31.

32. Hall, S.R., H. Bolger, and S. Mann, *Morphosynthesis of complex inorganic forms using pollen grain templates.* Chem. Commun., 2003(22): p. 2784-2785.

33. Wang, Y., et al., *Replication of biological organizations through a supercritical fluid route.* Chemical Communications, 2005(23): p. 2948-2950.

34. Hall, S.R., et al., *Fabrication of porous titania (brookite) microparticles with complex morphology by sol-gel replication of pollen grains.* Chemistry of Materials, 2006. **18**(3): p. 598-600.

35. Li, P., et al., *Hydrothermal Synthesis of TiO2 Hollow Spheres Using Rapeseed Pollen Grains as Template.* Journal of Inorganic Materials, 2008. **23**(1): p. 49-54.

36. Cao, F. and D.-X. Li, *Morphology-controlled synthesis of SiO2 hollow microspheres using pollen grain as a biotemplate.* Biomedical Materials, 2009. **4**(2): p. 025009.

37. Yang, X., et al., *Synthesis of spinous ZrO2 core–shell microspheres with good hydrogen storage properties by the pollen bio-template route.* Scripta Materialia, 2011. **64**(12): p. 1075-1078.

38. Thio, B.J.R., K.K. Clark, and A.A. Keller, *Magnetic pollen grains as sorbents for facile removal of organic pollutants in aqueous media.* Journal of hazardous materials, 2011. **194**: p. 53-61.

39. Xia, Y., et al., *Biotemplated fabrication of hierarchically porous NiO/C composite from lotus pollen grains for lithium-ion batteries.* Journal of Materials Chemistry, 2012. **22**(18): p. 9209-9215.

40. Anderson, M.W., et al., *Hierarchical pore structures through diatom zeolitization.* Angewandte Chemie, 2000. **112**(15): p. 2819-2822.

41. Rosi, N.L., C.S. Thaxton, and C.A. Mirkin, *Control of Nanoparticle Assembly by Using DNA-Modified Diatom Templates.* Angewandte Chemie, 2004. **43**(41): p. 5500-5503.

42. Gaddis, C.S. and K.H. Sandhage, *Freestanding microscale 3D polymeric structures with biologically-derived shapes and nanoscale features.* Journal of materials research, 2004. **19**(09): p. 2541-2545.

43. Zhao, J., et al., *Free-standing microscale structures of nanocrystalline zirconia with biologically replicable three-dimensional shapes.* Journal of materials research, 2005. **20**(02): p. 282-287.

44. Payne, E.K., et al., *Sacrificial biological templates for the formation of nanostructured metallic microshells.* Angewandte Chemie International Edition, 2005. **44**(32): p. 5064-5067.

45. Weatherspoon, M.R., et al., *Phosphor microparticles of controlled three-dimensional shape from phytoplankton.* Journal of The Electrochemical Society, 2006. **153**(2): p. H34-H37.

46. Losic, D., et al., *Rapid Fabrication of Micro-and Nanoscale Patterns by Replica Molding from Diatom Biosilica.* Advanced Functional Materials, 2007. **17**(14): p. 2439-2446.

47. Kusari, U., et al., *Formation of nanostructured, nanocrystalline boron nitride microparticles with diatom-derived 3-D shapes.* Chemical Communications, 2007(11): p. 1177-1179.

48. Fang, Y., et al., *Protein-mediated layer-by-layer syntheses of freestanding microscale titania structures with biologically assembled 3-D morphologies.* Chemistry of Materials, 2009. **21**(24): p. 5704-5710.

49. Dobson, H.E.M., *Survey of Pollen and Pollenkitt Lipids -- Chemical Cues to Flower Visitors?* American Journal of Botany, 1988. **75**(2): p. 170-182.

50. Weatherspoon, M.R., et al., *Thin, Conformal, and Continuous SnO2 Coatings on Three-Dimensional Biosilica Templates through Hydroxy-Group Amplification and Layer-By-Layer Alkoxide Deposition.* Angewandte Chemie International Edition, 2007. **46**(30): p. 5724-5727.

51. Weatherspoon, M.R., et al., *3D Rutile Titania-Based Structures with Morpho Butterfly Wing Scale Morphologies.* Angewandte Chemie International Edition, 2008. **47**(41): p. 7921-7923.

52. Wang, G., et al., *Layer-By-Layer Dendritic Growth of Hyperbranched Thin Films for Surface Sol–Gel Syntheses of Conformal, Functional, Nanocrystalline Oxide Coatings on Complex 3D (Bio)silica Templates.* Advanced Functional Materials, 2009. **19**(17): p. 2768-2776.

53. Vernon, J.P., et al., *3D photoluminescent lanthanide-doped barium titanate structures synthesized by coating and shape-preserving reaction of complex-shaped bioorganic templates.* J. Mater. Chem., 2012. **22**(21): p. 10435-10437.

54. Rhines, F.N., W.A. Johnson, and W.A. Anderson, *Rates of high-temperature oxidation of dilute copper alloys.* AIME TRANS, 1942. **147**: p. 205-221.

55. Domínguez, E., et al., *Pollen sporopollenin: degradation and structural elucidation.* Sexual Plant Reproduction, 1999. **12**(3): p. 171-178.

56. Ichinose, I., H. Senzu, and T. Kunitake, *Stepwise adsorption of metal alkoxides on hydrolyzed surfaces: A surface sol-gel process.* Chemistry Letters, 1996(10): p. 831-832.

57. Ichinose, I., H. Senzu, and T. Kunitake, *A surface sol-gel process of TiO2 and other metal oxide films with molecular precision.* Chemistry of Materials, 1997. **9**(6): p. 1296-1298.

58. Wriedt, H., *The Fe-O (iron-oxygen) system.* Journal of phase equilibria, 1991. **12**(2): p. 170-200.

59. Lin, H., I. Gomez, and J.C. Meredith, *Pollenkitt Wetting Mechanism Enables Species-Specific Tunable Pollen Adhesion.* Langmuir, 2013. **29**(9): p. 3012-3023.

60. Meredith, J.C., et al., *Combinatorial materials science for polymer thin-film dewetting.* Macromolecules, 2000. **33**(26): p. 9747-9756.

61. Israelachvili, J., *Intermolecular and Surface Forces*. 2nd ed: Academic Press: London, 1992.

62. Dunn, A. and L.H. Chong, *Application of the theory of colloid stability to the problem of particle formation in aqueous solutions of vinyl acetate.* British Polymer Journal, 1970. **2**(1): p. 49-59.

63. Visser, J., *On Hamaker constants: A comparison between Hamaker constants and Lifshitz-van der Waals constants.* Advances in Colloid and Interface Science, 1972. **3**(4): p. 331-363.

64. Martinez, N., et al., *Enhanced compositional sensitivity in atomic force microscopy by the excitation of the first two flexural modes.* Applied Physics Letters, 2006. **89**(15): p. 153115-153115-3.

65. Huang, Y., et al., *Mechanisms for nano particle removal in brush scrubber cleaning.* Applied Surface Science, 2011. **257**(7): p. 3055-3062.

66. He, C., et al., *A new purification method for carbon nanotubes and associated atomic force microscope force–distance curve analysis.* Separation and Purification Technology, 2011. **81**(2): p. 174-183.

67. Nussbaumer, R.J., et al., *Polymer-TiO2 Nanocomposites: A Route Towards Visually Transparent Broadband UV Filters and High Refractive Index Materials.* Macromolecular Materials and Engineering, 2003. **288**(1): p. 44-49.

68. Daoust, H. and M. Rinfret, *Solubility of polymethyl methacrylate and polyvinyl acetate.* Journal of Colloid Science, 1952. **7**(1): p. 11-19.

69. Devi, C.U., A. Sharma, and V. Rao, *Electrical and optical properties of pure and silver nitrate-doped polyvinyl alcohol films.* Materials Letters, 2002. **56**(3): p. 167-174.

70. Chiu, M.-H., J.-Y. Lee, and D.-C. Su, *Complex refractive-index measurement based on Fresnel's equations and the uses of heterodyne interferometry.* Applied optics, 1999. **38**(19): p. 4047-4052.

71. Rosenholtz, J.L. and D.T. Smith, *The dielectric constant of mineral powders.* 1936. **21**: p. 115.

72. Atkin, S.L., et al., *UV and visible light screening by individual sporopollenin exines derived from Lycopodium clavatum (club moss) and Ambrosia trifida (giant ragweed).* Journal of Photochemistry and Photobiology B: Biology, 2011. **102**(3): p. 209-217.

73. Lide, D.R.e., *CRC Handbook of Chemistry and Physics*. Internet Version 2005, http://www.hbcpnetbase.com2005: CRC Press, Boca Raton, FL, 2005.

74. Leventis, N. and X. Gao, *Magnetohydrodynamic electrochemistry in the field of Nd-Fe-B magnets. Theory, experiment, and application in self-powered flow delivery systems.* Analytical Chemistry, 2001. **73**(16): p. 3981-3992.

CHAPTER 5

TUNING THE LONG-RANGE MAGNETIC FORCE OF THREE-DIMENSIONAL MAGNETIC POLLEN REPLICAS

5.1 Overview

The tunability of magnetic attractive forces in microparticle design is a key component in magnetophoretic separations, targeted drug delivery, biological cell manipulation, microfluidics, and the self-assembly of hierarchical structures [1-6]. Additionally, coupling long-range magnetic attractions with controlled short-range van der Waals (VDW) adhesion may present new avenues for microparticle research. In Chapter 4, we reported the first synthesis of ferro- and ferri-magnetic pollen replicas from native sunflower (*Helianthus annuus*) pollen bio-organic templates using 30 coating cycles in the layer-by-layer (LbL) surface sol-gel (SSG) process. The replicas maintained the morphology of the native pollen creating complex, hollow, three-dimensional (3-D) structures. Native, hematite (α-Fe_2O_3), and magnetite (Fe_3O_4) sunflower pollen exhibited short-range VDW adhesion that was dependent on spike tip radius for native pollen and crystallite size for α-Fe_2O_3, and Fe_3O_4 replicas. Fe_3O_4 replicas were found to possess an additional long-range magnetic attraction to a permanent magnet.

In this chapter, we expand the study to include 10, 20, 30, 40, and 50 precursor deposition cycles on sunflower pollen bio-organic templates during the LbL SSG process. Modifying the number of deposition cycles is a potential design tool for tuning the short-range adhesion and long-range magnetic attraction of pollen replicas. Additionally, varying the coating layers allows for evaluating pollen replicas' capability to preserve the size and shape of natural pollen features. Upon conversion to α-Fe_2O_3 the Fe_3O_4 replicas, the short-range VDW-based adhesion of these replicas did not significantly change with coating layers. The contact radii of α-Fe_2O_3 the Fe_3O_4 replicas were calculated using the

Hamaker model and the results showed that the contact radii of these replicas did not significantly change with coating layers. Long-range magnetic forces were probed using an axially-poled disk magnet. Simulations of the disk magnet's magnetic field, validated using a chromium dioxide-coated polystyrene (CrO_2-PS) microsphere standard, allowed for the theoretical modeling of the magnetic attractions of Fe_3O_4 replicas (10-50 coating layers). Fe_3O_4 replica magnetic attractive forces agreed well with theory and significantly increased with the number of coating layers.

5.2 Theory

An axially-poled, permanent disk magnet can be used to probe the magnetic force of attraction experienced by α-Fe_2O_3 and Fe_3O_4 sunflower replicas. Starting with Gauss' law for magnetism from Maxwell's equations for macroscopic magnetism, the magnetic induction (B) of a magnetic dipole over a closed surface is given in Eq. (5.1) [7]:

$$\nabla B = 0 \tag{5.1}$$

Within the permanent magnet, B is also related to the magnetic field (H) and magnetization (M) by Eq. (5.2)

$$B = \mu_o(H + M) \tag{5.2}$$

where μ_o (4π x 10^{-7} N A^{-2}) is the permeability of free space [8]. Outside the magnet, however, M is zero and B is reduced to Eq. (5.3)

$$B = \mu_o H \tag{5.3}$$

Therefore, B is proportional to H and mapping H is equivalent to mapping B [9]. The force of a magnetic particle (F_m) interacting with a permanent magnet possessing a field gradient is governed by Eq. (5.4)

$$F_m = (m \cdot \nabla)B \tag{5.4}$$

where m is the magnetic moment [10, 11]. The total moment on the particle can then be expanded in Eq. (5.5)

$$m = V_m M \tag{5.5}$$

where V_m is the volumetric magnetization and M is the magnetization. Substituting Eq. (5.3) and Eq. (5.5) into Eq. (5.4) gives an expanded expression for F_m in Eq. (5.6)

$$F_m = \mu_o V_m M \nabla H \tag{5.6}$$

Because the sunflower replicas are anchored to tipless cantilevers, the direction of particle motion is restricted to the direction of cantilever deflection. Therefore, the force of a magnetic particle interacting with a permanent magnet possessing a field gradient is governed by Eq. (5.7)

$$F_m = \mu_o V_m M \frac{\partial H}{\partial z} \hat{z} \tag{5.7}$$

where $\frac{\partial H}{\partial z}$ is the gradient of the permanent magnet's magnetic field in the z-direction and $\hat{z}$ is the unit vector parallel to the cantilever deflection direction. In order to determine the magnetic force in Eq. (5.7), $\frac{\partial H}{\partial z}$ must be evaluated.

Beginning with Ampere's Law from Maxwell's equations for macroscopic magnetism, the curl of H is governed by Eq. (5.8)

$$\nabla \times H = J_f + \frac{\partial D}{\partial t} \tag{5.8}$$

where J_f is the free current density, D is the electric displacement field, and t is time [7]. In the absence of a current, Eq. (5.8) reduces to Eq. (5.9) and allows us to define a scalar potential function for H in Eq. (5.10) [7].

$$\nabla \times H = 0 \tag{5.9}$$

$$H = -\nabla\Phi \tag{5.10}$$

Taking the divergence of Eq. (5.2) and substituting Eq. (5.1), the divergence of H is shown in Eq. (5.11)

$$\nabla H = -\nabla M \tag{5.11}$$

Taking the divergence of Eq. (5.10) and substituting Eq. (5.11), the Laplacian of the magnetostatic potential is given in Eq. (5.12)

$$\nabla^2\Phi = \nabla M \tag{5.12}$$

Since M is zero outside of the permanent magnet, Eq. (5.12) reduces to Eq. (5.13)

$$\nabla^2\Phi = \frac{1}{r}\frac{\partial}{\partial r}\left(r\frac{\partial\Phi}{\partial r}\right) + \frac{1}{r^2}\frac{\partial^2\Phi}{\partial\theta^2} + \frac{\partial^2\Phi}{\partial z^2} = 0 \tag{5.13}$$

Assuming a uniform magnetization in the z-direction and cylindrical coordinates, Φ is independent of angle because of symmetry and Eq. (5.13) reduces to Eq. (5.14)

$$\frac{\partial^2\Phi}{\partial r^2} + \frac{1}{r}\frac{\partial\Phi}{\partial r} + \frac{\partial^2\Phi}{\partial z^2} = 0 \tag{5.14}$$

Evaluating Φ by Eq. (5.14) allows for the evaluation of H by Eq. (5.10) around the disk magnet. Furthermore, $\frac{\partial H}{\partial z}$ can then be calculated and, using Eq. (5.7), F_m can be determined for a magnetic particle interacting with a permanent disk magnet.

5.3 Experimental

5.3.1 Materials and Procedure

5.3.1.1 Pollen Preparation

The native pollen cleaning process was conducted following the procedure described in Chapter 4.

5.3.1.2 Computer-automated LbL SSG Deposition

The LbL coating process was followed using the procedure described in Chapter 4. In Chapter 4, the coating process was repeated for a total of 30 cycles to build up an Fe-O-bearing coating. In this chapter, Fe-O-bearing coatings are applied to cleaned pollen in 10, 20, 30, 40, and 50 cycles.

5.3.1.3 Thermal Processing

The heat treatments applied to coated pollen particles in Chapter 4 were employed to convert coated pollen particles of 10, 20, 30, 40, and 50 coating layers into hematite and magnetite replicas.

5.3.2 Experimental Methods

5.3.2.1 Pollen and Pollen Replica Characterization

Scanning electron microscopy was conducted with a field emission gun instrument (Carl Zeiss SMT, Ltd., Thornwood, NY USA) equipped with an energy dispersive X-ray spectrometer (INCA EDS, Oxford Instruments, Abingdon, Oxfordshire UK). The average spine tip radii of oxide replicas of sunflower pollen particles (10-50 coating layers), were obtained from SEM images of particles attached to cantilever probes (described in Chapter 4). Thermogravimetric (TG) analysis was used to evaluate the mass of replica oxide coatings (10-50 layers) relative to the mass of native organic pollen. TGA runs were carried out in a temperature range of 30-600 °C, in air and with a constant heating rate of 50 °C min^{-1} for all experiments. The sample mass was ~ 0.5 g for all measurements.

5.3.2.2 Magnetic Property Characterization

DC magnetic hysteresis loop measurements of α-Fe_2O_3 and Fe_3O_4 replicas were performed on a Quantum Design MPMS-XL7 Superconducting Quantum Interference Device (SQUID). The samples were mounted onto axially symmetric polyimide strips and adhered with a negligible amount of silicone adhesive. The hysteresis loops were measured in applied fields between -7 and +7 tesla and a temperature of 300 K.

5.3.2.3 Substrate Preparation and Characterization

The substrate preparation and characterization methods from Chapter 4 were utilized.

5.3.2.4 Adhesion Measurements

Adhesion measurements were conducted using colloidal probes consisting of a single oxide replica particle attached to a tipless silicon atomic force microscope (AFM) cantilever (FORT-TL, Applied NanoStructures, Inc.) using a procedure described in Chapter 2. For each type replica particle (α-Fe_2O_3 or Fe_3O_4 replicas with 10-50 coating layers), three single-particle-bearing cantilever probes were prepared (for a total of 30 particle/cantilever probes). Adhesion force measurements were evaluated with a scanning probe microscope (Dimension 3100 SPM equipped with a Nanoscope V Controller, Veeco Instruments, Inc., Plainview, NY USA) operated in contact mode. The spring constants, as determined with the scanning probe microscope, of the sunflower pollen-bearing, α-Fe_2O_3 replica-bearing, and Fe_3O_4 replica-bearing cantilever probes fell in the ranges listed in Table 5.1. Adhesion measurements for cleaned sunflower pollen (from Chapter 4) are also included for comparison. Additionally, t-tests were performed to determine the overall statistical significance ($\alpha = 0.05$) of the change in calculated contact radii with the number of coating layers.

Table 5.1. Range of cantilever probe spring constants (N/m) used in this study.

Coatings	0	10	20	30	40	50
Cleaned	1.84-2.34	--	--	--	--	--
α-Fe_2O_3	--	1.44-2.26	1.08-1.66	1.19-1.91	0.81-1.53	1.60-3.10
Fe_3O_4	--	1.92-2.30	1.15-2.05	1.63-1.69	0.91-1.67	1.37-1.61

5.3.2.5 Magnetic Force Measurements

The magnetic force of an individual oxide replica particle was probed with an axially-poled, neodymium-iron-boron alloy permanent magnet disk (ND022N-35, 5 mm

diameter, 1.5 mm thick, Master Magnetics, Inc., Castle Rock, CO USA) onto which was attached a polished nickel foil (Ni-Nd). The Ni-Nd disk magnet possessed a residual induction of 12,300 G. For each particular particle/cantilever probe and Ni-Nd substrate, 20 separate force-distance scans were obtained at the edge of the Ni-Nd magnet (where the gradient of the magnetic field is highest). The difference in the non-contact forces at the surface of the Ni-Nd magnet and at maximum retraction from the Ni-Nd magnet is the magnitude of the magnetic force. Additionally, t-tests were performed to determine the overall statistical significance ($\alpha = 0.05$) of the change in calculated contact radii with the number of coating layers.

Magnetic force-distance curves between an individual oxide replica particle and the Ni-Nd substrate were obtained by recording the change in cantilever deflection relative to the cantilever deflection at maximum retraction upon approaching the edge of the Ni-Nd magnet. As a model standard, magnetic force-distance curves of a 9.6 μm diameter ferromagnetic chromium dioxide-coated polystyrene (CrO_2-PS) microsphere (M_r = 6.3 emu g^{-1}, 20 vol.% CrO_2, Spherotech, Inc., Lake Forest, IL USA) approaching the Ni-Nd disk magnet were measured. The ambient relative humidity in the laboratory during the magnetic force measurements ranged from 30 to 35%.

5.3.2.6 Magnetic Field Simulation

The magnetostatic potential and magnetic field of the Nd permanent magnet was modeled using a finite difference approximation detailed elsewhere [9]. The approximations were coded in FORTRAN77 and numerically evaluated using an NAG Fortran Builder 5.2. The simulation was performed on the Ni-Nd permanent magnet possessing a 1.5 mm diameter and 5 mm thickness using a 50 mm x 50 mm grid and a 50 μm step size. The finite difference approximations, boundary conditions, and FORTRAN77 code, adapted from reference 9, are detailed in Appendix A.

5.4 Results and Discussion

5.4.1 Pollen Replica Characterization

Sunflower pollen particles were converted into magnetic oxide replicas via use of a computer-automated LbL SSG coating process, detailed in Chapter 4. SEM images of sunflower pollen particles after exposure to 10-50 SSG deposition cycles are shown in Figures 5.1A1-A5. The sunflower pollen grains were roughly spherical in shape and possessed echini (spines) of relatively high aspect ratio (height:width-at-midheight ratio of ~5:1). The Fe-O-coated sunflower pollen grains were then converted into hematite and magnetite using the procedure described in Chapter 4. Although smaller than the starting, Fe-O-coated pollen particles, hematite and magnetite replicas (Figures 5.1B1-B5 and Figures 5.1C1-C5, respectively) retained the 3-D shapes and surface features of the starting pollen grains. Table 5.2 details the diameters of Fe-O-coated-sunflower, α-Fe_2O_3, and Fe_3O_4 replicas during the conversion process. Though there is some variation in the size of native pollen grains (~28-43 μm), the relative diameters after conversion from Fe-O to α-Fe_2O_3 and Fe_3O_4 replicas increased with coating layers. In addition, no detectable change in replica particle size, for each coating layer, was detected upon conversion of the hematite into magnetite.

Table 5.2. Measured diameters of coated sunflower, α-Fe_2O_3 replicas, and Fe_3O_4 replicas of varying SSG deposition cycles (10-50 layers).

Coatings	Fe-O (D, μm)	α-Fe_2O_3 (D, μm)	Fe_3O_4 (D, μm)	$D_{\alpha\text{-}Fe2O3}/D_{Fe\text{-}O}$	$D_{Fe3O4}/D_{Fe\text{-}O}$	$D_{Fe3O4}/D_{\alpha\text{-}Fe2O3}$
10	27.9	13.3	13.2	0.48	0.47	0.99
20	31.5	17.5	17.5	0.56	0.56	1.0
30	42.9	26.5	26.4	0.62	0.62	1.0
40	30.5	20	20	0.66	0.66	1.0
50	33.8	23.5	23.2	0.70	0.69	0.99

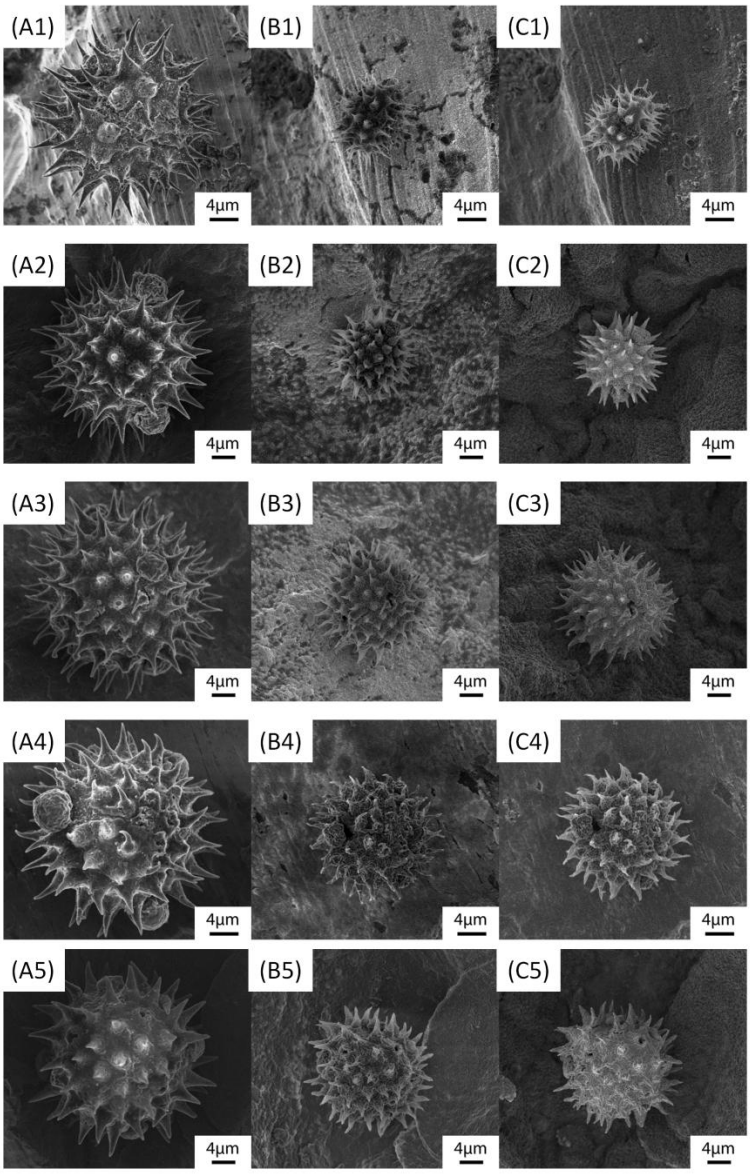

Figure 5.1. SEM images of sunflower pollen particles at various stages of conversion into Fe_3O_4: A) Fe-O-coated grains after 10-50 SSG deposition cycles, B) α-Fe_2O_3 replicas of the same grain in A) after pyrolysis at 600 ^{0}C for 4 h in air, and C) Fe_3O_4 replicas of the same α-Fe_2O_3 grain in B) generated by partial reduction using a Rhines pack (Fe/Fe_3O_4) at 550 ^{0}C for 3 h. Label "1" indicates 10 coating layers, "2" indicates 20 coating layers, "3" indicates 30 coating layers, "4" indicates 40 coating layers, and "5" indicates 50 coating layers.

The coated pollen particles were then heated in air at 600 °C for 4 h to allow for pyrolysis of the pollen template, and crystallization of the oxide coating. TG analysis in Chapter 4 confirmed the complete pyrolysis of the organic material from the sunflower pollen template. Figure 5.2 displays the wt.% of material remaining, from the inorganic oxide coatings, after heating Fe-O-coated sunflower pollen particles to 600 °C. An increasing trend in remaining wt.% is apparent when SSG deposition cycles were increased from 10 to 50.

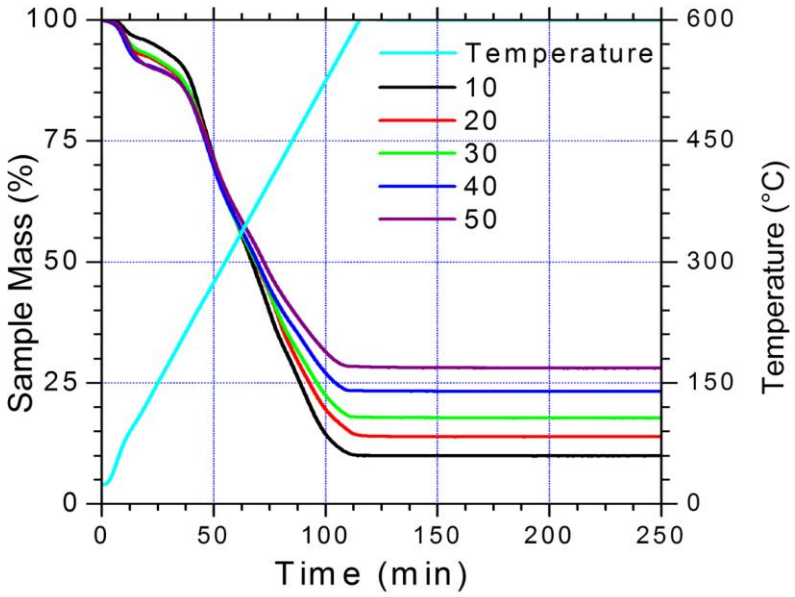

Figure 5.2. TG analysis of Fe-O-coated sunflower pollen (10-50 SSG deposition cycles) during pyrolysis by heating in air at 0.5 ^{0}C min^{-1} to 600 ^{0}C.

The magnetic properties of 50 Layer α-Fe_2O_3 and Fe_3O_4 replicas were examined with a SQUID magnetometer at 300 K as seen in Figure 5.3. The coercivity (H_c, intensity of an external coercive field needed to force the magnetization to zero) and magnetic saturation (M_s, maximum induced magnetization) values for the α-Fe_2O_3 replicas were determined to be 2710.7 Oe and 0.3 emu g^{-1}, respectively. The H_c and M_s values for the Fe_3O_4 replicas were determined at 300 K to be 206.7 Oe and 68.2 emu g^{-1}. This H_c value is higher than that of bulk Fe_3O_4 (115-150 Oe) and that of 150 nm Fe_3O_4 nanoparticles

(56.5 Oe) [12].The M_s value for the Fe_3O_4 replica is lower than the bulk value (92 emu g^{-1}) [13]. In general the M_s value is lower than that of the bulk and deceases with particle size [12, 14]. Even with an M_s value lower than the of bulk magnetite, the value is over two orders of magnitude higher than the α-Fe_2O_3 replicas and allows for magnetic related differences to be detected with adhesion measurements. The remanent magnetization (M_r, induced magnetization remaining after an applied field is removed) value for the α-Fe_2O_3 and Fe_3O_4 replicas was determined to be 0.2 emu g^{-1} and 21.8 emu g^{-1}, respectively. The M value for the Fe_3O_4 replicas, necessary for evaluating F_m in Eq. (5.7), was determined at 3.0x10^5 A m^{-1} (the average magnetic field during a typical magnetic force-distance measurement) to be 62 emu g^{-1}. Because it is well known that the crystal size and magnetic properties of magnetic materials are dependent on crystal growth temperature, the magnetic properties of 50 layer replicas are applicable to replicas with 10, 20, 30, and 40 coating layers prepared at the same temperature [15, 16].

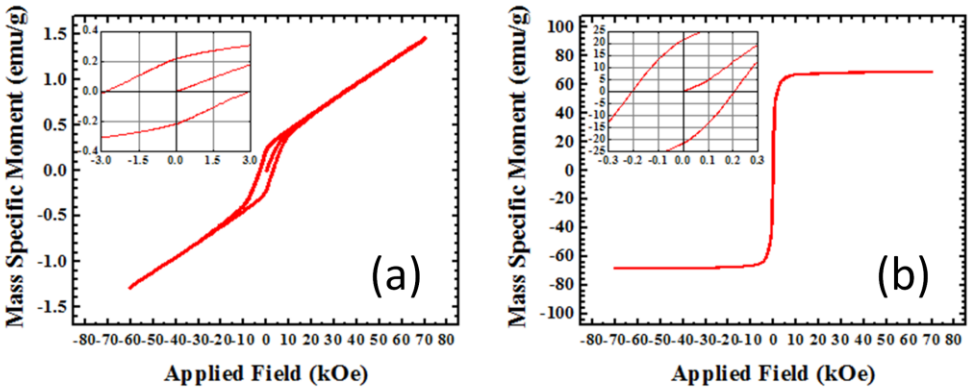

Figure 5.3. Magnetic hysteresis loops at 300 K of a) α-Fe_2O_3 and b) Fe_3O_4 sunflower pollen replicas.

5.4.2 Pollen Replica Adhesion Results

The adhesion strength of cleaned sunflower pollen and oxide pollen replicas of 10-50 coating layers to various substrate surfaces was evaluated by attaching pollen and replica particles to AFM cantilevers (Figure 5.4) as described in the experimental section.

Polyvinyl alcohol (PVA), polyvinyl acetate (PVAc), polystyrene (PS), piranha-etched silicon (Si), unpoled, polished nickel (Ni) foil, and an axially-poled, neodymium-iron-boron alloy disk magnet possessing a polished nickel foil surface (Ni-Nd) were chosen as the substrates to analyze the effects of substrate surface chemistry and magnetic properties on particle attraction. The measured average surface roughness values of the six substrates fell within a range of 0.2 to 2.8 nm.

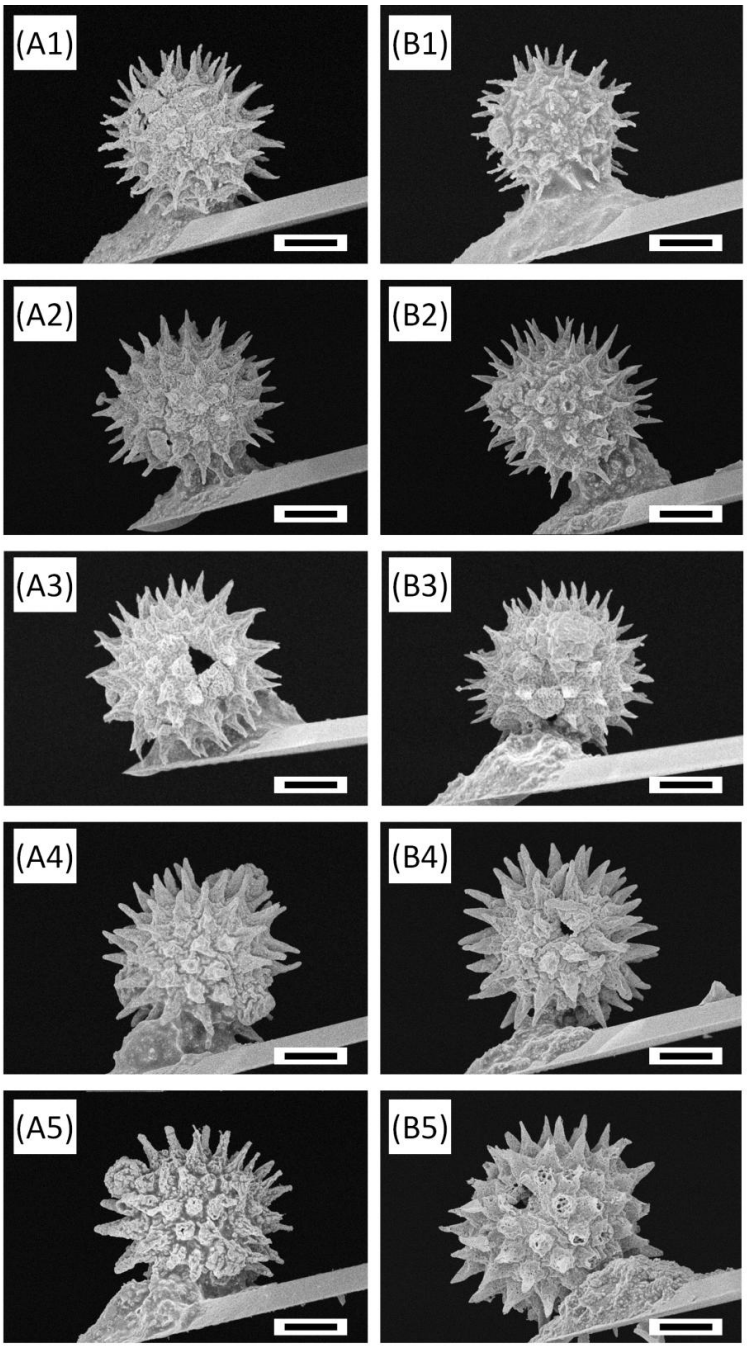

Figure 5.4. Scanning electron images of single-particle-bearing cantilever probes of A) α-Fe_2O_3 sunflower replicas and B) Fe_3O_4 sunflower replicas used in the AFM adhesion study. Label "1" indicates 10 coating layers, "2" indicates 20 coating layers, "3" indicates 30 coating layers, "4" indicates 40 coating layers, and "5" indicates 50 coating layers. The scale bars indicate 5 μm.

Contact mode AFM measurements were used to evaluate the short-range (VDW-based) adhesion of α-Fe_2O_3 and Fe_3O_4 particles of various coating layers (10-50), to the Si, PVA, PVAc, PS, Ni, and Ni-Nd substrates. Average values of the VDW-based adhesion for the different particle and substrate combinations are shown in Figure 5.5 (note: each average value was obtained from 60 measurements consisting of 20 analyses for each of three similar particle/cantilever probes). Given the observed range in measured values, no appreciable difference in contact mode adhesion force was detected for each type of particle on different substrates. Table 5.3 combines the data from all of the substrates for a given type of particle to yield average VDW adhesion force values for cleaned sunflower pollen, α-Fe_2O_3 replicas, and Fe_3O_4 replicas.

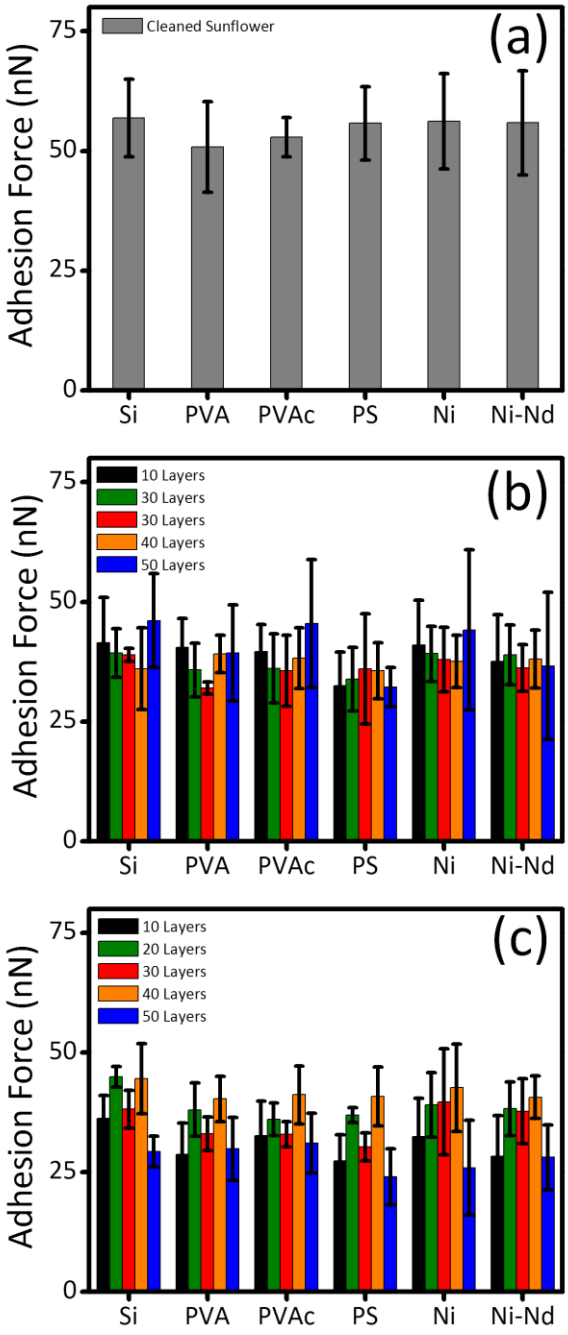

Figure 5.5. AFM adhesion measurements of short-ranged VDW-based adhesion forces for a) cleaned sunflower pollen, b) α-Fe_2O_3 sunflower replicas (10-50 layers), and c) Fe_3O_4 sunflower replicas (10-50 layers) with various substrates. Error bars indicate ± one standard deviation.

Table 5.3. Average adhesion forces for cleaned sunflower, α-Fe_2O_3 sunflower replicas, and Fe_3O_4 sunflower replicas of various coating layers for all substrates investigated. Error indicates ± one standard deviation.

Coatings	0	10	20	30	40	50
Cleaned	55 ± 9	--	--	--	--	--
α-Fe_2O_3	--	39 ± 9	37 ± 6	36 ± 7	38 ± 6	41 ± 13
Fe_3O_4	--	31 ± 8	39 ± 5	34 ± 7	42 ± 7	28 ± 7

Analyses of VDW-based adhesion forces, similar to those in Chapter 4, was conducted using the following Hamaker equation:

$$F_{vdw} = \frac{A_{132}R}{6D^2} \tag{5.15}$$

where A_{132} is the non-retarded Hamaker constant of material 1 and 2 interacting across a medium 3 (air), R is the contact radius, and D is the cutoff separation distance for the VDW interaction (≈0.165 nm) [17]. Because hematite and magnetite are media with high dielectric constants, interactions involving replicas were calculated on the basis of the Lifshitz theory via Eq. (5.16) [17]:

$$A_{132} \approx \frac{3}{4}kT\left(\frac{\varepsilon_1-\varepsilon_3}{\varepsilon_1+\varepsilon_3}\right)\left(\frac{\varepsilon_2-\varepsilon_3}{\varepsilon_2+\varepsilon_3}\right) + \frac{3h\nu_e}{8\sqrt{2}}\frac{\left(n_1^2-n_3^2\right)\left(n_2^2-n_3^2\right)}{\left(n_1^2+n_3^2\right)^{1/2}\left(n_2^2+n_3^2\right)^{1/2}\left\{\left(n_1^2+n_3^2\right)^{1/2}+\left(n_2^2+n_3^2\right)^{1/2}\right\}} \tag{5.16}$$

where k is Boltzmann's constant, T is temperature, h is Planck's constant, ν_e is the media absorption frequency, ε_1 and ε_2 are dielectric constants, and n_1 and n_2 are refractive indices. A_{132} values for various coating layers of hematite or magnetite replicas on all substrates were calculated from Eq. (5.16) by using appropriate ε_1, ε_2, n_1, and n_2 values from Chapter 4, with the assumption that the absorption frequencies of all media are the same. Assuming a flat substrate, R in Eq. (5.15) refers to the contact radius of the spine tip from each probe particle. By inserting the measured average values of adhesion force

into Eq. (5.15) along with the calculated A_{132} constants, average values of contact radii for the α-Fe_2O_3 replicas, and Fe_3O_4 replicas with the various substrates were calculated (Figure 5.6a) and ranged from 94-120 nm and 87-104 nm, respectively. However, the calculated contact radii for all hematite and magnetite replica particles were much smaller than the average spine tip radii of these replicas (i.e., 27-30 nm and 23-31 nm for hematite and magnetite, respectively) obtained from SEM analyses (Figure 5.6b). Instead, the calculated contact radii for oxide replicas of all coating layers were not far from the average crystallite radii (17-18 nm) of these particles obtained from XRD analyses; that is, the VDW-based adhesion forces of the oxide pollen replicas were consistent with the contact of one or two nanocrystals located at the spine tips to the substrates. Additionally, the change in calculated contact radii of the α-Fe_2O_3 and Fe_3O_4 replicas with the number of coating layers was not significant (α = 0.05).

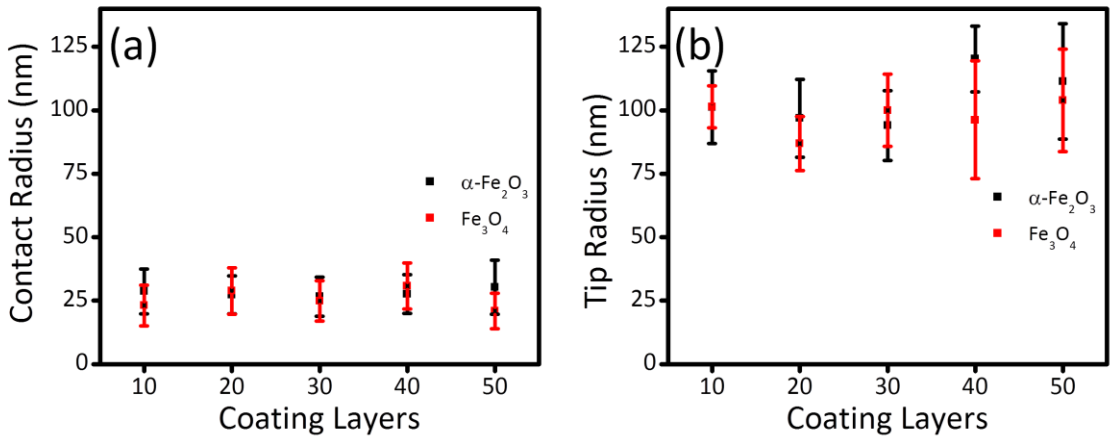

Figure 5.6. Average α-Fe_2O_3 and Fe_3O_4 sunflower replica (10-50 layers) a) calculated contact radii from the Hamaker model and b) measured contact radii from SEM images. Error bars indicate ± one standard deviation.

5.4.3 Modeling of the Magnetic Forces

Using a previously described methodology, the space around the Ni-Nd permanent magnet was discretized and Φ and H were simulated using the appropriate approximations of Eq. (5.14) and corresponding boundary conditions, detailed in

Appendix A [9]. Figure 5.7 shows the simulations of Φ and H around the Ni-Nd permanent magnet. Computing H around the permanent magnet now allows for the calculation of $\frac{\partial H}{\partial z}$ at the outer edge of the magnet, where the highest gradient of the magnetic field is located. At this location, the magnetic force is experimentally measured using colloidal AFM and predicted using Eq. (5.7).

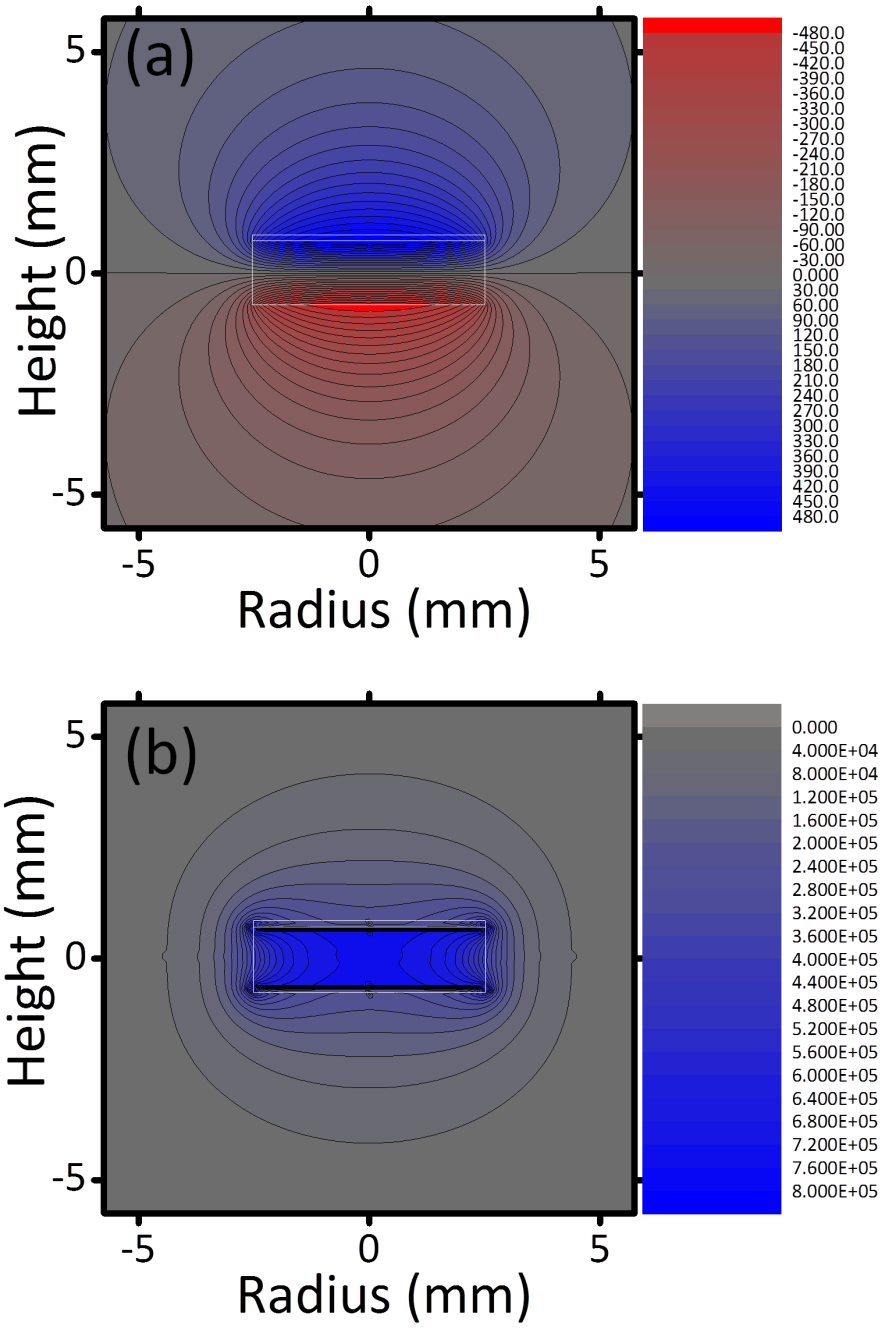

Figure 5.7. Simulations of a) the magnetostatic potential (Φ, A) and b) magnetic field (H, A m^{-1}) around a cross-section of the Ni-Nd permanent disk magnet. The dimensions of the Nd magnet and polished Ni foil are highlighted in white.

The validity of the magnetic force model developed in Eq. (5.7) between a magnetic particle and an axially magnetized disk magnet was assessed by probing the

magnetic attractions of a CrO_2-PS microsphere standard and the Ni-Nd disk magnet. The average magnetization of the CrO_2-PS standard over the distances probed (average magnetic field = 3.0×10^5 A m^{-1}) was ~12 emu g^{-1}. The magnetic forces were measured at the outer edge of the Ni-Nd disk magnet, where $\frac{\partial H}{\partial z}$ is greatest. Because $\frac{\partial H}{\partial z}$ has been evaluated and the CrO_2-PS microsphere possesses a known M and V_m, the calculation of F_m is possible by Eq. (5.7). Figure 5.8a compares the magnetic force values obtained from theoretical calculations and the magnetic force values obtained from experimental measurements of the CrO_2-PS microsphere (Figure 5.8b). The theoretical magnetic force values are in agreement with the measured magnetic force values within an average residual error of 20%. This error is within the error associated with measuring pollen replica magnetic forces, therefore, the magnetic force model is deemed valid.

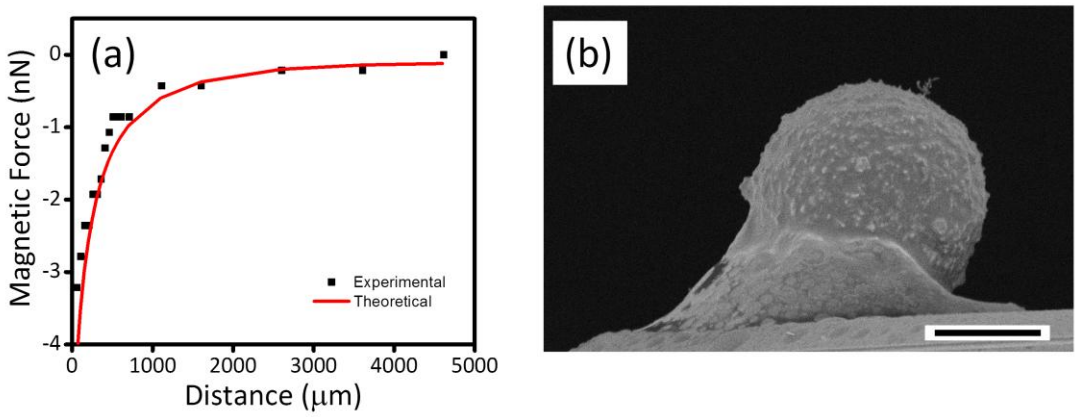

Figure 5.8. Comparison of a) magnetic force values field values obtained from theoretical calculations and experimental measurements of a b) CrO_2-PS microsphere. Scale bar represents 5 µm.

5.4.4 Fe_3O_4 Replica Magnetic Force Results

As discussed in Chapter 4, a noticeable attractive force was detected between the ferrimagnetic 30 layer Fe_3O_4 sunflower pollen replicas and the disk-shaped Ni-Nd substrate at locations near the outer perimeter of the Ni-Nd substrate, where the gradient of the magnetic field intensity associated with the magnetized Ni-Nd substrate is highest

(Figure 5.7b). The average magnetization (*M*) of the magnetite replicas over the distances probed (average magnetic field = 3.0×10^5 A m^{-1}) was 62 emu g^{-1}. Additionally, no appreciable magnetic attraction was detected between the weakly ferromagnetic 30 layer α-Fe_2O_3 sunflower replicas (M = 0.4 emu g^{-1}), or the non-magnetic native sunflower pollen, at any location across the Ni-Nd. Average values of the magnetic attraction for the different Fe_3O_4 particle coatings (10-50 layers) with the Ni-Nd permanent magnet are shown in Figure 5.9 (note: each average value was obtained from 60 measurements consisting of 20 analyses for each of three similar particle/cantilever probes). The magnetic force of the various Fe_3O_4 replicas was obtained at the outer edge of the Ni-Nd where the gradient of the magnetic field intensity associated with the magnetized Ni-Nd substrate is highest.

From TG analysis in Figure 5.2 it is apparent that increasing the number of SSG coating layers increases the wt.% of inorganic oxide material remaining after pyrolysis of the organic pollen template. Figure 5.9 indicates that there is a linear relationship with remaining inorganic wt.% remaining after pyrolysis and the number of coating layers deposited. From Eq. (5.7), we see that the magnetic force of a particle with a constant remanent magnetization interacting with a given magnetic field should increase linearly with increasing particle magnetic volume. As expected, the magnetic forces of Fe_3O_4 replicas (Figure 5.9) do increase linearly with increasing coating layers and further support the model developed. Additionally, the differences in the measured magnetic forces of Fe_3O_4 replicas for each coating layer was determined to be significant (α = 0.05). Control over the magnetic volume deposited during the LbL SSG process, therefore, provides a means for tuning the magnetic attractive forces experienced by these magnetic pollen replicas.

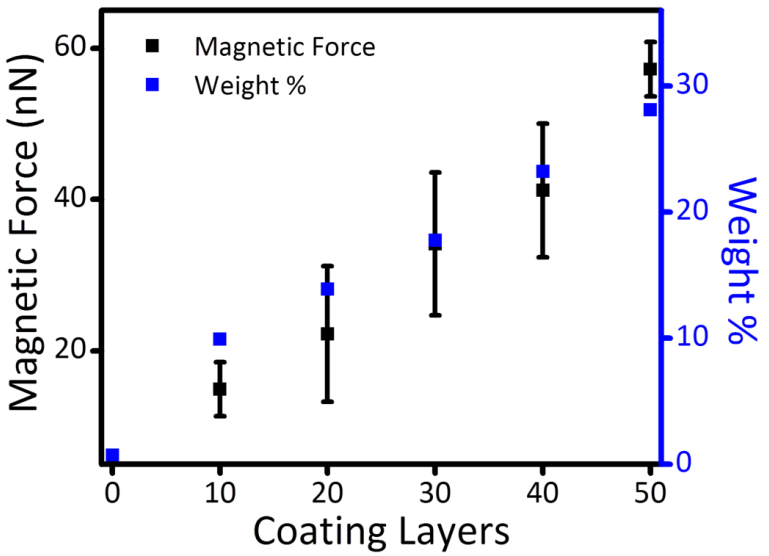

Figure 5.9. Magnetic force measurements of Fe_3O_4 sunflower replicas of 10-50 coating layers along with the corresponding remaining weight % of oxide material after pyrolysis of the organic pollen template.

5.4.5 Modeling the Magnetic Force of Fe_3O_4 Replicas

The total adhesion force acting between a given Fe_3O_4 replica particle and the Ni-Nd substrate is plotted against probe distance from the substrate surface in Figure 5.10a (note: measurements were obtained at a lateral distance of ~300 µm from the Ni foil edge). Both magnetic and VDW attractive forces were detected between Fe_3O_4 sunflower pollen replicas of all coatings and the Ni-Nd magnet near the outer edge of this substrate. For each Fe_3O_4 particle/Ni-Nd-edge substrate pairing, the total adhesion force (~50-90 nN) acting over a short distance (~10 nm) consisted of the sum of the VDW force (~35 nN) and the magnetic force (~15-55 nN). At distances just beyond the range of VDW-based adhesion, a steady magnetic force was detected. The magnetic interaction between the Fe_3O_4 sunflower pollen replicas and the magnetized edge of the Ni-Nd substrate persisted out to a separation distance of ~1 mm.

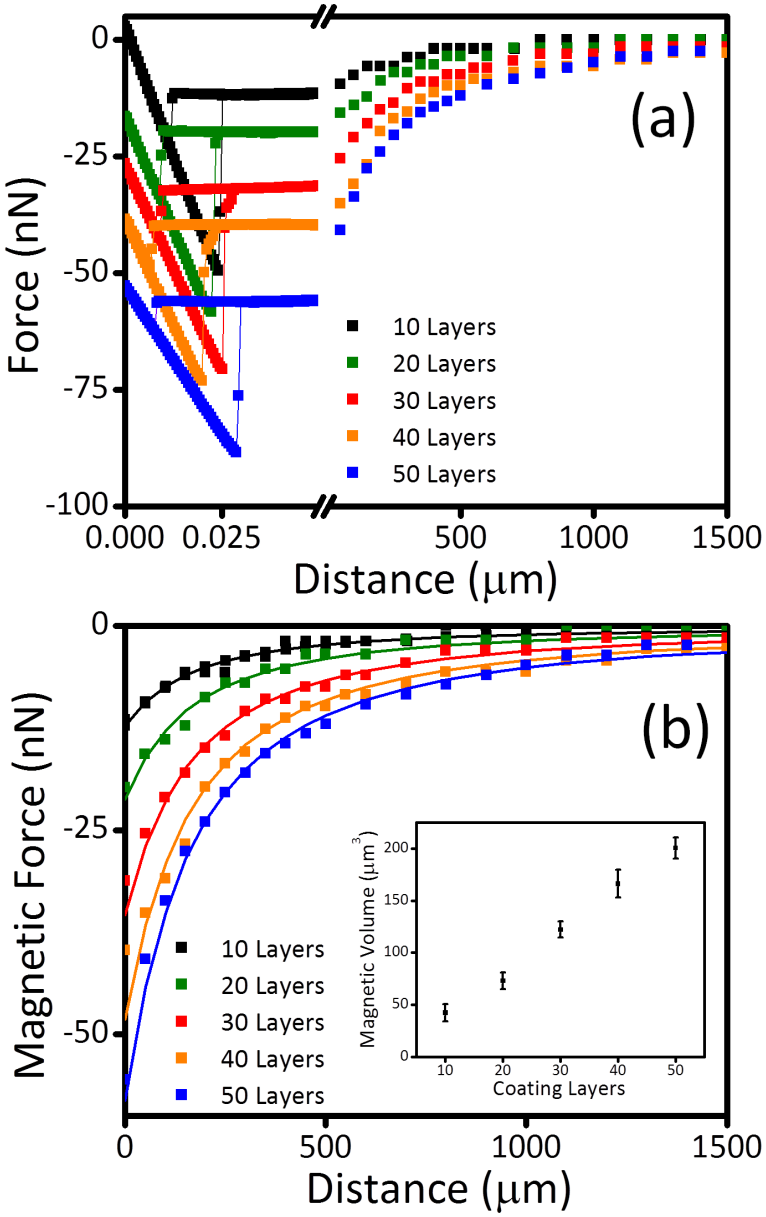

Figure 5.10. **AFM force-distance curves of the total (VDW + magnetic) adhesion force for a) Fe_3O_4 sunflower replicas with 10-50 coating layers at the edge of the disk-shaped Ni-Nd magnet and b) a comparison of the experimental magnetic force-distance curves with theoretical force-distance curves (the data in the inset is the calculated magnetic volume of Fe_3O_4 replicas of 10-50 coating layers).**

In order to implement the magnetic force model developed in Eq. (5.7), the magnetic volumes of Fe_3O_4 replicas of all coating layers is needed. These magnetic volumes were calculated from Eq. (5.7) using the experimental magnetic forces at each

position above the Ni-Nd magnet, the numerically evaluated $\frac{\partial H}{\partial z}$ at each position above the Ni-Nd magnet, and the Fe_3O_4 replica M. The magnetic volumes used to predict the magnetic forces of Fe_3O_4 replicas of varying coating layers is shown in the inset of Figure 5.10b. Again, a linear relationship is apparent between the calculated magnetic volume and number of SSG coatings. By inserting the calculated magnetic volumes, the numerically evaluated $\frac{\partial H}{\partial z}$ at each position above the Ni-Nd magnet, and the Fe_3O_4 replica M into Eq. (5.7), values of magnetic forces for Fe_3O_4 replicas (10-50 coating layers) at each position above the Ni-Nd disk magnet were calculated. Figure 5.10b compares experimental force-distance curves with theoretical force-distance curves for Fe_3O_4 replicas with 10-50 coating layers. Error associated with comparing theoretical with experimental magnetic forces ranged from 5-13%. Interestingly, the magnetic force model does not account for structural effects and treats the magnetic volume as a shapeless mass of material. Therefore, agreement between experimental and theoretical magnetic forces indicates the complex pollen replica shape does not affect the modeling of magnetic attraction, thus proving its potential for tailoring pollen replica magnetic attraction.

5.5 Conclusions

This work in this chapter demonstrates the ability to control long-range magnetic adhesion and predict the magnetic attractive forces of ferrimagnetic pollen replica particles. Using the LbL SSG process, 10, 20, 30, 40, and 50 deposition cycles were applied to sunflower pollen bio-organic templates. Thermal treatment of these highly conformal Fe-O-coated pollen particles (10-50 layers) allowed for conversion to nanocrystalline, phase-pure ferromagnetic hematite (α-Fe_2O_3) and nanocrystalline, phase-pure ferrimagnetic magnetite (Fe_3O_4) These α-Fe_2O_3 and Fe_3O_4 replicas were found to exhibit short-range VDW-based adhesion independent of coating layers and regulated by the contact radii of nanocrystals on the tips of the replica spines.

Ferrimagnetic Fe_3O_4 replicas also exhibited short-to-long-range (up to 1 mm) magnetic adhesion that scaled with the volume of magnetic material present. The Fe_3O_4 replica magnetic forces experimentally observed agreed with predicted magnetic forces using the model developed within 13% error. Control of the short-range VDW adhesion coupled with the scalability of magnetic forces with nanocrystalline magnetite coating layers present in the ceramic replicas and the predictability of magnetic forces using our magnetic force model demonstrate the potential design tools for synthesizing microparticles with tunable adhesion.

Acknowledgement: We are grateful to Dr. Ken Sandhage and Brandon Goodwin for their contributions to this work. They performed the preparation and characterization of all hematite and magnetite pollen replicas and supplied the data in Figures 5.1, Figure 5.2, and Table 5.2. We are also appreciative of the magnetic hysteresis loops in Figure 5.3 provided by Tom Ekiert and Brandon Yocum of the Air Force Research Laboratory.

5.6 References

1. Nandy, K., et al., Analytical model for the magnetophoretic capture of magnetic microspheres in microfluidic devices. Journal of magnetism and magnetic materials, 2008. 320(7): p. 1398-1405.

2. Rudge, S., et al., Adsorption and desorption of chemotherapeutic drugs from a magnetically targeted carrier (MTC). Journal of Controlled Release, 2001. 74(1–3): p. 335-340.

3. Henighan, T., et al., Manipulation of Magnetically Labeled and Unlabeled Cells with Mobile Magnetic Traps. Biophysical Journal, 2010. 98(3): p. 412-417.

4. Rida, A. and M.A.M. Gijs, Manipulation of Self-Assembled Structures of Magnetic Beads for Microfluidic Mixing and Assaying. Analytical Chemistry, 2004. 76(21): p. 6239-6246.

5. Love, J.C., et al., Three-dimensional self-assembly of metallic rods with submicron diameters using magnetic interactions. Journal of the American Chemical Society, 2003. 125(42): p. 12696-12697.

6. Wen, W., et al., Two-and three-dimensional arrays of magnetic microspheres. Journal of materials research, 1999. 14(4): p. 1186-1189.

7. Nayfeh, M.H. and M.K. Brussel, Electricity and magnetism1985, New York: Wiley. xiv, 619 p.

8. Pugh, E.M. and E.W. Pugh, Principles of electricity and magnetism. Addison-Wesley series in physics1960, Reading, Mass.,: Addison-Wesley Pub. Co. 430 p.

9. Leventis, N. and X. Gao, Magnetohydrodynamic electrochemistry in the field of Nd-Fe-B magnets. Theory, experiment, and application in self-powered flow delivery systems. Analytical Chemistry, 2001. 73(16): p. 3981-3992.

10. Scott, W.T., The physics of electricity and magnetism. 2d ed1977, Huntington, N.Y.: R. E. Krieger Pub. Co. xvii, 703 p.

11. Pankhurst, Q.A., et al., Applications of magnetic nanoparticles in biomedicine. Journal of physics D: Applied physics, 2003. 36(13): p. R167.

12. Goya, G., et al., Static and dynamic magnetic properties of spherical magnetite nanoparticles. Journal of Applied Physics, 2003. 94: p. 3520.

13. Skomski, R., Nanomagnetics. Journal of Physics: Condensed Matter, 2003. 15(20): p. R841.

14. Morales, M., et al., Structural effects on the magnetic properties of γ-Fe2O3 nanoparticles. Journal of magnetism and magnetic materials, 1999. 203(1): p. 146-148.

15. Fang, M., et al., Particle size and magnetic properties dependence on growth temperature for rapid mixed co-precipitated magnetite nanoparticles. Nanotechnology, 2012. 23(14): p. 145601.

16. Qiao, S., et al., Growth temperature dependent structural and magnetic properties of epitaxial Co 2 FeAl Heusler alloy films. Journal of Applied Physics, 2013. 113(23): p. 233914-233914-4.

17. Israelachvili, J., Intermolecular and Surface Forces. 2nd ed: Academic Press: London, 1992.

CHAPTER 6

CONCLUSIONS AND RECOMMENDATIONS

6.1 Summary and Conclusions

This work provides a foundation for exploiting the breadth of nano- and micro-structured pollen morphologies for multimodal adhesion. The results demonstrate the successful completion of the specific objectives outlined in Chapter 1. The key findings for each objective are summarized as follows:

6.1.1 Quantify the dependence of pollen adhesion on exine size and shape using colloidal AFM

We successfully quantified the adhesion of olive (*Olea europaea*), poplar (*Populus nigra*), ragweed (*Ambrosia artemisiifolia*), dandelion (*Taraxacum officinale*), and sunflower (*Helianthus annuus*) pollen with a series of test surfaces representing unique combinations of solid surface morphologies using AFM. It was determined that the surface morphology (size and shape of echinate or reticulate features) provides pollens with a mechanism for tuning adhesion over a force range of ~30-60 nN. Pollen grains, in the absence of the viscous pollenkitt coating, had adhesion strengths that were independent of surface chemistry and scalable with the tip radius of the pollen's ornamentation features, according to the Hamaker model. The structural adhesion mechanisms observed for natural pollen adhesion enabled the design of novel synthetic microparticle adhesion strategies.

6.1.2 Control the deposition of nanoparticles onto pollen using electrostatic interactions to modify pollen's adhesive properties and impart optical functionality

We successfully performed the first ex-situ deposition of metal nanoparticles (NPs) onto isolated pollen shells. Ragweed pollen shells were isolated using a conventional treatment with basic and acidic solutions. Functionalizing the isolated,

hydroxyl-rich sporopollenin shells with an aminosilane imparted a positive surface charge, which allowed heteroaggregation with negatively charged gold (Au) NPs and silver (Ag) nanocubes (NCs). Metal NP surface coverage up to 55% was achieved and could be tuned depending on the metal NP concentration or pH environment. Cleaned, base/acid-treated, and amine-functionalized ragweed pollens exhibited short-range VDW-based adhesion dependent on the contact with a single spine tip. The bio-organic ragweed pollen core possessed well-defined spine protuberances. AgNC-coated ragweed pollen exhibited short-range VDW-based adhesion dependent on the contact with a single spine tip. AuNP-covered spine tips of AuNP-coated ragweed pollen displayed enhanced adhesion (nearly double) compared to uncoated pollen spine tips of AgNC-coated pollen. Multiple nanoparticle contacts as well as an increased Hamaker constant facilitated the increase in short-range VDW adhesion. Additionally, NP-pollen composites showed potential for use as SERS substrates capable of enhancing the Raman signal of molecules bound to the NP surface. The approach developed in this chapter provides a framework for utilizing bio-organic pollen-NP composite particles for enhanced adhesion and as SERS substrates by tailoring the pollen morphology, NP size, and NP chemistry.

6.1.3 Utilize pollen as a template in the surface sol-gel fabrication of replicas possessing magnetic behavior

We demonstrated, for the first time, the ability to generate high-fidelity, all-oxide replicas of sunflower pollen particles exhibiting tailorable short-range VDW adhesion and short-to-long-range magnetic attraction. The hydroxyl-rich nature of sporopollenin allowed for the use of a LbL SSG process to apply highly-conformal Fe-O-bearing coatings (30 cycles) to the sharp, high-aspect-ratio spiny structure of sunflower pollen. Subsequent firing at 600 °C in air yielded high-fidelity replicas comprised of nanocrystalline, phase-pure ferro-magnetic hematite (α-Fe_2O_3). Partial reduction of these hematite replicas, via use of a controlled oxygen partial pressure (Rhines pack-based) heat treatment, yielded nanocrystalline, phase-pure ferrimagnetic magnetite (Fe_3O_4)

replicas. The Fe_3O_4 replicas were found to exhibit short-range (~10 nm) VDW-based adhesion, governed by the contact of oxide nanocrystals present on the sharp spines inherited from the starting sunflower pollen, and short-to-long-range (up to 1 mm) magnetic adhesion governed by the ferrimagnetic magnetite. Using the LbL SSG process to tailor the amount of nanocrystalline magnetite present in the ceramic replicas, microparticles with tunable short-range (VDW-based) and longer-range (magnetic) adhesion were successfully synthesized.

6.1.4 Tune the magnetic attraction of the pollen replicas and model the long-range magnetic interactions of the replicas using a permanent magnet as a probe.

We succeeded in demonstrating the ability to control long-range magnetic attraction and predicting the magnetic attractive forces of ferrimagnetic Fe_3O_4 pollen replica particles. Using a range of LbL SSG deposition cycles (10-50) on the bio-organic sunflower templates followed by thermal treatment, conversion to nanocrystalline, phase-pure ferromagnetic hematite (α-Fe_2O_3) and nanocrystalline, phase-pure ferrimagnetic magnetite (Fe_3O_4) was achieved. These α-Fe_2O_3 and Fe_3O_4 replicas were found to exhibit short-range VDW-based adhesion independent of coating cycles and regulated by the contact radii of nanocrystals on the tips of the replica spines. Ferrimagnetic Fe_3O_4 replicas also exhibited short-to-long-range (up to 1 mm) magnetic adhesion that scaled with the volume of magnetic material present. The experimentally observed Fe_3O_4 replica magnetic forces agreed with predicted magnetic forces according to the model used (within 13% error), which indicated that the magnetic forces were not influenced by the complex replica structure. Control of the short-range VDW adhesion, the scalability of magnetic forces with nanocrystalline magnetite replica coating layers, and the predictability of magnetic forces using the magnetic force model demonstrate the potential design tools for synthesizing microparticles with tunable adhesion.

6.2 Recommendations for Future Work

Based on the findings of this work, a number of key scientific questions have been raised. The following section seeks to provide possible strategies for approaching these issues in future studies.

6.2.1 Investigate the influence of surface roughness on pollen and pollen replica adhesion

AFM force measurements successfully revealed that pollen and pollen replica adhesion is dependent on a single contact point with a flat substrate. Realistically, the surfaces that these particles come into contact with are likely to possess a range of roughnesses not captured by measurements on a flat ideal surface. For example, the complex pollen morphologies enable a lock and key mechanism with certain species of pollen interacting with stigma surfaces during fertilization [1]. Additionally, microparticle dispersions undergo considerable particle-particle collisions that greatly affect their ability to disperse [2]. Therefore, major consideration for future work should incorporate the influence of surface roughness on particle adhesion. Colloidal AFM is an effective tool for studying the interactions between particle-bearing cantilevers and rough surfaces, surfaces that mimic particle morphologies, or surfaces covered with immobilized particles. It is likely that increasing the surface roughness of interacting substrates will increase the number of pollen spine contacts and area of contact with each individual spine. Consequently, this adhesion behavior may require the use of a model that incorporates the effect of surface roughness. Understanding the effects that nonideal surfaces have on particle adhesion would give greater insight on the role microstructures play in particle adhesion.

6.2.2 Investigate the adhesion enhancement of natural pollenkitt coating on synthesized pollen-derived particles

The adhesion mechanisms of pollen-derived particles were successfully elucidated using AFM. These “dry” particles were essentially absent of any liquid

influences. In nature, however, pollen grains are naturally coated with an oily liquid that resides on or within cavities in the exine wall, known as pollenkitt [3]. Pollen dispersal is thought to be facilitated by pollenkitt's ability to keep pollen grains together during transport, promoted by adhesion to animals; pollen germination and fertilization of the ovum are possible because the pollenkitt supports pollen adhesion to the stigma and rehydration [4, 5]. Recently, we showed that the liquid pollenkitt contributes to adhesion through capillary mechanisms that differ significantly from those of pollens that do not contain pollenkitt [6]. The adhesion of pollenkitt-covered pollens exhibited enhanced, substrate dependent adhesion (~3-6 times higher compared to cleaned pollens). As a result, natural pollenkitt can provide a means for imparting an additional mode of adhesion to AuNP-coated pollen, AgNC-coated pollen, α-Fe_2O_3 pollen replicas, and Fe_3O_4 pollen replicas displaying short-range VDW-based adhesion and long-range magnetic attraction. Hence, it would be interesting to determine the effects of surface wettability, asperity shape (NP/nanocrystal), and volume of pollenkitt present on the adhesion of pollen-derived particles. The combination of these wet and dry adhesion mechanisms is potentially a useful approach for controlling pollen-derived particle adhesion.

6.2.3 Optimize nanoparticle-pollen composites for effective SERS substrates

The adhesion behavior of metal NP-coated pollen particles was successfully evaluated using AFM. Although these metal NP-pollen composites did show some Raman enhancement of the PVP capping agent and sporopollenin shell, a more effective SERS demonstration is needed. Characteristics of an effective SERS substrate include the ability to enhance the Raman signals of low concentrations of probe molecules, either adsorbed or bound to the metal surface, and the ability to have surface plasmons in the metal NPs excited by a laser source. In order to prove pollen-NPs are viable SERS substrates, future research should demonstrate the detection of an analyte that can adsorb

or bind to the metal NP surface. For example, organic compounds, such as benzene thiol, can readily bind to metal surfaces via a thiol linkage [7, 8]. A significant increase in the selectivity and decrease in the detection limit of SERS-sensors can be achieved by covering the SERS-active metal substrate with a monolayer of a species that forms specific complexes with the analyte under investigation [9]. Because surface plasmons are excited by an incident laser source, the excitation wavelength must be adapted to the resonance wavelength of the metal surface [10]. This would require a detailed characterization of the optical properties of the metal NP pollen composites followed by a tuning of the optical properties for the specific laser source. The most feasible way to tune the optical properties is to modify the plasmon absorption of SERS substrates by tuning the aspect ratio of Au and Ag nanorods [11]. Although, successful application of metal NP-pollen composites as SERS substrates requires significant optimization of the NP chemistry and NP size, the fabrication methodology we developed provides a means for tailoring the metal NPs to fit the specific application.

6.2.4 Tunability of short-range pollen replica adhesion (crystal size)

The short-range VDW adhesion and long-range magnetic attraction of α-Fe_2O_3 and Fe_3O_4 pollen replicas were successfully measured using AFM. The magnitude of short-range adhesion was independent of substrate chemistry and coating cycles, while the long-range magnetic attraction scaled with coating layers (magnetic volume). It is well known that the crystal size of ceramic materials, such as α-Fe_2O_3 and Fe_3O_4, is determined by its growth temperature [12]. Additionally, there is a direct correlation between the crystal size of ceramic materials and their magnetic properties [13, 14]. Thus, future research regarding magnetic pollen replicas should consider the effect of altering the crystal growth temperature. Modifying the crystal size could potentially provide a route for tuning the short-range VDW-based adhesion of pollen replicas and support the current hypothesis that adhesion is crystal size-dependent. The magnetic force

model used to successfully predict ferrimagnetic Fe_3O_4 magnetic forces is dependent on the external magnetic field interacting with the replicas (from a permanent magnet), the magnetic volume of the replica, and the magnetization of the replica. Controlling the replica magnetization, from a modified crystal size, would facilitate further control over the long-range magnetic attractions. Furthermore, tuning the α-Fe_2O_3 and Fe_3O_4 crystal sizes represents an expansion of the available design tools for controlling pollen replica adhesion.

6.3 References

1. Heslop-Harrison, Y., *Control gates and micro-ecology: the pollen-stigma interaction in perspective.* Annals of Botany, 2000. 85(suppl 1): p. 5-13.

2. Bolio, E.J., J.A. Yasuna, and J.L. Sinclair, *Dilute turbulent gas-solid flow in risers with particle-particle interactions.* AIChE Journal, 1995. 41(6): p. 1375-1388.

3. Knoll, F., *Über Pollenkitt und Bestäubungsart: Ein Beitrag zur experimentellen Blütenökologie.* Zeitschrift für Botanik, 1930. 23: p. 609-675.

4. Pacini, E. and M. Hesse, *Pollenkitt – its composition, forms and functions.* Flora - Morphology, Distribution, Functional Ecology of Plants, 2005. 200(5): p. 399-415.

5. Pacini, E., *Tapetum character states: analytical keys for tapetum types and activities.* Canadian Journal of Botany, 1997. 75(9): p. 1448-1459.

6. Lin, H., I. Gomez, and J.C. Meredith, *Pollenkitt Wetting Mechanism Enables Species-Specific Tunable Pollen Adhesion.* Langmuir, 2013. 29(9): p. 3012-3023.

7. Larsson, J., M. Nolan, and J. Greer, *Interactions between thiol molecular linkers and the Au13 nanoparticle.* The Journal of Physical Chemistry B, 2002. 106(23): p. 5931-5937.

8. Onuegbu, J., et al., *Investigation of chemically modified barium titanate beads as surface-enhanced Raman scattering (SERS) active substrates for the detection of benzene thiol, 1, 2-benzene dithiol, and rhodamine 6G.* Spectrochimica Acta Part A: Molecular and Biomolecular Spectroscopy, 2011. 79(3): p. 456-461.

9. Kudelski, A., *Analytical applications of Raman spectroscopy.* Talanta, 2008. 76(1): p. 1-8.

10. Hering, K., et al., *SERS: a versatile tool in chemical and biochemical diagnostics.* Analytical and Bioanalytical Chemistry, 2008. 390(1): p. 113-124.

11. Orendorff, C.J., et al., *Aspect ratio dependence on surface enhanced Raman scattering using silver and gold nanorod substrates.* Physical Chemistry Chemical Physics, 2006. 8(1): p. 165-170.

12. Sivula, K., et al., *Photoelectrochemical water splitting with mesoporous hematite prepared by a solution-based colloidal approach.* Journal of the American Chemical Society, 2010. 132(21): p. 7436-7444.

13. Fang, M., et al., *Particle size and magnetic properties dependence on growth temperature for rapid mixed co-precipitated magnetite nanoparticles.* Nanotechnology, 2012. 23(14): p. 145601.

14. Dunlop, D.J., *Hysteresis properties of magnetite and their dependence on particle size: A test of pseudo-single-domain remanence models.* Journal of Geophysical Research: Solid Earth (1978–2012), 1986. 91(B9): p. 9569-9584.

APPENDIX A

FORTRAN CODE FOR MAGNETOSTATIC POTENTIAL AND MAGNETIC FIELD OF AN NEODYMIUM DISK PERMANENT MAGNET

A.1 Adaptation of FORTRAN simulation

The space around the Ni-Nd permanent magnet is discretized and the magnetostatic potential (Φ) and magnetic field (H) are simulated in FORTRAN77 using the appropriate finite difference approximations and corresponding boundary conditions from the work of Leventis et al. [1].

```
*     Code written in FORTRAN77
*     This simulation maps the MAGNETOSTATIC POTENTIAL (PHI), the
*    MAGNETIC FIELD |HH|, and the GRADIENT OF THE MAGNETIC FIELD
*     |dHH| of a Permanent Disk-Magnet symmetrically disposed about the origin, which
*     is set at (0,0)
*     Calculations are executed in the first quadrant and because of symmetry both the
*     magnetostatic potential, phi, the magnetic field intensity, H, and the gradient of the
*     magnetic field, dH, are unfolded into the other three quadrants
      PROGRAM B_FIELD
      DOUBLE PRECISION pi, M, phi(0:1300,0:1300), current, PHI_INIT,
     +            r,h,alpha, HH(0:2500,0:2500), Hi(0:2500,0:2500),
     +            Hj(0:2500,0:2500), H_INIT, BIGPHI(0:2500,0:2500),
     +             dHi(0:2500,0:2500), dHj(0:2500,0:2500),
     +             dHH(0:2500,0:2500)
      INTEGER       flag(0:1300,0:1300),jstar,istar,Nx,Ny,NUMITER,
```

```
     +            i,j,bigNy,bigNx,count
      LOGICAL       DONE
      PARAMETER     (M = 9.788029D5, pi=3.14159265358979D0)
*     M is the magnetization, |M|, of the magnet in ampere/meter
*
*     Use optimum alpha for 2D Cartesian coordinates.
*     Although not optimum for this problem, it should be a reasonable guess.
      alpha=1.0          ! 0.1-1D-5 doesn't give much difference to results,
                         ! only increases iterations
      count = 0          ! Initialize counter

      PHI_INIT=1.0       ! phi initial value
      H_INIT=0           ! H initial value
      h=5D-5             ! grid step in meters (50 micron step size)

      jstar=0.0007493/h     ! top surface of the magnet (0.0295" from origin)
      istar=0.0025019/h     ! cylindrical side surface of the magnet (0.0985" from origin)

      Ny=0.05/h          ! the grid size is Nx*Ny (50 mm x 50 mm)
      Nx=0.05/h

      bigNy=2*Ny         ! to be used when unfolding the field in all four quadrants
      bigNx=2*Nx         ! same as for bigNy

      NUMITER=50000      ! maximum allowable number of iterations

*     FLAG is an integer array that characterizes a point in the grid. It is used to determine
```

```
*     which of various equations to use in determining the solution, according to the
*     following "code":
*     Initialize PHI and FLAG:
*
      DO i = 0, Nx
          DO j =0, Ny
              flag(i,j)=1
              phi(i,j) = PHI_INIT
          END DO
      END DO
*     in the plane of j=0
      DO i = 0,Nx
           flag(i,0) = 7
           phi(i,0) = 0
      END DO

*     Initialize all boundaries, points, etc.
*     fixed value point on the boundary of the computational grid
*     i.e., at infinity
      DO i = 1, Nx
           flag(i,Ny) = 2
      END DO
      DO j = 1, Ny
           flag(Nx,j) = 2
      END DO
*     along the axis of the magnet
      DO j = 1, Ny
```

```
            flag(0,j) = 3
        END DO
*-------------------------------------------------------------------------------------------------*
*     phi(0,j) = (4*phi(1,j)+phi(0,j+1)+phi(0,j-1))/6
*-------------------------------------------------------------------------------------------------*
*     on the cylindrical walls
        DO j = 1, jstar-1
            flag(istar,j) = 4
        END DO
*-------------------------------------------------------------------------------------------------*
*     phi(istar,j) = (phi(istar+1,j)+phi(istar-1,j))/2
*-------------------------------------------------------------------------------------------------*
*     on the top surface of the magnet
        DO i = 1, istar-1
            flag(i,jstar) = 5
        END DO
*-------------------------------------------------------------------------------------------------*
*     phi(i, jstar)=(M*h+phi(i,jstar+1)+phi(i,jstar-1))/2
*-------------------------------------------------------------------------------------------------*
*     at a corner of the magnet
        flag(istar,jstar) = 6
*-------------------------------------------------------------------------------------------------*
*     Average at jstar and istar:
*     phi(istar, jstar)=(M*h+phi(istar,jstar+1)+
*     phi(istar,jstar-1)
*     +phi(istar+1,jstar)+phi(istar-1,jstar))/4
*-------------------------------------------------------------------------------------------------*
```

```
*****************************************************************
*
*     S(uper)O(ver)R(elaxation) iteration loop starts here...

  100 DONE = .TRUE.
      count = count + 1
      IF (count .GE. NUMITER) THEN
      GOTO 999
      END IF

*     The following DO LOOPS do the actual SOR, using the
*     relaxation parameter alpha, and defining:
*     "phi(i,j)" as the old value of the magnetostatic potential, phi, and as
*     "current" the latest iterate.
*
      DO j = 0, Ny
            DO i = 0, Nx
            IF ( flag(i,j) .EQ. 1 )THEN
            current = ((1+h/(2*i*h))*phi(i+1,j)+(1-h/(2*i*h))
     +              *phi(i-1,j)+phi(i,j+1)+phi(i,j-1))/4
            ELSE IF(flag(i,j) .EQ. 2)THEN
            r=SQRT((i*h)**2+(j*h)**2)
            current= (M*j*h*pi*((istar*h)**2)*(2*jstar*h))/(4*pi*r**3)
*     The quantity [pi * ((istar*h)**2) * (2 * jstar*h)] is the volume
*     of the magnet, V
            ELSE IF(flag(i,j) .EQ. 3)THEN
                current = (4*phi(1,j)+phi(0,j+1)+phi(0,j-1))/6
```

```
            ELSE IF(flag(i,j) .EQ. 4)THEN
                current = (phi(istar+1,j)+phi(istar-1,j))/2
            ELSE IF(flag(i,j) .EQ. 5)THEN
                current = (M*h+phi(i,jstar+1)+phi(i,jstar-1))/2
            ELSE IF(flag(i,j) .EQ. 6)THEN
                current = (M*h+phi(i,jstar+1)
     +              +phi(i,jstar-1)+phi(istar+1,j)+phi(istar-1,j))/4
*           ELSE IF(flag(i,j) .EQ. 7)THEN
*               current = 0
            END IF
            IF(count.GT.1000) alpha=1D-5
            IF((abs((current-phi(i,j))/current).GT.1D-5))
     +          DONE = .FALSE.
                phi(i,j) = current +alpha * (current-phi(i,j))
            END DO
        END DO
        IF (.NOT.DONE) THEN
        GOTO 100
        ENDIF
**********UNFOLDING PHI OVER ALL QUADRANTS **********
*     initialize big arrays
  999 DO j=0,bigNy
        DO i=0,bigNx
          BIGPHI(i,j)=PHI_INIT
          Hi(i,j)=H_INIT
          Hj(i,j)=H_INIT
          HH(i,j)=H_INIT
```

```
            dHi(i,j)=H_INIT
            dHj(i,j)=H_INIT
            dHH(i,j)=H_INIT
          END DO
        END DO
*     using symmetry to calculate phi everywhere
        DO j=0,Ny
         DO i=0,Nx
            BIGPHI(Nx+i,Ny+j)=phi(i,j)
            BIGPHI(Nx-i,Ny+j)=phi(i,j)
            BIGPHI(Nx+i,Ny-j)=-phi(i,j)
            BIGPHI(Nx-i,Ny-j)=-phi(i,j)
         END DO
        END DO
************************ PRINTING OUT i, j, phi(i,j) ********************
        PRINT*
        PRINT*,"# i j phi(i,j)"
        PRINT*
        OPEN(11,file='Nd1.txt')
        DO j=0,bigNy
         DO i=0,bigNx
            WRITE(11,555) real(i-Nx)/508,real(j-Ny)/508,BIGPHI (i,j)
         END DO
        END DO
        close (11)
*********************CALCULATING Hi(i,j), Hj(i,j), |HH(i,j)|******************
*     calculating Hx component of the H vector
```

```
      DO j=0,bigNy
         DO i=1,bigNx-1
            Hi(i,j)=-(BIGPHI(i+1,j)-BIGPHI(i-1,j))/(2.0*h)
         END DO
      END DO
*     calculating Hy component of the H vector
      DO i=0,bigNx
         DO j=1,bigNy-1
            Hj(i,j)=-(BIGPHI(i,j+1)-BIGPHI(i,j-1))/(2.0*h)
         END DO
      END DO
*     calculating the absolute value (called HH) of the H vector
      DO i=0,bigNx
         DO j=0,bigNy
            HH(i,j)=SQRT(Hi(i,j)**2+Hj(i,j)**2)
         END DO
      END DO


********************** PRINTING PARAMETERS OUT ********************
      PRINT*
      PRINT*, "# No. of iterations= :", count
      PRINT*, "# h= :",h
      PRINT*, "# Nx= :",Nx
      PRINT*, "# Ny= :",Ny
      PRINT*, "# bigNx= :",bigNx
      PRINT*, "# bigNy= :",bigNy
      PRINT*, "# M= :",M
```

```
      PRINT*, "# alpha= :",alpha
      PRINT*, "# PHI_INIT= :",PHI_INIT
      PRINT*, "# H_INIT= :",H_INIT
      PRINT*, "variables= x,y,Hi,Hj,HH"
      PRINT*, "zone J=899,I=899,F=point,F=point,F=point"
******************PRINTING OUT i, j, Hi(i,j),Hj(i,j)AND |HH(i,j)|**************
      PRINT*
      PRINT*,"# i j Hi(i,j) Hj(i,j) HH(i,j)"
      PRINT*
      OPEN(12,file='Nd2.txt')
      DO j=1,bigNy-1
          DO i=1,bigNx-1
              WRITE(12,555) real(i-Nx)/508,real(j-Ny)/508,
     +           Hi(i,j),Hj(i,j),HH(i,j)
          END DO
      END DO
      close(12)
******************CALCULATING dHi(i,j), dHj(i,j), |dHH(i,j)|*****************
*     calculating dHi component of the dH vector
      DO j=0,bigNy
          DO i=1,bigNx-1
              dHi(i,j)=(HH(i+1,j)-HH(i-1,j))/(2.0*h)
          END DO
      END DO
*     calculating dHj component of the dH vector
      DO i=0,bigNx
          DO j=1,bigNy-1
```

```
            dHj(i,j)=(HH(i,j+1)-HH(i,j-1))/(2.0*h)
        END DO
    END DO
*   calculating the absolute value (called dHH) of the dH vector
    DO i=0,bigNx
        DO j=0,bigNy
            dHH(i,j)=SQRT(dHi(i,j)**2+dHj(i,j)**2)
        END DO
    END DO
******************PRINTING OUT i, j, dHi(i,j),dHj(i,j)AND |dHH(i,j)|***********
    PRINT*
    PRINT*,"# i j dHi(i,j) dHj(i,j) dHH(i,j)"
    PRINT*
    OPEN(13,file='Nd3.txt')
    DO j=2,bigNy-2
        DO i=2,bigNx-2
            WRITE(13,555) real(i-Nx)/508,real(j-Ny)/508,
   +         dHi(i,j),dHj(i,j),dHH(i,j)
        END DO
    END DO
    close(13)
555  FORMAT(1X,f8.4,1X,f8.4,F18.2,F18.2,F18.2)
    END
```

A.2 References

1. Leventis, N. and X. Gao, *Magnetohydrodynamic electrochemistry in the field of Nd-Fe-B magnets. Theory, experiment, and application in self-powered flow delivery systems.* Analytical Chemistry, 2001. **73**(16): p. 3981-3992.